Quantum light source compatible with solid-state quantum memories and telecom networks

Daniel Rieländer

The Institute of Photonics / Universidad Politècnica de Catalunya

A thesis submitted for the degree of

PhilosophiæDoctor (PhD)

September 28, 2016

Resumen

Esta Tesis doctoral se encuentra en el área de la comunicación cuántica experimental. Trata de pares de fotones de los cuales uno está almacenado en una memoria cuántica de estado sólido y su pareja es compatible con redes telecom. Las correlaciones cuánticas entre un fotón telecom y un fotón almacenado en una memoria cuántica son un recurso importante para aplicaciones del futuro como un repetidor cuántico, que permite la transmisión de un estado cuántico hacia distancias largas. Durante la primer parte de la tesis, se ha desarrollado una fuente de fotones nueva basada en la conversión paramétrica espontanea (SPDC). SPDC es un proceso no lineal que divide esporádicamente un fotón de alta frecuencia en dos fotones correlacionados de baja frecuencia dentro de un rango de varios centenares de GHz, llamados fotones signal y idler. La fuente es compatible con una memoria cuántica de estado sólido basada en un cristal dopado con iones de praseodimio, usando el protocolo de pinta de frecuencias atómica (AFC). Este material ha demostrado propiedades extraordinarias para el almacenamiento de luz coherente. Sin embargo, ofrece un ancho de banda muy limitado de 4 MHz alrededor de una longitud de onda de 606 nm para el almacenamiento. Esto pone requisitos muy rigurosos a los fotones creados. Para cumplir con estos requisitos el proceso de SPDC se encuentra dentro de una cavidad de configuración "bowtie". La cavidad es resonante con los fotones de signal y los de idler, que tienen longitudes de onda diferentes, que induce pares de fotones extensamente no-degenerados. Esta resonancia doble induce un fuerte efecto de agrupación de modos espectrales, que evita un gran número de modos redundantes. El espectro de los fotones creados se ha investigado detenidamente y contiene tres grupos con pocos modos espectrales. La anchura de cada modo es 2 MHz y cumple con los requisitos de la memoria cuántica. El filtraje de un modo único se realiza con una cavidad de Fabry-Perot adicional. El resultado es la demonstración de los pares de fotones más estrechos en un modo espectral individual creados por SPDC. En la segunda parte de la tesis se crean fotones individuales de 606 nm anunciados por la detección de un fotón de 1436 nm. Estos fotones anunciados se almacenan como excitación colectiva óptica en un cristal de praseodimio usando el protocolo de AFC. Correlaciones no-clásicas entre el fotón almacenado y el

fotón anunciante se observan hasta una duración de almacenado de 4 µs, 20 veces más largo que lo conseguido en experimentos previos con una memoria cuántica de estado sólido. Con el desarrollo posterior de la fuente se logró una tasa de coincidencia un orden de magnitud más alta y una eficiencia de anunciado del 28 %. La naturaleza del fotón individual anunciado se demostró por medido del "antibunching" del campo signal. Estos avances hicieron que los fotones creados fueran compatibles con el almacenamiento en el estado de spin del cristal de praseodimio usando el protocolo completo de AFC. Esto permitió que la duración de almacenamiento fuera extendida a 11 µs y también una lectura en demanda. La última parte de la tesis explora entrelazamiento en frecuencia entre los pares de fotones creados. Es un tipo de entrelazamiento, aún poco investigado, basado en los modos espectrales, que es muy conveniente para los fotones de banda estrecha. Tomamos la ventaja de que la fuente crea varios modos de frecuencias separados y correlacionados en energía. Para demonstrar una superposición coherente de los modos de frecuencia usamos moduladores electro-ópticos para mezclarlos coherentemente. Demostramos franjas de interferencia entre dos fotones con una alta visibilidad, un fuerte indicador del entrelazamiento en frecuencia.

Los resultados presentados en esta tesis abren la puerta a la demonstración de entrelazamiento entre una memoria de estado sólido y un fotón telecom. Esto representa un paso importante hacia la realización de un repetidor cuántico usando dispositivos de estado sólido.

Abstract

This PhD thesis is in the scope of experimental quantum communication. It deals with correlated photon pairs of which one photon is stored in a solid state device, while the other photon is at telecom wavelength. Quantum correlation between a photon at telecom wavelength and a photon stored in a quantum memory is an important resource for future applications like quantum repeaters, allowing the transmission of quantum states over long distances.

During the first part of this thesis, a novel photon pair source has been developed, based on spontaneous parametric downconversion (SPDC) inside a bow-tie cavity. SPDC is a non-linear process which splits a pump photon sporadically into two correlated photons, called signal and idler photon. The source used in this work has been designed to be compatible with a solid state quantum memory based on a praseodymium doped crystal, using the atomic frequency comb (AFC) protocol. This material has shown promising properties for classical light storage. However, it features a small storage bandwidth of 4 MHz at 606 nm, which sets stringent requirements for the photons to be stored. To match these requirements the SPDC process takes place inside a bow-tie cavity which is resonant with the created signal and idler photons. The difference between storage wavelength and telecom wavelength (1436 nm in our case) leads to widely non-degenerate photon pairs. Double resonance leads to a strong clustering effect, which suppresses a high number of redundant spectral modes. The created photon spectrum is investigated carefully and consists of three clusters with few well separated modes. The width of each mode is around 2 MHz and matches the requirement for the quantum memory. Single mode operation was achieved by placing an additional Fabry-Perot cavity in the idler field at 1436 nm. This resulted in the demonstration of the narrowest photon pairs consisting of a spectral single mode, created by SPDC to date.

In the second part of the thesis, heralded single photons at 606 nm were created by the detection of a photon at 1436 nm. These heralded photons were then stored as collective optical excitations in a praseodymium crystal, using the AFC scheme. Non-classical correlation between the heralding photon and the stored

and retrieved photons were observed for storage times up to 4 µs, 20 times longer than achieved in previous solid state quantum memory experiments.

Further development on the source led to improved results, including an increase of coincidence count rate by one order of magnitude and a heralding efficiency of 28 %. The single photon nature of the heralded photon was also measured directly by showing strong antibunching of the 606 nm signal field. These improvements made the created photons compatible with the storage in the spin state of the praseodymium level scheme, using the full AFC protocol. That enabled an extended storage time of 11 µs with on demand readout of the stored photon.

The last part of the thesis explores the possibility to use entanglement between the created photon pairs. Here we show an approach of entanglement analysis, based on frequency bins, which is well suited for narrow band photons. We take advantage of the fact that the source naturally creates several energy correlated well separated frequency modes. In order to show the coherent superposition of the frequency modes, we use electro-optical modulators to coherently mix them. We could show high-visibility two-photon interference fringes, a strong indicator for entanglement in the frequency domain.

The results presented in this thesis open the door for the demonstration of entanglement between a solid-state spin-wave quantum memory and a photon at telecom wavelength. This represents an important step for the realization of quantum repeaters using solid state resources.

This PhD thesis is dedicated to every scientist who contributes with honesty, modesty and accuracy to the development of our knowledge.

List of publications

published:

- J. Fekete, D. Rieländer, C. Matteo and H. de Riedmatten. Ultranarrow-Band Photon-Pair Source Compatible with Solid State Quantum Memories and Telecommunication Networks. *Phys. Rev. Lett.*, 110:220502, May 2013.
  see also associated View Point in Physics by P. Hemmer

- Daniel Rieländer, Kutlu Kutluer, Patrick M. Ledingham, Mustafa Gündo§an, Julia Fekete, Margherita Mazzera, and Hugues de Riedmatten. Quantum storage of heralded single photons in a praseodymium-doped crystal. *Phys. Rev. Lett.*, 112:040504, Jan 2014.

in preparation:

- D. Rieländer, A. Lenhard, M. Mazzera, and H. de Riedmatten. Source of high quality narrowband telecom heralded single photons compatible with quantum memories. *arXiv:1608.08943, submitted to New Journal of Physics.*

- A. Seri, A. Lenhard, D. Rieländer, M. Güundoğan, M. Mazzera, Margherita and H. de Riedmatten. Non-classical correlations between single telecom photons and a multimode on-demand solid-state quantum memory. *manuscript in preparation.*

Contents

1

Introduction

The field of quantum information uses the extraordinary features of quantum mechanics to establish more powerful processors, secure communication, simulation of complex atomic systems or ultra precise sensing. Quantum processors are capable to calculate specific problems much faster than classical processors. With quantum key distribution a non interceptable communication based on physical laws is possible. Complex simulations of atomic systems allow to design materials with new properties on the smallest scale. Quantum sensing allows to enhance the precision of atomic clocks, magnetometers, length scales, etc. The work presented in this thesis goes into the direction of long distance quantum communication, which uses quantum repeaters to transfer a quantum state over long distances. Most quantum repeater architectures require photon pair sources, quantum memories and entanglement, experiments done during this PhD thesis cover these topics.

1.1 Quantum information science

1.1.1 Qubits

In contrast to classical information, where a bit can be in one of the states 0 or 1, quantum information uses a superposition of 0 and 1 the so called qubits

$$|\psi\rangle = \alpha|0\rangle + \beta|1\rangle \tag{1.1}$$

, with $\alpha^2 + \beta^2 = 1$, the probability coefficients α and β. The states $|0\rangle$ and $|1\rangle$ can be for example different polarization states (expressed as $|H\rangle$ and $|V\rangle$) or the ground $|g\rangle$ and the excited $|e\rangle$ state in a two level atomic system. In general, qubits can be divided in two classes: Flying qubits, which can be used to distribute quantum information, encoded in single photons or weak coherent states and stationary qubits, which can be used to store quantum information in quantum memories, based on atoms, ions or impurities in solids.

A classical bit keeps the same value after measuring it, and thus can be copied and amplified. That enables an unlimited transfer distance for classical information. In contrast, a measurement on a qubit projects its state on the measurement basis and therefore defines the probabilities it in that basis. Since there is no way to know the exact outcome of a qubit before measuring it, qubits cannot be copied nor amplified [1]. That limits the approachable distance and their lifetime due to optical losses and decoherence.

1.1.2 Entanglement

An important resource for quantum information science is given by entanglement.

Entanglement is a fundamental quantum effect, in which two or more particles, e.g. photons, share the same non-separable quantum state. It is a required resource for advanced quantum communication processes, like quantum computing or quantum repeaters. Photons can be entangled e.g. in polarization, time-bins, momentum, path and in frequency.

An entangled state can be expressed as:

$$|\phi\rangle = \frac{1}{\sqrt{2}}(|10\rangle + e^{i\phi}|01\rangle) \tag{1.2}$$

This state describes a non-separable state of two particles and leads to correlation stronger than possible with classical particles. The outcome of each particle is not known until a measurement on one of the two particles is performed. The measurement projects the state of both particles on a certain measurement basis and defines their own states in the used basis instantaneously. After a measurement is taken each particle owns a separated state and the entanglement is dissolved.

However, it is possible to perform operations on entangled states, like spin flips, transformations, teleportation [2], swapping [3] without measuring their state. This creates the possibility of performing quantum algorithms.

1.1.3 Quantum computation

Today's encryption techniques, used in private E-Mail communication, bank transfers or secret service issues, are based on the factorization of very large numbers into their prime factors. Using classical computers, with actual known algorithms, the decryption of these data would take much longer than the lifetime of several generations. A quantum computer with a sufficient number of operating qubits could do the factorization much faster and obtain a lot of sensitive information by decryption. The best known quantum algorithm is the Shor's algorithm [4], it allows to factorize integers with a polynomial increase of calculation steps which is significantly faster for large numbers than the exponential increase with classical algorithms used today. Shor's algorithm has been already applied for small numbers like 15 [5] and 21 [6]. Since the field of quantum information is progressing very fast, new encryption technologies will be required soon.

1.1.4 Quantum key distribution

On the other hand, quantum mechanics offers the possibility to exchange keys in a secure way using quantum key distribution (QKD). The security of QKD is based on the fact that a quantum state can not be copied due to the non-cloning theorem [1] and the result of a quantum state analysis could reveal an eavesdropper's measurement in the communication channel. One of the first algorithms for QKD is the BB84-protocol [7] which founded a basis for many more complex and improved protocols today [8].

For all protocols the distribution of qubits is required. While the non-cloning theorem is the heart of the security of QKD, it is also what prevents to send quantum information over large distances in optical fibers using direct transmission. The amplification of a single photon state is not possible and the absorption loss

in optical fibers increases exponentially with the distance. The number of qubits received by a distant party separated by the length L therefore scales as:

$$N = R \cdot P_0 \cdot \eta_t \eta_{det} = R \cdot P_0 \cdot e^{-\alpha \cdot L} \cdot \eta_{det} \tag{1.3}$$

where R is the repetition rate of the source, P_0 is the probability to emit a photon, η_t is the transmission of the quantum channel and η_{det} is the detection efficiency. The distribution of a quantum state in between Barcelona and Madrid, which are separated by a distance of roughly 600 km, using one single photon source with a generation rate of $R = 10\,\mathrm{GHz}$ and unit efficiency ($P_0 = 1$), transmitted in a low loss telecom fiber ($0.2\,\mathrm{dB\,km^{-1}}$), would take in average 1.5 min (for $\eta_{det} = 1$). For a distance of 1000 km, e.g. between Paris and Berlin, the average duration to detect a photon would be more than 300 years. The longest distance of secure QKD with qubits encoded in weak coherent states has been 307 km so far [9]. Using entangled photon pairs and placing the source in between two receivers the detection rate is given by:

$$C = R \cdot P_0 \cdot \sqrt{\eta_t}\sqrt{\eta_t} \cdot \eta_{det}^2 \tag{1.4}$$

We see that the distribution of entangled states alone does not change the scaling with distance. A solution to alleviate the distance limitations is given by quantum repeater protocols [10–12], combining entanglement distribution, entanglement swapping and quantum memories. Using these architectures the losses scale only polynomially with distance.

1.2 Quantum repeaters

Quantum repeater protocols [10–12] suggest to divide the distance in shorter segments with the possibility to store the entanglement in quantum memories (QM) at the connection points in between the segments. After entanglement is distributed successfully between the two quantum memories of one segment, it is stored until the entanglement of the neighboring segment is heralded. Then the entanglement can be swapped at the connection nodes and extended to the outer memories. The fact that the entanglement can be stored in quantum memories

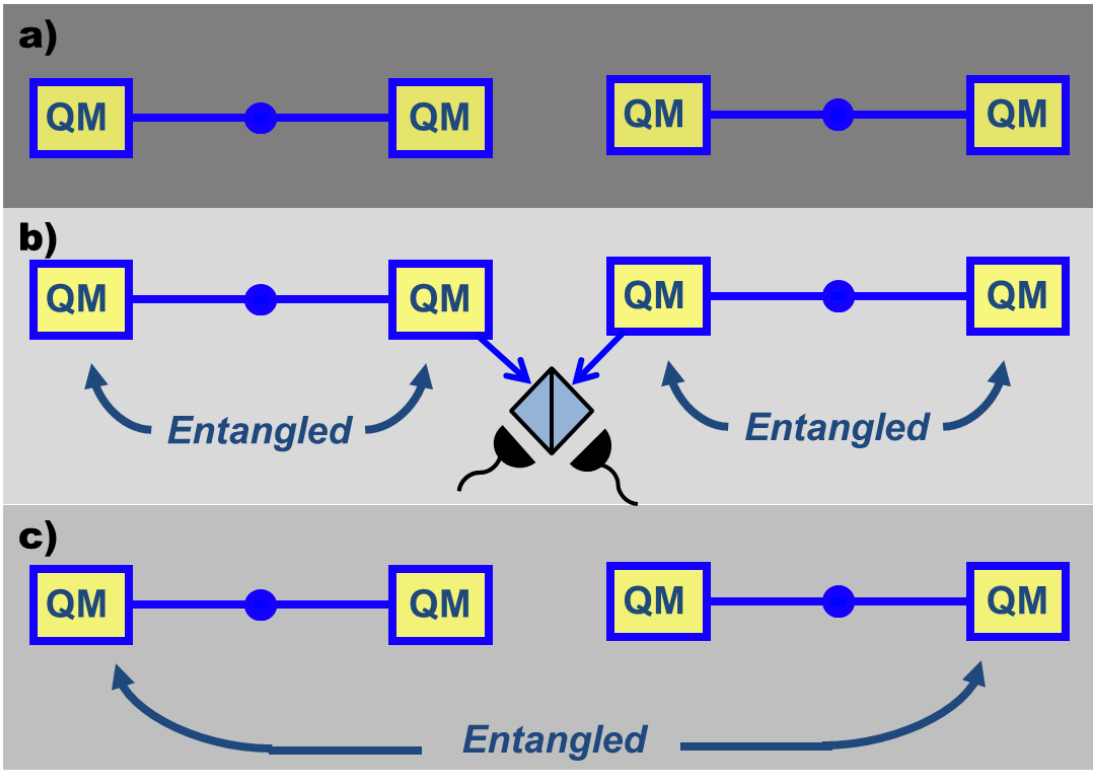

Figure 1.1: a) long distances could be divided in smaller segments, consisting of quantum relays with entangled photon pair sources and quantum memories at the edges. b) Entanglement could be distributed in between the shorter distances of each segments and stored in the quantum memories. Once entanglement in two neighboring segments is created a Bell measurement can be performed in between the two inner quantum memories. c) If successful, the entanglement is extended towards the outer quantum memories as a result of the swapping operation. Further segments could be added and the entanglement can be extended to longer distances.

allows the different segments to be independent from each other. This implies that the entanglement distribution within each segment does not need to succeed simultaneously in each segment. For that reason the loss doesn't scale exponentially with distance any more, instead a polynomial scaling leads to higher success probabilities for long distances. If several modes can be stored at the same time in a quantum memory, the success probability increases linearly with the number of modes [12–14]. An illustration for better understanding is given in Fig. 1.1. For the development of functional quantum repeaters, it is necessary to develop quantum memories and compatible quantum light sources with extraordinary performances. In addition the photons used for the transmission should be at telecom wavelentgh, where the absorption loss is low.

To increase the quality of entangled states, which may be degraded by transmission losses in optical fiber, imperfect entanglement swappings and noise from quantum memories, entanglement purification protocols [15] can be applied.

A new generation of quantum repeaters based on quantum error correction has been proposed recently, that do not require quantum memories [16–18]. However, this type of repeaters require much more advanced resources and capabilities than the one based on heralded entanglement and quantum memories.

1.2.1 Our approach to build a quantum repeater

Suggested protocol

We follow an approach based on photon pair sources and solid state quantum memories which can store multiple temporal modes at the same time [13]. A schematic drawing is depicted in Fig. 1.2.

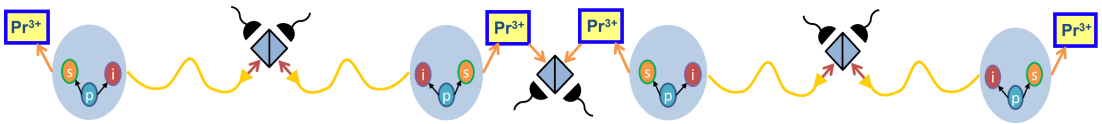

Figure 1.2: Scheme of quantum repeater protocol.

Each node includes a photon pair source and a quantum memory. The photon pair sources emit one photon resonant with the quantum memory and one photon

at telecom wavelengths, which benefits from very low losses in fibers and the use of existing telecom infrastructures. The photon pair sources are pumped coherently, leading to the state:

$$\left[1+\sqrt{\frac{p}{2}}\left(e^{i\phi_A}a^\dagger a'^\dagger+e^{i\phi_B}b^\dagger b'^\dagger\right)+O(p)\right]|0\rangle \tag{1.5}$$

One mode of each source is stored in the quantum memory next to the photon pair source, while the other photon is sent over long distance in an optical fiber. At a central location between the two photon pair sources, the photons coming from the two distant sources are combined at a beam splitter, which erases the information about their origin. This leads to a probabilistic implementation of entanglement swapping. A photon detection behind the beam splitter will project the two remote quantum memories onto an entangled state:

$$|\Phi_{AB}\rangle=\frac{1}{\sqrt{2}}(|1\rangle_A|0\rangle_B\pm e^{i\theta_{AB}}|0\rangle_A|1\rangle_B) \tag{1.6}$$

The state describes two entangled quantum memories at Alice (A) and Bob's (B) position of which one contains a collective atomic excitation, while the other one is in the ground state. In that case, the entanglement between the two remote QMs is probabilistic, but heralded, which is crucial for the scalability of the quantum repeater. If entanglement is established in two neighboring segments containing the quantum memories A,B and C,D, photons of the inner quantum memories (B,C) can be read out and the entanglement can be swapped by a photon detection after the beam splitter (see Fig. 1.1 (b)) onto the outer quantum memories A and D. The entangled state

$$\frac{1}{\sqrt{2}}(a^\dagger+e^{i(\theta_{AB}+\theta_{CD})}d^\dagger)|0\rangle \tag{1.7}$$

between quantum memory A and D is created. We see that the phases θ_{AB} and θ_{CD} play a crucial role and phase stability between the involved photon pair sources is required. In this way, it is possible to establish entanglement between more distant memories. If entanglement is distributed in two parallel chains (1,2) to the locations A and Z, then the projection into the subspace where at least

one excitation is present in A and Z is analogous to conventional polarization or time-bin entanglement [13]:

$$|\Psi_{AZ}\rangle = \frac{1}{\sqrt{2}}(a_1^\dagger z_2^\dagger + e^{i(\theta_2-\theta_1)} a_2^\dagger z_1^\dagger)|0\rangle \tag{1.8}$$

This protocol is advantageous because it requires only single particle detection for the entanglement connections. In addition, used in combination with QMs that can store multiple qubits in the time domain, it has the advantage of allowing time multiplexing. That can increase the distribution probability by a factor of N_m, where N_m is the number of modes that can be stored in the memory.

The key ingredient to realize an elementary segment of this quantum repeater architecture are thus quantum memories, and photon pair sources with one photon compatible with the memory and the other photon at telecom wavelength.

Our recourses for the implementation

Our QM consists of a praseodymium doped crystal (Pr^{3+}:Y_2SiO_5). Photons with a wavelength of 606 nm and a narrow spectral bandwidth of few MHz can be stored in this crystal. The spectral bandwidth is limited by the electronic structure, because of the small separation between the excited states (see Fig 1.3). Therefore the photon pair source has to provide narrow band photons at 606 nm at one output-arm, guided to the QM close by, correlated with photons at telecom wavelength for far transmission in an optical fiber.

To create these pairs we chose the process of spontaneous parametric down-conversion (SPDC) in a nonlinear crystal. One pump photon is split sporadically into two correlated (in time and energy) photons, called signal and idler photons. Energy and momentum conservation have to be satisfied and lead to the phase-matching condition. SPDC can be used to implement heralded single photon sources: one photon is detected and heralds the arrival time of a single photon in the other mode. The drawback of SPDC is that the generated photon pairs have a bandwidth which is determined by the phase matching condition, resulting in a typical width in the order of hundreds of GHz.

By placing a cavity around the nonlinear crystal it is possible to reduce the bandwidth of the out-coupled photons to the width of the cavity modes, which

can be in the MHz range, while keeping a high count rate due to cavity enhancement. This configuration corresponds to an optical parametric oscillator (OPO) far below threshold.

SPDC has the advantage of wavelength flexibility, depending on the crystal design, the phase matching conditions and the pump wavelentgh. Many wavelength combinations are possible including a wide spreading of signal and idler wavelengths. The quantum memory restricts us to 606 nm for the signal wavelength, while we are more free in the choice of the idler wavelength, which requires low absorption in optical fibers. Optical fibers used for telecommunications possess a small absorption for several wavelength windows between 1200 nm and 1700 nm. For practical reasons (availability of the pump laser) the wavelength of our telecom photon is at 1436 nm where the absorption in optical fibers can be as low as $0.2\,\mathrm{dB\,km^{-1}}$.

1.2.2 Required performances for a quantum repeater

To distribute entanglement over 600 km and beat direct transmission in the success probability components with excellent performances as shown in Tab. 1.1 have to be connected [12].

Protocol	[13]	
Detectors with	$> 90\,\%$	detection efficiency
Memories with	$> 90\,\%$	storage efficiency
Memories with	$\sim 2\,\mathrm{s}$	storage time
Multi mode capacity with	100	modes
Elementary links	4	segments
Single photons at	telecom wavelength	interfaced with a quantum memory

Table 1.1: requirements for a quantum repeater

Single photon detectors with more than 90 percent detection efficiency are already available, even at telecom wavelength. However they have to be cooled to cryogenic temperatures [19, 20]. Even though important progress has been realized in last years in the performances of quantum memories and photon pair

sources (see section 1.3), the combination of all required properties remains so far elusive.

Entanglement purification which enhances the fidelity, would require several entanglement chains in parallel and thus decrease the count rate. The parameters in table 1.1 have been calculated in [12] assuming that the number of links would be low enough to be able to achieve a sufficient fidelity without entanglement purification.

1.3 State of the Art

1.3.1 Solid state quantum memories

As quantum memory we use a rare earth (RE) doped crystal. These materials, when cooled down to below 4 K, have interesting properties for storage applications. They provide a system with a large number of atoms naturally trapped in a transparent solid state matrix. This prevents the atoms from moving and constitute a so called 'frozen' gas of atoms. RE doped crystals are characterized by long coherence times. They can be used for multiplexed storage using different temporal [21–23], spectral [24] or spatial [25] modes. Spectral hole burning techniques can be applied to slow down the light [26–28] and in combination with atomic frequency comb protocols long storage times for quantum light are possible [13, 29, 30].

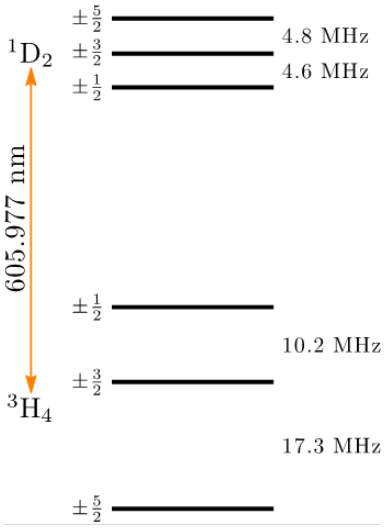

Figure 1.3: Level structure of praseodymium ions.

The first demonstration of storage in RE doped solids at single photon level has been realized a Nd-doped crystal (Nd:YVO_4) using the atomic frequency comb (AFC) protocol [31]. Storage of entangled photons, created by SPDC in a nonlinear waveguide, in Nd^{3+}:Y_2SiO_5 has been realized [32, 33]. A heralded entanglement of two Nd-doped crystals has been shown with a photon pair source based on SPDC [34]. However, this scheme cannot be applied to remote quantum memories. The storage in Nd^{3+}:Y_2SiO_5 is restricted to the excited state, since an appropriate level structure with a third long lived ground state is not available. That limits the storage to short and predetermined times.

Instead, praseodymium doped crystals (Pr^{3+}:Y_2SiO_5), do offer an appropriate level structure with a threefold ground state (shown in Fig. 1.3) which makes Pr^{3+}:Y_2SiO_5 an interesting candidate for spin wave storage. That offers the possibility to extend the storage time and brings the possibility of an on de-

mand readout. In addition, these crystals provide high absorption of around $\alpha = 20\,\mathrm{cm}^{-1}$ at the optical transition combined with spin levels with excellent coherence properties. This allows high internal efficiencies up to 76 % (measured in multi-pass configuration for very short storage time) [35] and long storage times up to 90 s (albeit with low efficiency in the percent range) [36] for classical light, using stopped light based on electro-magnetically induced transparency (EIT). These high efficiencies and long storage times have been shown with strong laser pulses with a duration in the µs-range. The long duration of the laser pulses is necessary to match the limited bandwidth of EIT. For the development of quantum repeaters the realization with few photons, which allow entanglement, is required. Weak coherent states which are close to the single photon level have shown efficiencies up to 69 % in the excited state [37]. The highest spin-wave storage efficiency at the single photon level is currently 23 % [38]. These properties make Pr^{3+}:Y_2SiO_5 an excellent candidate for applications as solid state quantum memories.

Despite very promising properties, quantum light had never been stored in a Pr^{3+}:Y_2SiO_5 crystal before the beginning of this thesis. A drawback of the level structure of praseodymium is that the splitting in the excited state is around 4 MHz, which leads to a small storage bandwidth. This makes the storage of quantum light challenging, since typical sources have a broad bandwidth of hundreds of gigahertz. The challenging task to realize storage of quantum light, respectively heralded single photons, in this material is the main goal of this thesis.

1.3.2 Narrowband photon pair sources based on spontaneous parametric downconversion

The most common way to generate entangled photon pairs is to use spontaneous parametric downconversion (SPDC). It is a nonlinear process in an anisotropic crystal which creates sporadically a photon pair out of one pump photon. A detailed description of the process can be found in section 2.1. SPDC allows quite simple setups and flexibility in the choice of wavelength. The drawback of SPDC is that the photons created have a large spectral bandwidth which is

usually hundreds of GHz. This value is significantly higher than the bandwidth of most atomic transitions including rare earth based quantum memories.

One possibility to match the bandwidth with atomic transitions would be to apply narrowband spectral filtering behind an efficient source based on waveguides [32, 34, 39–44]. In that case filtering reduces the count rate per second. However it was possible to scale the bandwidth down to 9 MHz to store single photons in a cold atomic Rubidium cloud using electromagnetically induced transparency [39]. Some sources were used to store entanglement [32–34, 42, 43] in crystals. A possible technique to generate entangled photon pairs is to use two separated SPDC-crystals [42, 43].

Another approach to generate narrowband photon pairs is to place a nonlinear crystal used for SPDC inside a cavity, resonant to the photon pairs. It has been shown that in this configuration the bandwidth of SPDC photon pairs can be reduced, while the spectral brightness of the source inside the cavity modes is enhanced [45]. More theoretical studies have been done [46, 47].

Very efficient and robust devices are based on integrated devices like waveguides with partially reflective endface coating [48–51] or on whispering gallery mode resonators [52, 53]. An integrated source based on a microring cavity generates frequency multiplexed photon pairs at telecom wavelength [54]. However these sources haven't been used for storage experiments so far.

A more flexible design can be achieved placing a bulk crystal inside a bow-tie cavity [55–58]. This design is suited for long cavities with a tight focusing parameter. An elaborate locking scheme is required to match the photon linewidth with an atomic transition. Simpler Fabry-Perot designs are realized either with a monolithic cavity with coated end-faces [59] or semi-monolithic cavity with one coated end-face and one external mirror [60] or with two external mirrors [61–67]. Some of them use two crystals inside the cavity either to create polarization entangled pairs [55] or for compensation of the introduced birefringence by a type II crystal [57, 61–64].

With this kind of techniques, photon sources with line widths in the MHz range could be demonstrated with various designs [50, 53, 57, 58, 60, 63, 65, 67]. Interfacing such photons effectively with atomic transitions has also been demonstrated [39, 42, 44, 60, 65, 69–73]. These sources are of special interest for the

Reference	Bandwidth [MHz]	Wavelength [nm]	Atomic transition	Entanglement
passive filtering			resonant	
Akiba et al. [39]	9	795	^{87}Rb	
Clausen et al. [32]	35	883 + 1338	Nd:Y_2SiO_2	time-bin
Clausen et al. [42]	240	883 + 1338	Nd:Y_2SiO_2	polarization
Jin et al. [43]	6000	795 + 1553	Tm:$LiNbO_3$	time-bin
Saglamyurek et al. [44]	$6 \cdot 10^3$	795 + 1532	Er-doped fiber	time-bin
cavity enhanced			resonant	
Bao et al. [60]	9.6	780		polarization
Zhang et al. [65]	5	795	^{87}Rb	polarization
Wolfgramm et al. [57]	7	795	^{87}Rb	
Fekete et al. [58]	2	606 + 1436	$Pr^{3+}Y_2SiO_2$	
Zhou et al. [68]	9.6	780	Rb	
cavity enhanced			non-resonant	
Wang et al. [55]	18	860		polarization
Scholz et al. [63]	2.7	893		
Förtsch et al. [53]	26.8	tunable		
Luo et al. [50]	60	890 + 1320		

Table 1.2: narrowband photon pair sources

development of quantum repeaters. As mentioned before, one interesting scenario is that one photon of the source is stored in a quantum memory while its partner photon is used to distribute entanglement to the neighboring node [13]. To bridge large distances the second photon should be at a low loss telecommunication wavelength. To that end frequency non-degenerate sources have been developed [32, 42–44, 50, 58].

In table 1.2 an overview of the most important sources with their characteristics is given.

1.4 Brief summary of my contributions

I joined the group in October 2011 and started directly to work on the photon pair source with Julia Fekete, a postdoc who started in the same year. J. Fekete had already set up the PPLN crystal and started to characterize it in single pass configuration. She also designed the cavity which was included at a later stage in the setup. I already was experienced with optical parametric oscillators for efficient second harmonic generation I worked on during my Master thesis and single photon counting technologies due to my Bachelor thesis. Therefore I could directly contribute in the lab. The measurements presented in chapter 3 and in [58] were done in a team of both of us or by myself while J. Fekete was evaluating the results. In June 2013 I took over the responsibility of the source and its connection to the memory and prepared it for the measurements presented in chapter 4 and in [73]. This measurements were done in collaboration with the quantum memory team[1] in our group. Afterwards I investigated carefully how the source could be improved and applied changes on it presented in chapter 5 to prepare it for a possible storage in the spin state of our quantum memory. Apart from that I started to work on showing entanglement with the source. First I tried to implement polarization entanglement with a two crystal configuration similar to [55]. I took advantage of that possibility to investigate the reduction of the number of created modes due to the clustering effect. Both approaches didn't bring the desired results, because of technical limitations. Instead I suggested

[1] Kutlu Kutluer, Patrick Ledingham, Mustafa Gündogan, Margherita Mazzera

to show frequency entanglement based on the frequency modes created by our source. I started to work on that in the beginning of 2015 based on experiments shown in [74]. In June 2015 a new postdoc, Andreas Lenhard, joined our group and helped me a lot in taking and presenting the data about the frequency entanglement shown in chapter 6 and in retaking and presenting some data presented in chapter 5. At a later stage the evaluation of the frequency entanglement led to a collaboration with a theoretical group[1] in our institute led by Antonio Acin.

[1] Osvaldo Jimenez, Daniel Cavalcanti, Alejandro Máttar and Antonio Acín

2

Theoretical background

2.1 Spontaneous parametric down-conversion

In spontaneous parametric down-conversion (SPDC) a pump photon inside an optically nonlinear medium can split spontaneously into a pair of photons (called signal and idler), each of them at lower energy than the pump. The detection of one photon signals the presence of its partner photon. Hence, SPDC can be used as a source of heralded single photons [75].

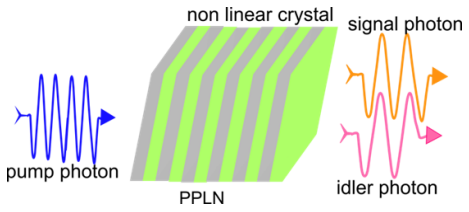

Figure 2.1: One pump photon enters a periodically poled crystal and creates a signal-idler photon pair spontaneously.

As in other non-linear processes, like second harmonic generation (SHG) or difference frequency generation (DFG), energy and momentum have to be conserved. Energy is conserved if:

$$E_{pump} = h\frac{c}{\lambda_p} = h\frac{c}{\lambda_s} + h\frac{c}{\lambda_i} \tag{2.1}$$

and the momentum $\hbar k = \hbar\frac{2\pi n_i}{\lambda_i}$ is conserved if no phase mismatch Δk is present

and the phase matching condition is fulfilled:

$$\Delta k = \frac{2\pi n_p}{\lambda_p} - \frac{2\pi n_s(\lambda)}{\lambda_s} - \frac{2\pi n_i(\lambda)}{\lambda_i} = 0 \tag{2.2}$$

The two photon state created by SPDC is derived e.g. in [76] and can be written as:

$$|\Psi\rangle_{PDC} = |0_s, 0_i\rangle + \eta \int d\omega_1 d\omega_2 f(\omega_1, \omega_2) |\omega_{1s}\omega_{2i}\rangle \tag{2.3}$$

where $f(\omega_1, \omega_2) = \alpha_p(\omega_1 + \omega_2)h(\omega_1, \omega_2)$ includes the spectral amplitude of the narrowband pump field $\alpha_p(\omega_1 + \omega_2)$ and the phase matching function

$$h(L\Delta k) = e^{-iL\Delta k/2} \cdot \mathrm{sinc}(L\Delta k/2) \tag{2.4}$$

.

2.1.1 Fulfilling phase matching condition

To fulfill the phase-matching condition given in Eqn. 2.2 birefringent materials are usually required, since dispersion is monotonous in the visible range. The anisotropy in birefringent crystals leads to an ordinary and an extraordinary refractive index which apply for orthogonal polarizations. That advantage can be used to create signal and idler photons with the same polarization, while the pump photons polarization is orthogonal (Type I) or to create photon pairs with orthogonal polarizations (Type II). To achieve the suitable relation between the refractive indices several techniques can be applied. The technique which was used first is called critical phase matching and can be applied by rotating the crystal to change the angle of its optical axis with respect to the incident beam. A more convenient technique is the non-critical phase matching which matches the refractive indices by temperature tuning.

A common technique, known as quasi phase matching, provides more flexibility in the choice of wavelengths but requires a special design. This technique in combination with non-critical phase matching for fine tuning is very powerful and used throughout the thesis.

Quasi phase matching

Critical and non-critical phase matching are bounded to certain wavelengths ranges due to given material properties. To overcome these bounds the crystal can be designed with an alternating orientation of its nonlinearity. This so called periodic poling changes the sign of the phase periodically and thus compensates the phase mismatch. Crystals can be produced with a poling period Λ in the µm-range. That adds an additional term the phase matching condition:

$$\Delta k = \frac{2\pi n_p}{\lambda_p} - \frac{2\pi n_s(\lambda)}{\lambda_s} - \frac{2\pi n_i(\lambda)}{\lambda_i} - \frac{2\pi}{\Lambda} = 0 \tag{2.5}$$

This term can fulfill the phase matching condition, with wavelength/refractive index combinations which would normally not provide phase matching. It allows also a new type of phase matching (type 0) with equally polarized pairs and pump photons. Fig. 2.2 illustrates how the conversion efficiency scales with a perfect

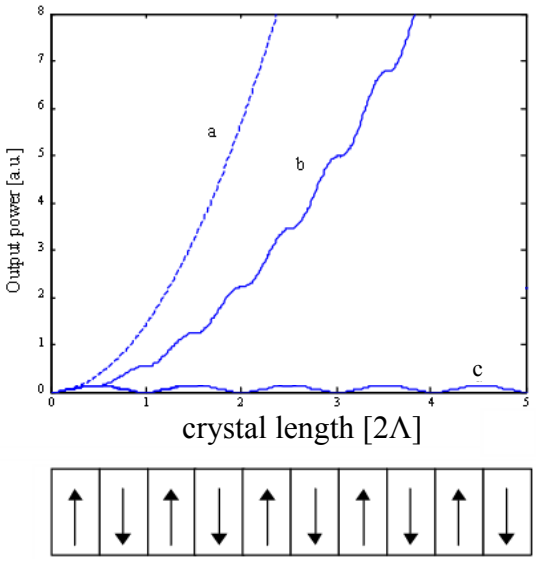

Figure 2.2: Comparison of output power versus crystal length between (a) perfectly phase matched, (b) first-order QPM, (c) non-phase matched frequency conversion. [77]

phase matching, a quasi phase matching and without phase matching.

2.1.2 Spectral bandwidth

The spectral shape of the signal, respectively idler, photon is given by the spectral power density function derived in [47]:

$$S(\nu_s) \propto L_c^2 \cdot \mathrm{sinc}^2\left(\frac{\Delta k(\nu_s, \nu_i = \nu_p - \nu_s) \cdot L_c}{2}\right) \tag{2.6}$$

with the crystal length L_c. The refractive indeces used to calculate Δk are wavelength dependent and can be calculated using the Sellmeier formulas [78]. For non-degenerate photons the bandwidth can be linearized, taking the group index $n^g_{s,i} = \frac{n_{s,i}}{1+\frac{\lambda}{n_{s,i}}\frac{\partial n_{s,i}}{\partial \lambda}}$ (approximated by a first order Taylor expansion) for signal and idler photons into account [59]:

$$\Delta\Gamma = 0.885 \cdot \frac{c}{L_c} \frac{1}{\mid n^g_i - n^g_s \mid} \tag{2.7}$$

2.1.3 Optimal beam waist

To maximize the conversion efficiency in non-linear processes of the second order, like SPDC, the beam waist has to be adjusted according to the crystal length L to obtain the highest possible intensity inside the crystal. A very short crystal requires a tight beam waist inside the center, while the intensity at the edges of a longer crystal would suffer from a too tight beam waist in the center.

The optimal ratio between the length of a crystal and the confocal parameter b is given by the Boyd-Kleinmann parameter [79]. For collinear phase matching without walk off it is:

$$2.84 = \frac{L_c}{b} \tag{2.8}$$

The confocal parameter b is two times the Rayleigh length z_r:

$$b = 2 \cdot z_r = 2 \cdot \frac{\pi \cdot n_{ref} \cdot \omega_0^2}{\lambda_p} \tag{2.9}$$

2.1.4 Statistics of SPCD

The state of the created photon pairs given in Eqn. 2.3 can also include higher order terms and be written as [80, chapter 9.5]:

$$|\Psi\rangle_{s,i} = \sqrt{1-p} \sum_{n=0}^{\infty} p^{\frac{n}{2}} |n\rangle_s |n\rangle_i \tag{2.10}$$

Here we don't consider the spectral shape of the created photon pairs as expressed in Eqn. 2.3. We just consider the number of created photons expressed in a n photon number Fock state $|n\rangle_{s,i}$ with a probability p for the decay of a pump photon into a photon pair. This state is known as two mode squeezed state. To avoid the generation of multiple photon pairs the generation probability has to be low $p \ll 1$. That distinguishes the spontaneous process from the stimulated process.

Cross-correlation

The temporal correlation between signal and idler photons can be measured by the second order intensity cross correlation function $G^{(2)}_{s,i}(\tau)$, the normalized form is denoted as:

$$g^{(2)}_{s,i}(\tau) \equiv \frac{\langle E^{\dagger}_s(t) E^{\dagger}_i(t+\tau) E_i(t+\tau) E_s(t)\rangle}{\langle E^{\dagger}_i(t+\tau) E_i(t+\tau)\rangle \langle E^{\dagger}_s(t) E_s(t)\rangle}, \tag{2.11}$$

where $E^{\dagger}_{s,i}$ and $E_{s,i}$ are the electric field creation and annihilation operators for the signal and idler fields. For an ideal two mode squeezed state, as in Eq. 2.10, the cross-correlation function is given by the generation probability:

$$g^{(2)}_{s,i} = 1 + \frac{1}{p} \tag{2.12}$$

A low p enables high correlation, but at the cost of generation rate. The mean number of photons generated is given by:

$$\bar{n}_s = \frac{p}{1-p} \tag{2.13}$$

In practice $g^{(2)}_{s,i}$ can also be determined over a detection window $\Delta\tau$ as:

$$g^{(2)}_{s,i}(\Delta\tau) = \frac{p_{s,i}}{p_s p_i} \tag{2.14}$$

where $p_{s,i}$ is the probability to detect a coincidence between signal and idler photons and p_s respectively p_i, the probability to detect a signal, respectively idler, photon in a time interval $\Delta\tau$.

Unconditioned auto-correlation

To characterize the state emitted by SPDC, another useful correlation function is the unconditional second order autocorrelation function $g^{(2)}_{s,s}$ and $g^{(2)}_{i,i}$. It can be obtained by setting a beam splitter in the signal or idler arm and detect the coincidences in the two obtained outputs. In the ideal case of a two mode squeezed state expressed in Eq. 2.10 the unconditional field exhibits thermal statistics with $g^{(2)}_{s,s}(0) = g^{(2)}_{i,i}(0) = 2$.

However noise, which doesn't show thermal correlations on the photon time scale, like detector dark counts or coherent background can lower this value. If the background in the detectors A and B are expressed as Dc_A and Dc_B, and the detected signal including background as N_A and N_B then the $g^{(2)}_{x,x}$-value is given by [73]:

$$g^{(2)}_{x,x}(0) = 1 + \frac{(N_A - Dc_A)(N_B - Dc_B)}{N_A \cdot N_B} \leq 2. \tag{2.15}$$

Another reason for a lower $g^{(2)}_{x,x}$-value can be the contribution of several spectral or temporal modes. Then the autocorrelation decreases as [81]

$$g^{(2)}_{x,x}(0) = 1 + 1/N \leq 2 \tag{2.16}$$

where N is the number of modes.

Conditioned auto-correlation

If the autocorrelation measurement is conditioned on a click on the detector at the correlated mode, the resulting value is connected to the cross-correlation and unconditioned auto-correlation values in the following way [82]:

$$g^{(2)}_{i:s,s} = \frac{g^{(2)}_{s,s} \cdot g^{(2)}_{i,i}}{g^{(2)}_{s,i}} \tag{2.17}$$

All classical states must obey $g^{(2)}_{i:s,s} \geq 1$ If p is low enough, the heralded signal field can be in a non-classical state. In that case each click heralds only one photon and no coincidences at zero time delay on the two detectors behind the beam splitter are expected. For $p \ll 1$, $g^{(2)}_{i:s,s}$ tends toward 0, and a single photon Fock state is generated.

Cauchy-Schwarz inequality

The non-classical nature of the correlation between signal and idler fields can also be experimentally assessed with a Cauchy-Schwarz inequality involving correlation functions. For a pair of independent classical fields the following inequality must be fulfilled:

$$R = \frac{(g^{(2)}_{s,i})^2}{g^{(2)}_{s,s} g^{(2)}_{i,i}} \leq 1 \tag{2.18}$$

If the signal and idler fields exhibit thermal or sub-thermal statistics $g^{(2)}_{s,s}(0) = g^{(2)}_{i,i}(0) \leq 2$, the measurement of $g^{(2)}_{s,i} > 2$ is therefore a signature of non-classical correlations.

2.2 Cavity enhanced SPDC

Since quantum memories based on Pr doped solids accept a bandwidth of a few MHz, which doesn't match with the phase matching bandwidth of the SPDC process, a reduction of the linewidth is required. That can either be done by placing filtering cavities (FC) behind the SPDC process or by generating the photon pairs directly inside the cavity modes by placing the non-linear crystal inside a cavity, as in Fig. 2.3. The second option brings an enhancement B of the spectral brightness, related to the finesse F of the cavity [45].

$$B = \frac{F^3}{2F_0} \tag{2.19}$$

F is the finesse including internal losses caused by the non-linear medium L_{int} and F_0 is the finesse of the cavity without internal losses.

2.2.1 Parameters for a Bow-tie cavity

Finesse

The finesse is limited by round-trip losses and the mirrors reflectivity. For an asymmetric cavity with one lower reflective mirror for out coupling and high

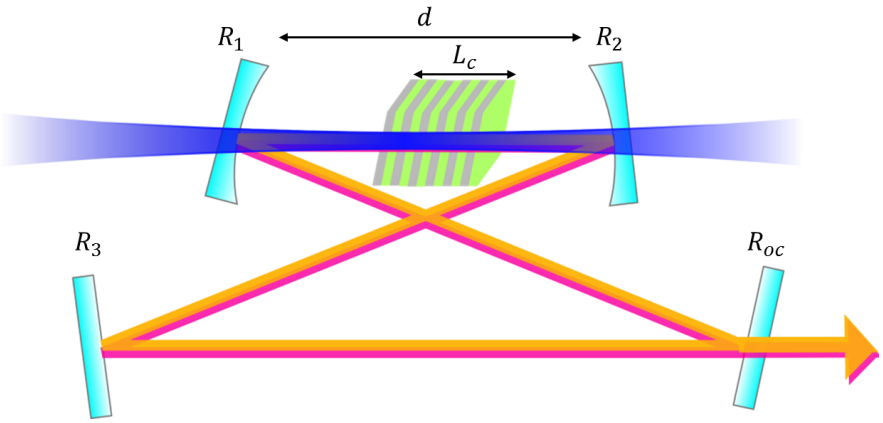

Figure 2.3: Bow-tie cavity with non-linear crystal inside creating photon pairs resonant to the cavity.

reflective mirrors the finesse can be calculated as:

$$F = \frac{\pi\sqrt{r_{oc}r_{tr}}}{1 - r_{oc}r_{tr}} \tag{2.20}$$

Here r_{oc} is the reflection coefficient and can be calculated from the reflectivity R_{oc} of the out coupling mirror $r_{oc} = \sqrt{R_{oc}} = \sqrt{1 - T_{oc}}$. The reflectivity coefficient r_{tr} includes the reflectivity of the remaining mirrors and the transmission of the medium. It can be calculated from the remaining power after one round trip of the cavity $r_{tr} = \sqrt{1 - L_{int}}$, with L_{int} the internal losses. To acquire the best trade-off between cavity enhancement and escape efficiency a good impedance matching given by $T_{oc} = L_{int}$ is required. For these assumptions the finesse simplifies to [83]:

$$F = \frac{\pi}{L_{int}} \tag{2.21}$$

Free spectral range

Another important parameter is the free spectral range (FSR) which is inversely proportional to the resonator length L_{cav}. In case of an empty ring cavity the FSR is given by

$$FSR = \frac{c}{L_{cav}} \tag{2.22}$$

Taking the crystal length L_c with the group index $n^g_{s,i}$ into account the exact FSR can be calculated as:

$$FSR = \frac{c}{L_{cav} + (L_c(n^g_{s,i} - 1))} \tag{2.23}$$

Due to dispersion the refractive indeces, and thus the FSR, for signal and idler wavelength are slightly different in the non-degenerate case. That leads to the clustering effect described in 2.2.3.

Linewidth

Given the FSR and the finesse F, the linewidth of the cavity modes can be calculated:

$$\Delta\nu_{\mathrm{FWHM}} = \frac{F}{FSR} \tag{2.24}$$

If a crystal is inserted in the cavity, the finesse is limited by internal losses, mostly in the percent range, and the remaining parameter to adjust the linewidth is the cavity length. Thus rather long cavities are required to achieve a narrow linewidth. The bow-tie design enables a long cavity path-length combined with a narrow beam waist at the crystals center. It also facilitates the elaborate locking scheme required to achieve double resonance.

Escape efficiency

The cavity escape efficiency describes the probability of a photon to exit the cavity, without getting lost beforehand (by absorption or transmittance trough high reflective mirrors). It can be calculated using the transmission of the out coupling mirror T_{oc} and the internal losses L_{int} [84]:

$$\eta_{esc} = \frac{T_{oc}}{T_{oc} + L_{int}} \tag{2.25}$$

In the impedance-matched case $T_{oc} \approx L_{int}$, the best trade off between cavity finesse and escape efficiency for the highest enhancement, it amounts 50 %.

The internal losses L_{int} cannot be measured directly. They can be estimated either from the transmission of the crystal or calculated taking into account the

Finesse and the transitivity of the out-coupling mirror: From Eq. 2.20, the following relation can be found for reflectivities close to 1 $\sqrt{r_{oc}r_{tr}} \approx 1$:

$$L_{int} = 1 - r_{tr}^2 = 1 - \left[\frac{\left(1 - \frac{\pi}{F}\right)^2}{(1 - T_{oc})}\right] \tag{2.26}$$

2.2.2 Transmission and spectral shape

The transmittance of the cavity is given by the Airy function [83]

$$A(\phi) = \frac{\sqrt{(1 - r_{oc}^2)(1 - r_{tr}^2)}e^{-i\phi}}{1 - r_{oc}r_{tr}e^{-i2\phi}} \tag{2.27}$$

with $\phi = \pi(L - L_c + nL_c)/\lambda$ for a bowtie cavity with length L and internal medium with length L_c and refractive index n. With $A^2(e^{-i\phi_{\max}} = 1)$ we get the maximal transmission of a cavity, it relies on the reflectivity of the out-coupling mirror $R_{oc} = r_{oc}^2$ and the internal losses $L_{int} = 1 - r_{tr}^2$:

$$T_{max} = \frac{(1 - r_{oc}^2)(1 - r_{tr}^2)}{(1 - r_{oc}r_{tr})^2} \tag{2.28}$$

It also allows us to express the spectral power density at the cavity output using the finesse and the FSR for the bowtie cavity as convenient parameters [83]:

$$T(\nu) = \frac{T_{max}}{1 + (\frac{2F}{\pi})^2 \sin^2(\frac{\pi\nu}{FSR})} \tag{2.29}$$

ABCD-matrix formalism

To calculate the beam properties and the stability conditions of the cavity, we used the ABCD-Matrix formalism. Each optical path and each optical element, can be expressed with a 2x2 matrix [85]. Multiplying all the matrices in between two points, one can trace the beam parameters from a starting point. The Gaussian beam parameter can be written as:

$$\frac{1}{q} = \frac{1}{R(z)} - i\frac{\lambda}{\pi\omega^2(z)} \tag{2.30}$$

The ABCD matrix for one round trip in a bow-tie cavity with starting and end point in the crystals center can be calculated as follows:

$$\begin{bmatrix} A & B \\ C & D \end{bmatrix} = \begin{bmatrix} 1 & \frac{(n_i-1)L_c+d}{2} \\ 0 & 1 \end{bmatrix} \begin{bmatrix} 1 & 0 \\ -\frac{2}{R} & 1 \end{bmatrix} \begin{bmatrix} 1 & L_{cav} - d \\ 0 & 1 \end{bmatrix} \begin{bmatrix} 1 & 0 \\ -\frac{2}{R} & 1 \end{bmatrix} \begin{bmatrix} 1 & \frac{(n_i-1)L_c+d}{2} \\ 0 & 1 \end{bmatrix} \tag{2.31}$$

The result could be obtained e.g. with Mathematica. One then can calculate the Gaussian beam parameter using following relation:

$$q_{out} = \frac{Aq_{in} + B}{Cq_{in} + D} \tag{2.32}$$

A simpler method is to calculate the beam parameters for an empty cavity and extend the length d by $d' = d + (n_i - 1)L_c$ afterward. The beam parameters don't change in that case, just the optical (and physical) length of the cavity will be stretched. Note that the FSR will be larger with the crystal inside the cavity than without.

2.2.3 Double resonant cavities and clustering effect

To receive the full enhancement described in Eqn. 2.19 the cavity has to be resonant at both, signal and idler wavelength. Due to energy conservation, expressed in Eqn. 2.1, modes are only generated if signal and idler mode are resonant to the cavity. In the non-degenerate case, where dispersion is present, signal and idler modes have a slightly different FSR which leads to an additional resonance condition. The double resonance is only fulfilled for certain modes in so called clusters [50, 58, 86], as illustrated in Fig. 2.4.

State created by cavity enhanced SPDC

The new state created by cavity enhanced SPDC contains a modified joint spectral function, which is a product of the phase matching function $h(\Delta kL)$, and the two Airy-function for the signal and idler modes [46]:

$$f_R(\omega_s, \omega_i) = f(\omega_s, \omega_i) \cdot A_s(\omega_s) \cdot A_i(\omega_i) \tag{2.33}$$

with the Airy function given in Eqn. 2.27 for signal and idler wavelength. The joint spectral intensity, expressing the spectral shape of the photons behind the cavity is given by $S_R(\omega_s, \omega_i) = |f_R(\omega_s, \omega_i)|^2$ it follows:

$$S_R(\omega_s, \omega_i) \propto \mathrm{sinc}^2\left(\frac{\Delta k(\omega_{s,i})L}{2}\right) \cdot \frac{1}{1 + (\frac{2F_s}{\pi})^2 \sin^2(\frac{\pi\nu_s}{FSR_s})} \cdot \frac{1}{1 + (\frac{2F_i}{\pi})^2 \sin^2(\frac{\pi(\nu_p - \nu_s)}{FSR_i})} \tag{2.34}$$

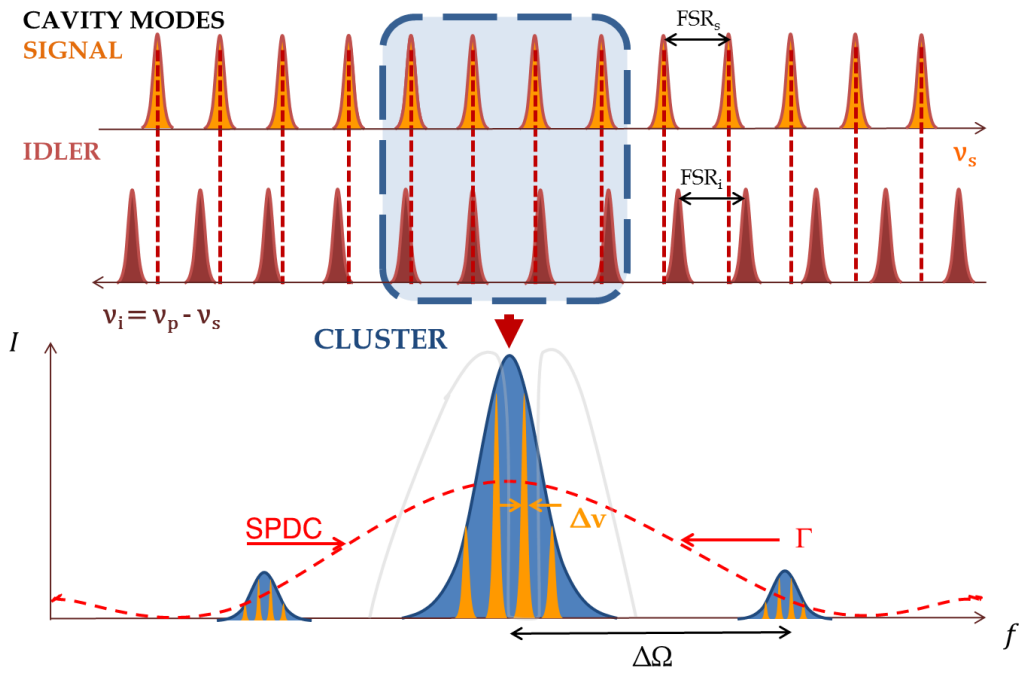

Figure 2.4: The output spectrum of a double resonant cavity is defined by the overlap of the frequency combs of signal and idler modes. In the non-degenerate case the FSR of signal and idler differ from each other due to dispersion inside the media. Modes are created inside clusters where this condition is fulfilled, in other regions the single resonant modes are suppressed. Thus the number of created modes can be strongly reduced compared to the single resonant case.

Cluster width and spacing

Looking at Fig. 2.4 the spacing $\Delta\Omega$ and the width $\Delta\Theta$ of a cluster can be derived. To get the number of modes N_m in between two clusters one can assume $N_m = \frac{FSR_s}{|FSR_s - FSR_i|} = \frac{FSR_i}{|FSR_s - FSR_i|} - 1$ and to get the spacing in between two clusters, we have $\Delta\Omega = N_m \cdot FSR_s$. This can be simplified to the following equation [50]:

$$\Delta\Omega = \frac{FSR_s \cdot FSR_i}{|FSR_s - FSR_i|} = \frac{c}{L_c} \frac{1}{|n_s^g - n_i^g|} \tag{2.35}$$

Here we see that the cluster spacing is slightly broader than the FWHM of the phase-matching bandwidth in Eq. 2.6. If just fundamental modes are supported that should result in maximally two clusters inside the phase matching bandwidth. If one cluster is centered to the maximum of the phase-matching envelope then the side clusters should be suppressed by the side-wings of the phase matching bandwidth. That is different to the Fabry-Perot design, where the photons pass the crystal two times per cavity round trip [50, 86].

The cluster width $\Delta\Theta_{\mathrm{FWHM}}$ can be calculated with

$$\Delta\Theta_i = \frac{\Delta\nu_i}{\Delta FSR} = \frac{FSR_S}{FSR_I} \frac{1}{F_i} \cdot \Delta\Omega \tag{2.36}$$

Second order cross-correlation function

Following the steps in [46] the second order cross-correlation function can be derived for a doubly-resonant cavity down-conversion:

$$\begin{aligned} G_{s,i}^{(2)}(\tau) \propto \Bigg| \sum_{m_s,m_i=0}^{\infty} & \frac{\sqrt{\gamma_s\,\gamma_i\,\omega_s\,\omega_i}}{\Gamma_s + \Gamma_i} \\ & \times \begin{cases} e^{-2\pi\Gamma_s(\tau-(\tau_0/2))}\mathrm{sinc}(i\pi\tau_0\Gamma_s) & \tau \geq \frac{\tau_0}{2} \\ e^{+2\pi\Gamma_i(\tau-(\tau_0/2))}\mathrm{sinc}(i\pi\tau_0\Gamma_i) & \tau < \frac{\tau_0}{2} \end{cases} \Bigg|^2, \end{aligned} \tag{2.37}$$

where $\gamma_{s,i}$ are the cavity damping rates for signal and idler, $\omega_{s,i}$ are the central frequencies, $\Gamma_{s,i} = \gamma_{s,i}/2 + im_{s,i}\mathrm{FSR_{s,i}}$ with mode indices $m_{s,i}$ and free spectral ranges $\mathrm{FSR_{s,i}}$, and τ_0 is the transit time difference between the signal and idler photons through the SPDC crystal.

3

Creation of ultra narrow band photon pairs compatible with solid-sate quantum memories

In this chapter, we describe the creation of ultra-narrow photon pairs compatible with solid-state quantum memories. Section 3.1 describes the characterization of the SPDC process without cavity. Section 3.2 describes the effect of the cavity setup. Results from that section are published in PRL [58]. Some text and figures are identical with the publication. In addition further measurements of the spectrum, taken after the publication are shown. At the end of this chapter results of single pass and cavity enhanced measurements are compared, showing an enhancement of the spectral brightness, due to the cavity.

3.1 Experiment: Single-pass SPDC

3.1.1 Setup

For the generation of photon pairs we use a periodically poled lithium niobate crystal (PPLN) of 2 cm length. PPLN provides a high nonlinear coefficient for the desired wavelength and promises a good conversion efficiency using Type I quasi phase matching with a poling period of 16.5 µm. In the first experiment we characterized the PPLN crystal in single pass configuration.

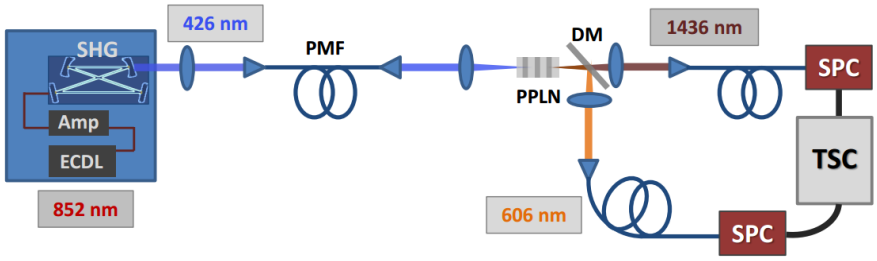

Figure 3.1: Setup for single pass spontaneous parametric down conversion: A pump laser at 426 nm creates photon pairs at 606nm and 1436 nm wavelength.

In Fig. 3.1 the setup for the single-pass configuration is shown. To generate the pump field for the SPDC process we use a commercial laser[1] at 426 nm wavelength. That laser is composed of an external cavity diode laser (ECDL) in Littrow-configuration which emits laser light at 852 nm wavelength, a tapered amplifier increases the power of the fundamental beam up to 600 mW. A second harmonic generation (SHG) unit doubles the frequency and a beam at a wavelength of 426 nm is generated. A bandpass filter[2] (center wavelength: 425 nm, bandwidth 30 nm) is used behind the laser to clean the doubled frequency from residual the fundamental one. The power of the light at 426 nm was measured to be in the range of 30 to 90 mW, depending on the alignment and cleanliness of the internal SHG-cavity.

Then the beam is coupled into a polarization maintaining single mode fiber[3] to clean the spatial mode. A good conversion efficiency of the SPDC process requires a good match with a Gaussian mode profile of the beam. Behind the fiber the beam is collimated and focused with a focal length of 500 mm into the PPLN crystal. Signal photons at 606 nm and Idler photons at 1436 nm are created and separated with a dichroic mirror behind the crystal. Each arm leads to a fiber coupled commercial single photon detector. For the photons at telecom wavelength at 1436 nm a single photon detector[4] based on an InGaAs avalanche photo diode (APD) is used. It provides a detection efficiency of 10 % and a dark

[1] Toptica SHG-100
[2] FF 425/30
[3] Thorlabs, P3-488PM-FC-2
[4] Id Quantique: ID220

count rate of 400 Hz. For the photons at visible wavelength of 606 nm a silicon based APD[1] is used, providing a detection efficiency of 60 % and a dark count rate of 50 Hz. The arrival times of the photons at the detectors are then recorded with a time stamping card[2] and coincidence histograms are evaluated with a Matlab code.

Adjusting phase matching temperature

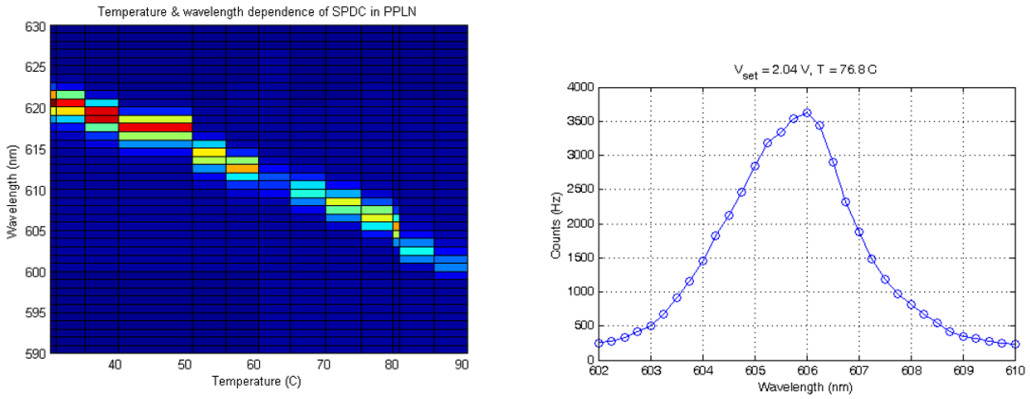

(a) temperature tuning

(b) Wavelength tuning

Figure 3.2: a) Temperature tuning of PPLN crystal. Colours represent detection rate of signal photons. At lower temperatures, photon pairs are closer to each other in wavelength. b) Temperature is fixed to the desired wavelength and coincidences are at different monochromator positions.

We need to create photons which are resonant with the Praseodymium ions of our solid state quantum memory. That requires a precise wavelength of 605.997 nm. The crystal's poling period is designed to fulfill the phase-matching conditions for this wavelength using a pump wavelength of 426.2 nm at a temperature of $T = 60\,°\mathrm{C}$. Therefore the crystal is manufactured[3] with a poling period of 16.5 µm. To obtain the required temperature the PPLN crystal is placed inside a copper mount which is heated with a Peltier-element.

[1] Perkin Elmer SPDM
[2] Signadyne: Hydra time stamp
[3] provided by hc-photonics

The wavelength of the generated photons is measured at different temperatures with a monochromator[1] (resolution: 0.2 nm). In the used configuration a broader resolution inhibited the resolvance of the phase matching bandwidth. With a temperature of 77 °C photons at 606 nm wavelength are created in the signal arm. This Temperature can vary for different incident angles of the beam on the crystal. Results of this measurement are shown in fig. 3.2.

3.1.2 Coincidence histogram

After the phase matching conditions had been optimized first coincidence measurements could be taken. The detection events of signal and idler photons are taken with our single photon counters and saved in time-stamp files, with a precision of 325 ps. The coincidence histograms are then generated with a Matlab code. Fig. 3.3 shows a measurement taken at a later stage when the cavity was setup and the out-coupler mirror was removed, to be able to compare the values directly with the cavity enhanced values. Here an integration window of 3 ns splitted in 6 time bins is selected to evaluate the coincidences and the $g_{si}^{(2)}$-values. A coincidence rate of 2800 Hz mW^{-1} was detected (see Fig. 3.4. Taking all the losses into account (detector efficiencies, transmission losses) we calculate a coincidence rate of 200 kHz mW^{-1} behind the crystal. Assuming a phase matching bandwidth of 64 GHz that results in a spectral brightness of 3 Hz mW^{-1} MHz^{-1}.

The rates in the time window in between 100 ns and 400 ns are related to accidental coincidences resulting from higher oder photon pairs, uncorrelated noise and dark counts of the detectors. One measure for the quality of the non classical state is the $g_{si}^{(2)}$-value mentioned in 2.1.4. As predicted it increases for lower powers and shows a very high non-classical correlation for the two mode squeezed state. It has its maximum of 31 000 at 9 µW. In Fig. 3.4 the coincidence rates and the $g_{si}^{(2)}$-value for powers in between 5 µW and 1 mW are shown.

3.1.3 First-order autocorrelation function

To get more information about the spectral distribution of the produced single photons we used a Michelson interferometer in the signal arm. It allows us to

[1] Horiba Jobin Yvon microHR

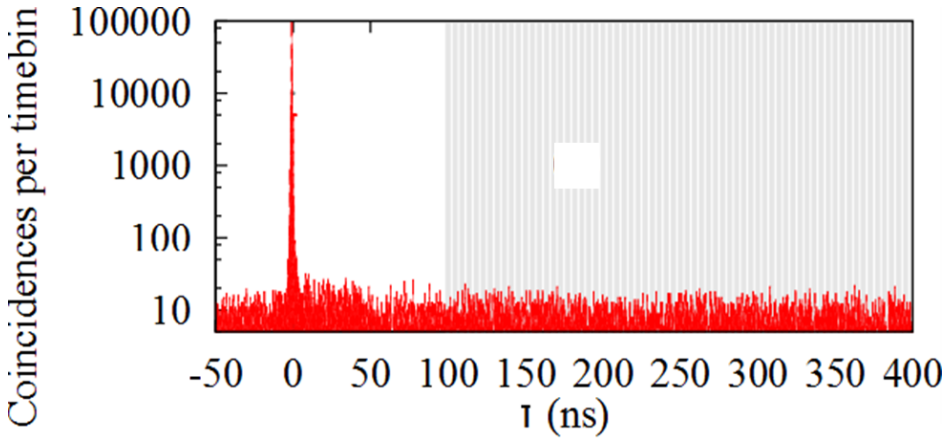

Figure 3.3: Coincidence histogram of a single-pass SPDC measurement at 40 µW of pump power. The temporal width is given by the detector time resolution and doesn't reflect the width of the photons. The shaded area is a noise window. The coincidence rate divided by the normalized count rate in the noise window results in the $g_{si}^{(2)}$-value shown.

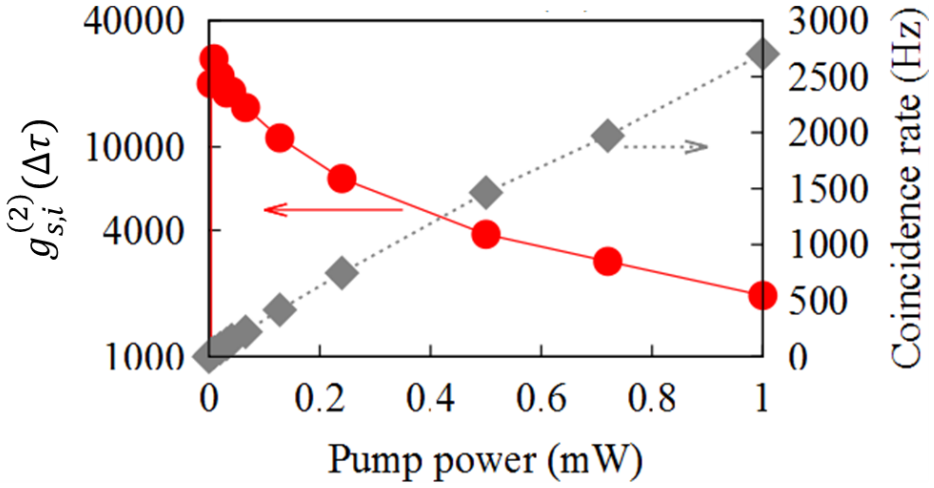

Figure 3.4: Coincidence measurements are taken at different pump powers between 5 µW and 1 mW. The obtained coincidence rate is shown as gray diamonds. The $g_{si}^{(2)}$-value is shown as red circles. It is calculated by the area containing the coincidence peak divided by the noise area, which is normalized to the width of the peak area.

investigate the temporal shape of the photons in the picoseconds range. From that we can infer the temporal shape of the photons much more accurately than it is possible with single photon counters. Using Fourier-interferometry we can infer information about the spectral shape.

Setup

In Fig. 3.5 a sketch of the setup including the Michelson interferometer is shown. For the single pass measurement the output coupler of the cavity was removed and no narrow band spectral filter was used.

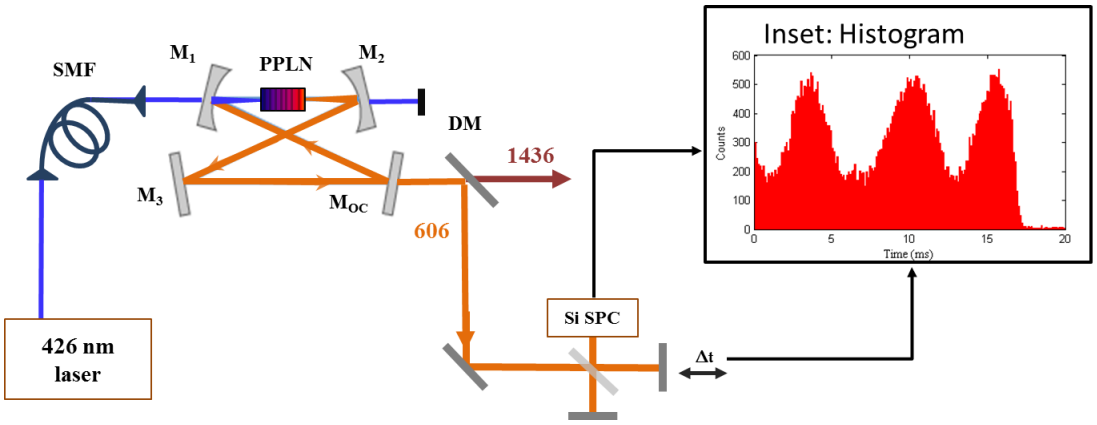

Figure 3.5: A Michelson interferometer is used in the signal arm (606nm) to achieve temporal information about the photons in the picoseconds range.

The signal arm of the source is guided to a Michelson interferometer via a single mode fiber. The Michelson Interferometer consists of a 50:50 beam splitter and two mirrors, one at each output. Depending on the phase difference of the reflected beams the photons end up with a higher probability either in the input port or in the fourth port used as output due to interference. By moving one of the mirrors forth and back with a piezo-element a continuous phase shift is created, resulting in a temporal interference pattern at the output of the beam splitter. With a translation stage[1] larger delays can be added to one of the interferometer arms. At zero delay, the visibility of the interference pattern is maximal, adding more distance to one mirror the temporal shape of the photons

[1] Standa: 7T175-150

can be investigated precisely. The photons at the output port are guided to a single photon counter. Histograms are taken with a trigger of the voltage ramp sent to the piezo as start signal and a click at the photon counter as stop signal. An example of one of these histograms is depicted in the inset of fig. 3.5. Here we can extract a visibility depending on the path length difference of the two interferometer arms.

Results

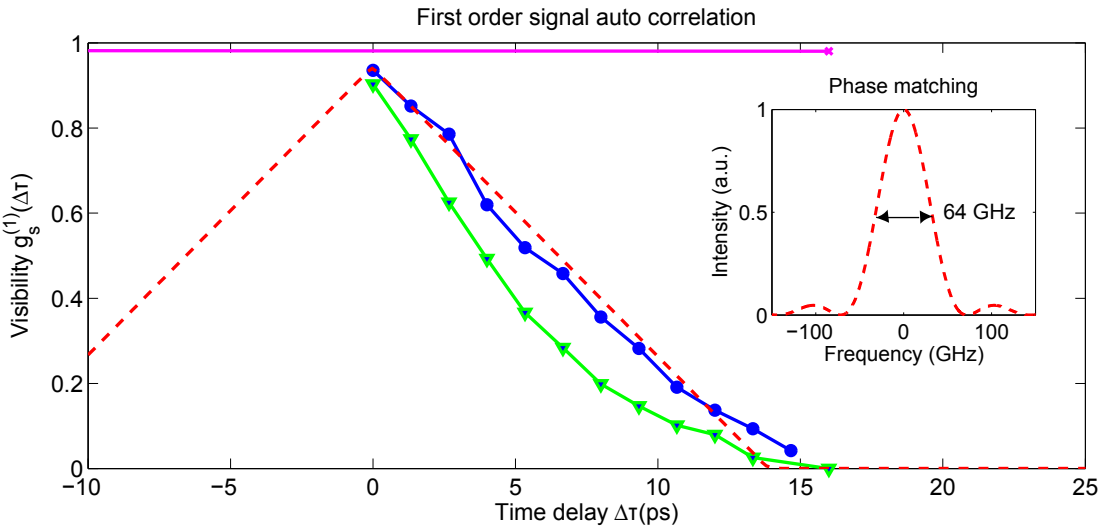

Figure 3.6: First oder autocorrelation measurement of signal photons. Visibility in green triangles take all detections of signal SPD into account. Blue bulls take just the clicks into account which are heralded by a click on the idler detector. Striped red line corresponds to a Fourier transformation of the calculated phase matching function shown in the inset. The line in magenta shows the calibration of the interferometer with classical light.

Measurements are taken with the signal and idler counters, detecting the arrival times on each detector. In the graph visibilities are plotted for all the detected photons in the signal arm (green triangles) and for the photons which are heralded by a click in the idler arm (blue bulls). The raw visibility shows a narrower temporal distribution than the conditioned one. That could be related to a broadband noise of uncorrelated photons. The conditioned visibility curve

agrees with the Fourier transformation of the phase matching function calculated with Eq. 2.6 using Sellmeier-coefficients from [87]. The calculation results in a bandwidth of 64 GHz (FWHM). The relation between time and bandwidth is given by $\Delta\Gamma = \frac{1}{\delta t}$. The used Sellmeier-coefficients agree also with the poling period of 16.5 µm provided by the crystal manufacturer[1] and the condition $\Delta k \approx 0$ (see Eq. 2.5). Using other Sellmeier-coefficients [78, 88–91] brings slightly different results.

3.2 Cavity enhanced SPDC - first generation

In this section I included text and figures from our publication. The included text parts are indented. I will comment on the publication in between and conclude it in the end.

3.2.1 Setup

> The scheme of the photon pair source is shown in Fig. 3.7. The pump for the downconversion is a 426 nm single-frequency continuous-wave laser system (Toptica TA SHG). The pump light is passing through an acousto-optic modulator (AOM) that allows for varying the pump power incident on the cavity. After the AOM the light is coupled into a single-mode fiber (SMF) for spatial mode cleaning. The SPDC process is based on Type I quasi-phase-matching in a 2 cm long periodically poled lithium niobate crystal (5 % MgO doped PPLN with 16.5 μm poling period, AR-coated for 426, 606, 1436 nm, provided by HCPhotonics Corp.) The bow-tie cavity surrounding the crystal has finesse $\mathcal{F} \approx 200$, and free spectral range $FSR \approx 414$ MHz. The mirror reflectivities for signal and idler wavelength are 99.99 % for $M_{1,2,3}$, and 98.5 % for the output coupler (M_{OC}, Layertec GmbH).

[1] hc photonics

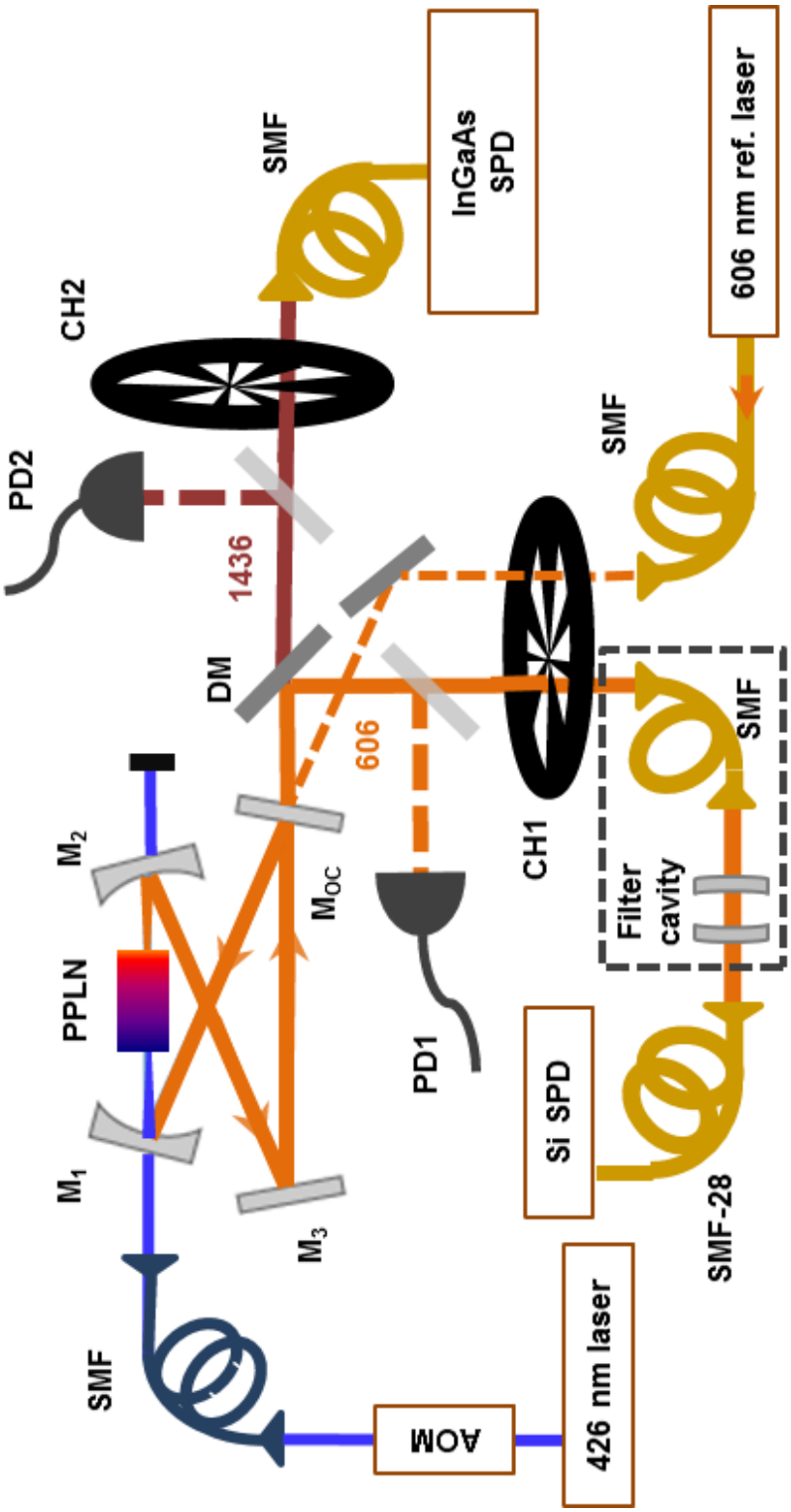

Figure 3.7: Experimental setup. AOM, acousto-optic modulator; SMF, single-mode fiber; $M_{1,2,3}$ highly reflective mirrors; M_{OC} output coupler mirror; DM, dichroic mirror; PD1,2, photodiodes detecting partial beam extracted with glas plates; CH1,2, choppers; SPD, single-photon detectors.

Beam waist and mode matching

For an optimal conversion efficiency the beam waist in the crystals center has to be 18.5 µm, according to the Boyd-Kleinmann parameter (see section 2.1.3). In addition a long resonator length of $L \approx 64$ cm is required to achieve the targeted linewidth of 2 MHz with the given finesse. For that reason we chose a bow-tie cavity. The mirrors in the short arm, surrounding the crystal have a radius of curvature of 100 mm while the mirrors in the long arm are plane.

The distance d of the two curved mirrors can be varied, considering the stability conditions of the cavity (11.1 cm $\gg d \gg$ 12.8 cm for our cavity). The created signal and idler modes have to match the cavity mode. In case of mode mismatch, transversal modes will be created and reduce the efficiency in the desired TEM_{00}-mode at the cavity output.

Since the beam waist are wavelength dependent and the cavity normally supports just one mode it is very challenging to find a good mode matching for both signal and idler modes. A good mode matching is achieved for the signal wavelength (see Fig. 3.8). At the idler wavelength it was not possible to remove all the transversal modes.

mode	λ [nm]	ω_0 in crystal [µm]	d_B at M_{oc} [µm]
pump	426	18.5	-
signal	606	18.5	1040
idler	1436	18.5	2470

Table 3.1: calculated beam parameters for optimal mode matching

Cavity stabilization

In order to obtain enhancement of the photon pair generation probability, resonance for both the signal (606 nm) and idler (1436 nm) frequencies has to be ensured. In addition, the signal frequency has to be resonant with the Pr^{3+} ions. To achieve these conditions a complex lock system was implemented. A reference beam at 606 nm, resonant with Pr^{3+} ions [92], is coupled into the cavity through M_{OC},

co-propagating with the pump beam. The reflection from the cavity is used for locking the cavity length at resonance with the signal frequency, by means of a piezo element moving M_{OC}. To derive an error signal for the lock we use a Pound Drever Hall scheme. To this end, the reference laser is modulated by 12.5 MHz with an electro optical modulator (EOM). We mix the Signal of PD1 with the local oscillator and feed this to a micro-controller where a PID regulator is implemented the voltage for the piezo.

A reference beam at the idler frequency is obtained by difference-frequency generation between the pump (426 nm) and the 606 nm reference beam and is used for locking the pump frequency to maintain double resonance.

To this end the pump laser frequency is modulated by an acousto optic modulator (AOM) with a frequency of around 30 kHz. As in the Pound Drever Hall scheme, the modulation frequency is mixed with the detected DFG-signal. A difference to the previous stabilization scheme is that the detected signal is created inside the cavity, such that a reflected signal can not be detected. Thus the modulation frequency has to be much lower than the line width of the cavity. In this way, an error signal can be obtained and after passing through a second micro-controller with an implemented PID regulator, a correction signal is applied to the frequency of the pump laser. In that sense the pump laser and the idler frequency are locked to the frequency of the reference beam. Small drifts of the reference beam are then applied to the other two frequencies.

The lock system is acting during 45 % of the total operation time, alternating with the measurement time, separated by mechanical choppers (CH1,2). During the measurement time no classical reference signal beam is present in the cavity to protect the single-photon detectors (SPD) and avoid excessive noise. The downconverted photons are spectrally filtered, fiber coupled (SMF-28: single-mode at 1436 nm, and slightly multi-mode at 606 nm) and detected by SPDs (Si SPD: Perkin Elmer SPCM-AQR-16-FC with detection efficiency, $\eta_{\mathrm{det},606} \approx 60\,\%$; InGaAs SPD: IdQuantique id220 used in free-running

mode with $\eta_{\mathrm{det},1436} \approx 10-20\,\%$). The measured transmission from the output of the cavity to the SPDs is 0.46 (0.31) for the 606 (1436) nm photons.

3.2.2 Source preparation

The reference beams are used to align the cavity. First the cavity is aligned to the reference beam at 606 nm, with a beam-diameter close to the calculated diameter of the signal mode. For that purpose, we scan the cavity length and display the transmission signal obtained with a photo diode on an oscilloscope, the transmission peaks for the resonant condition ($L = n \cdot \lambda$) can be identified. In Fig. 3.8 a typical transmission signal is plotted.

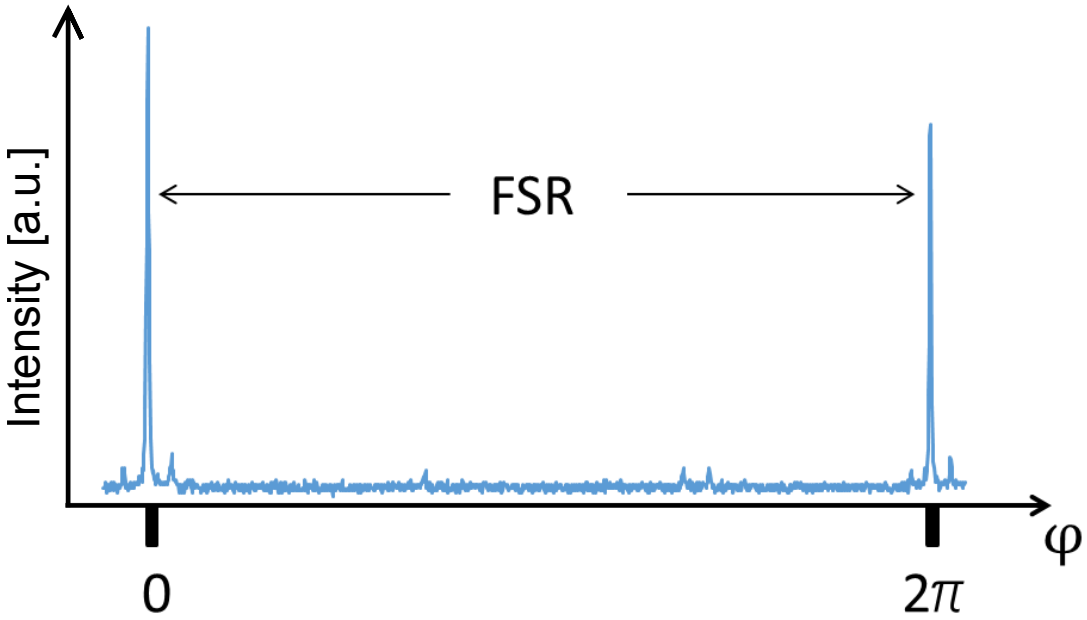

Figure 3.8: Cavity transmission of the reference beam at 606 nm, while the cavity length is scanning over one FSR. The two main peaks show the transmission at the desired resonance. The two small peaks beside are sidebands introduced by an EOM for Pound-Drever-Hall locking. The three small remaining peaks in the center are due to imperfect mode matching.

Then the pump beam at 426 nm is brought to overlap with the reference beam.

With a highly sensitive InGaAs-photodiode, the created beam at 1436 nm can be detected. The temperature of the crystal can be tuned to maximize the signal created by DFG.

Temperature dependence

The phase-matching bandwidth is sensitive to the temperature of the non-linear crystal. To investigate this sensitivity the intensity of the beam created by DFG is measured with a photo diode behind the cavity, while the temperature was changed in a range from 62.5 °C to 67 °C. Results are shown in Fig. 3.9.

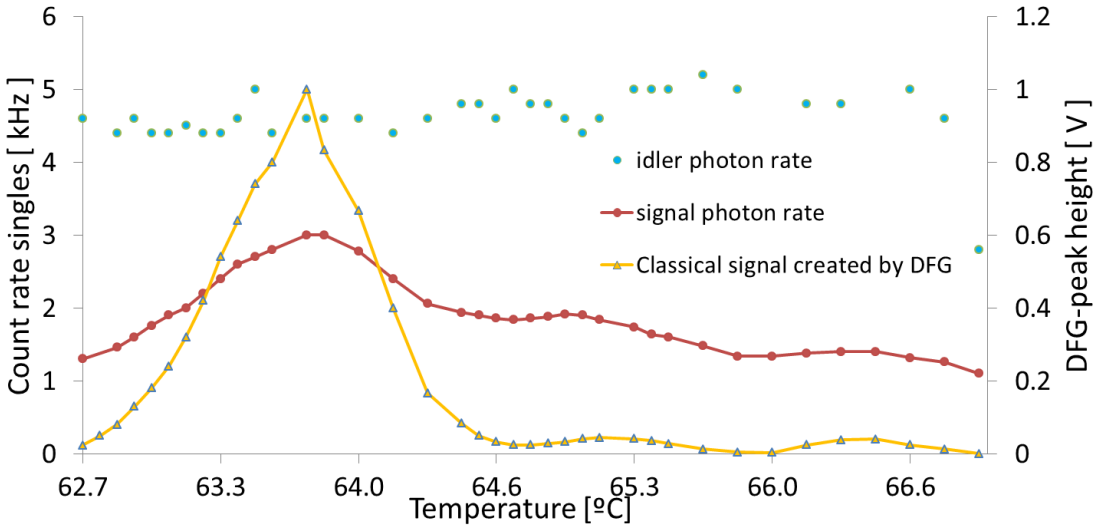

Figure 3.9: Yellow triangles: power of DFG signal, detected with a photo diode. Red points: Count rate of 606 photons, filtered with an etalon. Green points: Count rate of idler photons.

The behavior of the expected $sinc^2$ function can be identified and a (FWHM) of $\Delta T_{\mathrm{FWHM}} = 0.8\,^{\circ}\mathrm{C}$ is measured. The idler photon rate is measured without any spectral filter. It shows that the number of created photons is independent from the temperature setting. The signal photons are spectrally filtered with an etalon centered to the frequency of the reference light. The etalon has a bandwidth of 6 GHz and a finesse of 10. The signal photon rate shows an oscillation with temperature with the same period as the phase matching temperature. It can be

deduced that the phase matching of the generated photon pairs behaves in the same way as the phase matching of the DFG-signal.

3.2.3 $g_{si}^{(2)}$-measurements

The quantum state of the emitted photon pairs can be analyzed by the second-order cross-correlation function in between the signal and idler fields, $G_{s,i}^{(2)}(\tau)$, as described in Eq. 2.37 in chapter 2.

> To do so, the frequency non-degenerate photons of the pair are spatially separated by a dichroic mirror (DM) and their arrival times at the detectors are recorded by a time-to-digital-converter card (TDC, Signadyne). To create the correlation function, the arrival-time differences (τ) are plotted in a histogram, as shown in Fig. 3.10. We observe a FWHM correlation time of 104 ns, which, to our knowledge, is the highest value reported for a SPDC source so far.

At the time of writing this thesis, only one SPDC source with a longer correlation time has been developed, but without any single mode filtering so far [93].

> The double exponential decay of $G_{s,i}^{(2)}(\tau)$ is due to the photon lifetime inside the cavity and allows for the estimation of the cavity linewidth, $\Delta\nu$. Fitting $\exp(-2\pi\Delta\nu\tau)$ on the two sides of the correlation function results in $\Delta\nu = 1.7\,\mathrm{MHz}$ at 1436 nm and 2.9 MHz at 606 nm. The asymmetry is a clear sign of the difference of the finesse for the two wavelengths which can be explained by a slight difference in the reflectivities of the mirrors or the crystal surfaces. From these values we infer internal cavity losses of $1 - 2.5\,\%$ and cavity escape efficiencies of $\sim 0.6 - 0.4$ [57].

At a later stage, described in 5.2.1, I measured a slightly higher reflectivity for the out-coupler mirror, which leads to escape efficiencies of 55 % and 30 %. The escape efficiency is the main limitation for the heralding efficiency, which is crucial for advanced experiments like the spin wave storage.

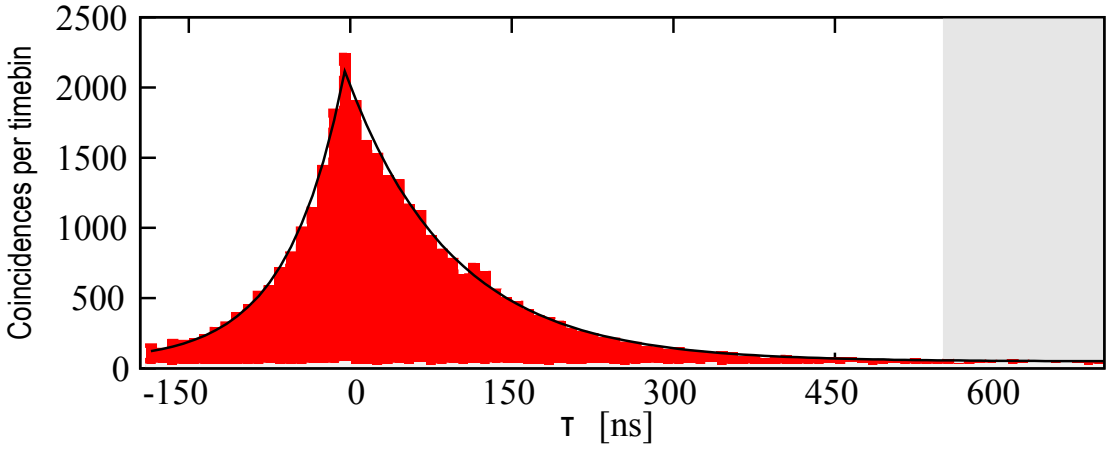

Figure 3.10: Measured correlation functions of the unfiltered photon pair source. $G^{(2)}_{s,i}(\tau)$ function (measured at 130 μW pump power, $\eta_{\mathrm{det},1436} = 10\,\%$, 43 min integration time, 10 ns timebin size). The dark count rate (light grey bars) is obtained by blocking the InGaAs SPD. $g^{(2)}_{s,i}(0)$ is calculated using the fit function (solid line) as the peak value divided by the accidental region (shaded area) average count rate level.

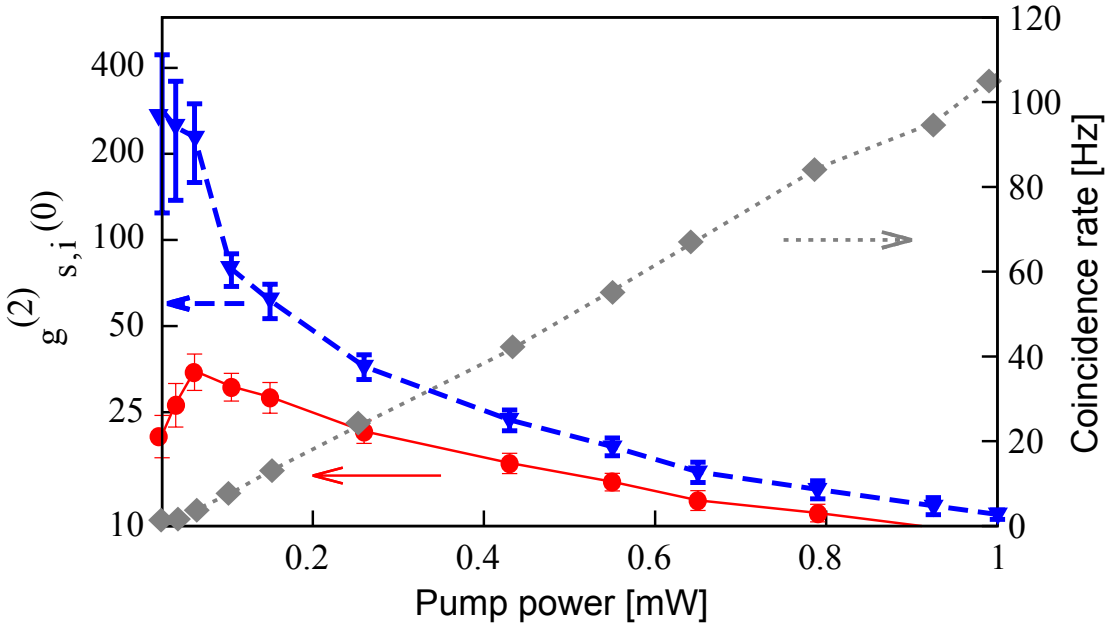

Figure 3.11: Power dependence of $g^{(2)}_{s,i}(0)$ without and with dark count subtraction (left axis, circles and triangles, respectively) and coincidence count rates (right axis, diamonds).

To further characterize the source, the histograms were measured at various pump power levels. The number of total coincidences within a 500 ns time window increases linearly with pump power (see Fig. 3.11). The detected pair production rate after dark count subtraction is $C = 92\,\mathrm{Hz/mW}$. For applications in quantum information science, another critical parameter is the normalized cross-correlation function at zero delay, $g^{(2)}_{s,i}(0)$, which is also plotted in Fig. 3.11 as a function of pump power. In order to obtain good fidelities in quantum protocols, high $g^{(2)}_{s,i}(0)$ is needed. As expected, $g^{(2)}_{s,i}(0)$ is inversely proportional to the pump power [52]. Without subtracting any background, we reach values of $g^{(2)}_{s,i}(0)$ up to 35, significantly higher than the classical threshold of 2 for two-mode squeezed states. For a pump power of 1 mW, we still observe $g^{(2)}_{s,i}(0) = 9.3$. At very low power (below $100\,\mu$W) the measurements are limited by dark counts, reducing $g^{(2)}_{s,i}(0)$ [94]. The $g^{(2)}_{s,i}(0)$ with dark count subtraction (also plotted) approaches a value of 284 at $24\,\mu$W, showing the high purity of our photon pair source.

As a possible application of the photon pair source, the telecom photons could be used to herald the presence of the 606 nm photons to be absorbed by the QM. To give an estimate for the heralding efficiency (η^H), the singles count rate at the InGaAs SPC (S_{1436}) has to be taken into account, resulting in $\eta^H = C/S_{1436}/\eta_{\mathrm{det},606} = 13\,\%$.

The coincidence value given in that paragraph correspond to a spectrum containing several spectral modes. For a single mode output the numbers would be significantly lower due to spectral filtering.

$g^{(2)}_{s,i}(0)$-values at zero-time delay an infinitesimal small time window is obtained from a fit. These values hold for the violation of the classical boundary $g^{(2)}_{s,i}(0) \leq 2$, but to measure coincidences a broader integration window is required. In further experiments we refer to the $g^{(2)}_{s,i}(\Delta\tau)$-value, which is obtained by the coincidences measured in a time window Δt divided by the accidental coincidences normalized to the same window size. In that case the $g^{(2)}_{s,i}(\Delta t)$-value is strongly dependent

on the window size Δt and is just a lower bound for the comparison with other non-classical light sources, which refer to a $g^{(2)}_{s,i}(0)$-value.

3.2.4 Spectral content of photon pairs

In the following section we use three methods to investigate the spectrum of the photon pairs. First we use an estimation obtained from oscillations found in out $g^{(2)}_{si}$ measurements. Then we measure the cavity enhanced spectrum with an Michelson interferometer as explained in Sec. 3.1.3. Finally, we use a scanning Fabry-Perot cavity to visualize the photon spectrum. The expected spectrum containing several clusters is explained in Sec. 2.2.3.

Spectrum estimated from $g^{(2)}_{si}$ measurement

A first insight on the spectral content of the emitted photons can be inferred from the $G^{(2)}_{s,i}(\tau)$ function. As shown in Fig. 3.12, the histogram taken with 325 ps timebin size shows an oscillatory behavior. This is the consequence of the presence of multiple spectral modes [55]. The periodicity follows the cavity round-trip time ($T = 1/FSR = 2.4$ ns), as the photon wavepacket incorporates the beating from several frequency components spaced by the FSR.

From the temporal width of the peaks (~ 880 ps) and taking into account the time resolution of the detection system (~ 685 ps), we infer that the spectrum is composed of clusters containing around 4 longitudinal modes (see fig. 3.13). This technique is however limited to a few GHz by the detection time resolution.

In Fig. 3.13 simulated $G^{(2)}_{s,i}(\tau)$ functions are plotted as a function of time delay (τ) normalized to the cavity round-trip time (T). The different curves correspond to different number of spectral modes taken into account. As the number of modes is increased, the superposition of the sinc functions results in the oscillation peak width's (Δt) reduction. This effect is also shown in Fig. 3.14. Taking into account the time resolution of our detection system (~ 685 ps) we can estimate the expected temporal width of the peaks by convolution. From

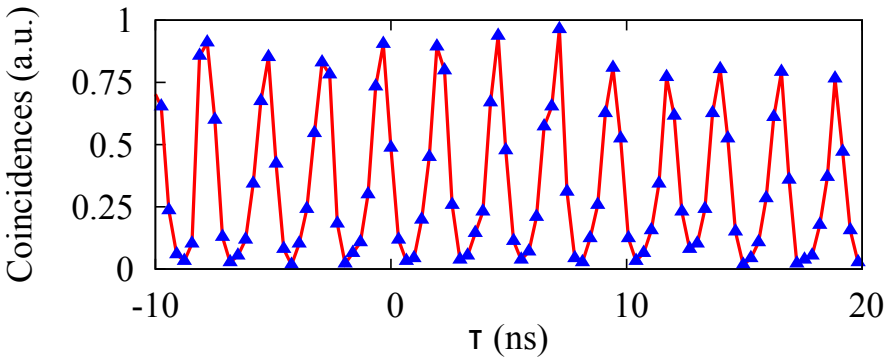

Figure 3.12: Temporal oscillations in the $G^{(2)}_{s,i}(\tau)$ correlation function for the unfiltered photon pair source. Here a zoom of Fig. 3.10 to the $-10-20$ ns region evaluated with 325 ps timebin size is shown.

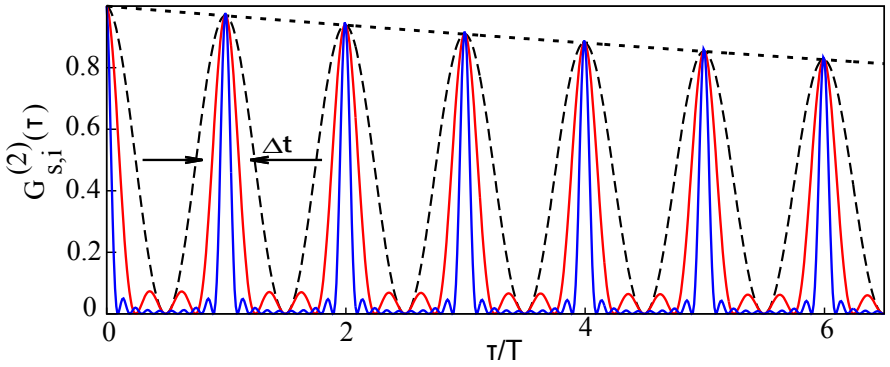

Figure 3.13: Dependence of the $G^{(2)}_{s,i}(\tau)$ function on the number of spectral modes. Correlation functions for 1, 2, 4, and 10 modes (dotted, dashed, red solid, and blue solid lines, respectively).

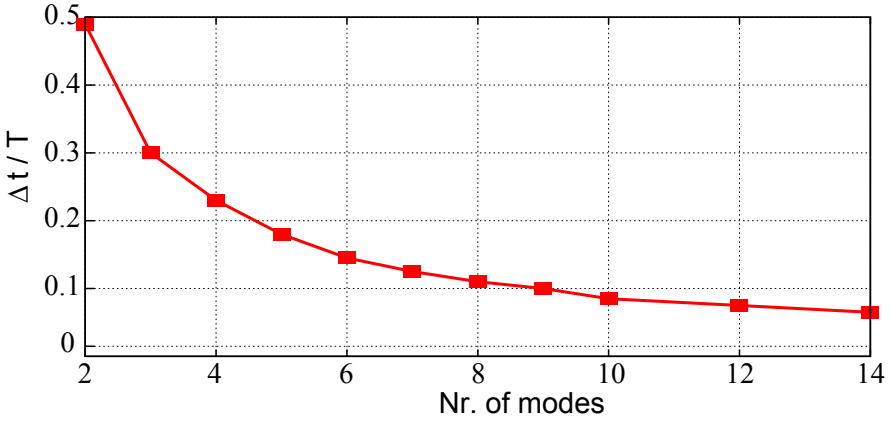

Figure 3.14: Width of the oscillation peaks versus the number of modes.

the best agreement when changing the number of modes we infer that the spectrum is composed of clusters containing around 4 longitudinal modes (peak width $\sim 880\,\mathrm{ps}$). Note that this corresponds to 4 modes of equal height, which is physically not the case, but their contribution to the peak width should be similar.

Spectrum obtained from $g_s^{(1)}$-measurements with Michelson-interferometer

Here we use the same setup as depicted in Fig. 3.5 and the method described in Sec. 3.1.3. This time the out-coupling mirror completes the cavity, such that at its output the cavity enhanced spectrum is generated. In Fig. 3.15 the results without any narrow-band filter are shown (apart from a longpass filter at 532 to remove residual pump light and a broad bandpass filter[1]).

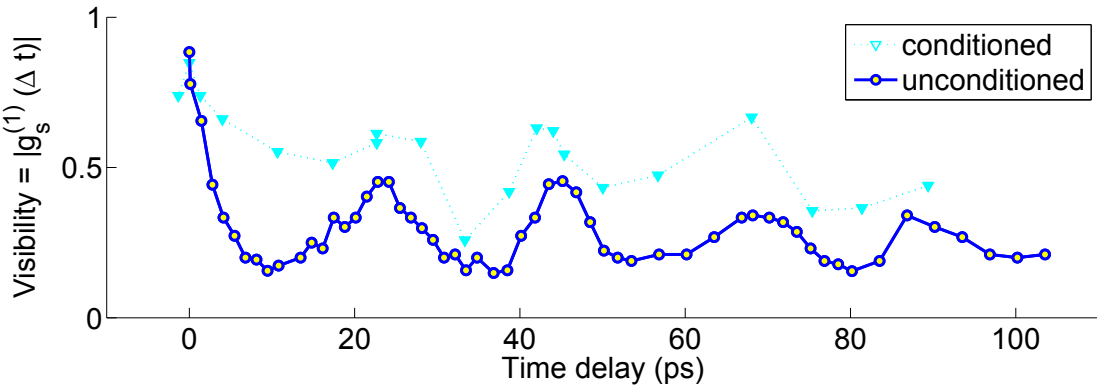

Figure 3.15: $G_s^{(1)}$-measurement of spectrally unfiltered signal photons copled into a single mode fiber. Blue circles show raw visibilities obtained by single rates. Cyan triangles show visibilities of signal photons condition on an click at the idler detector. Idler photons are spectrally unfiltered and coupled into a single mode fiber.

The measurement with the blue circles shows the uncorrelated auto-correlation as presented in [58]. The measurements of the cavity enhanced $g_s^{(1)}$-correlation show oscillations with a periodicity of 22.5 ps. This shows that there are few clusters with a spectral spacing around 44.5 GHz. This spacing does not agree with the theory presented in 2.2.3, which predicts a cluster spacing of $\Delta\Omega =$

[1] Thorlabs: FB600-40

$0.885 \cdot \Delta\Gamma = 72\,\mathrm{GHz}$ with just one central cluster. One reason could be that the used Sellmeier-coefficients are inaccurate, but on the other hand they match well with the measurements shown in Fig. 3.6 and the calculated poling period of the crystal. Another reason could be that the measured side clusters are created by higher order transversal modes, which are also prominent in the light created by DFG. The cyan triangles in Fig. 3.15 show a measurement conditioned on the clicks of the heralding detector. It was taken at a later stage, but the unconditioned data reproduce the previous data well. Here the visibility is much higher because we get rid of the effect of uncorrelated noise. The high visibility seems to be more constant, which could result from an additional spatial filtering in the idler arm due to the coupling into a single mode fiber[1].

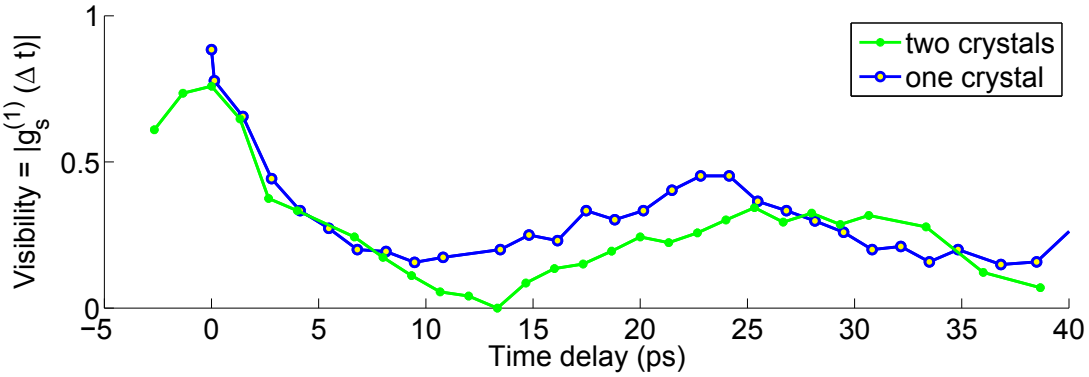

Figure 3.16: Comparison of $G_s^{(1)}$-measurements with one (blue circles) and two crystals (green dots) of 2 cm length each inside the cavity. The second crystal is not used for photon generation, but as dispersion element.

In Fig. 3.16 an measurement is shown, when a second PPLN crystal of 2 cm length was placed in the long arm of the cavity. There the pump beam was not passing, but was used as additional dispersion element for signal and idler photons. This measurement was taken with a slightly changed cavity configuration as used in chapter 5. Here we see a slightly larger oscillation period of roughly 28 ps, which corresponds to a cluster spacing of 35.7 GHz and agrees with the theory taking the doubled dispersion delay into account.

[1] Thorlabs: SMF28

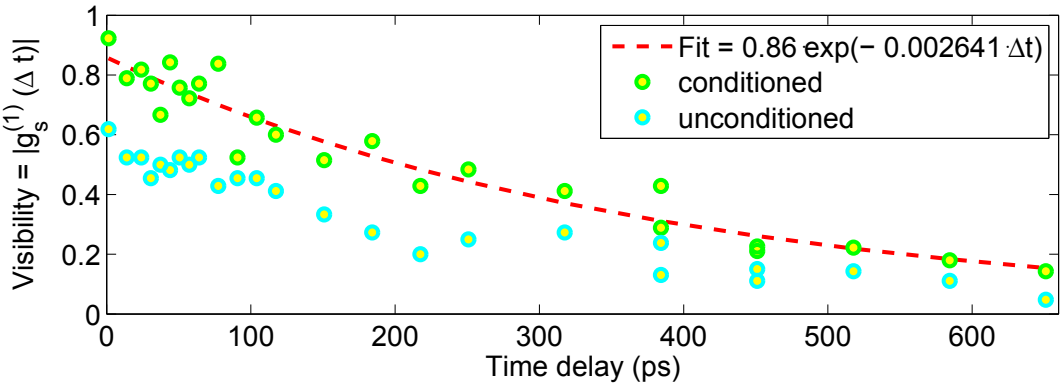

Figure 3.17: $G_s^{(1)}$ of photons spectrally filtered with an Etalon of 6 GHz bandwidth suppressing possible side clusters. Cyan circles show visibilities of unconditioned signal photons. Green circles show visibilities of photons conditioned on an idler click. The stripped red line is an exponential fit.

In Figure 3.17 further measurements with an Etalon (FSR=60 GHz, finesse≈ 10) in the signal arm to remove additional clusters from the spectrum are shown. The fitted decay results in a cluster width of $\Delta\Theta = \frac{1}{\pi\Delta t} = 1.55\,\text{GHz}$.

3.2.5 Scanning cavity

Another method to get direct information about the spectrum is to use a scanning Fabry-Perot interferometer. By applying a voltage ramp on a piezo behind one of the mirrors and triggering the photon detections on the trigger of this ramp, we can get a direct picture of the spectrum created by the source. A scan at the main clusters position is shown in Fig. 3.18.

The width of the peaks can not be resolved by the Fabry-Perot cavity, which has a line width of 80 MHz and a FSR of 16.8 GHz. Here the cluster width is roughly $\Delta\Theta \approx 1.2\,\text{GHz}$

3.2.6 Single mode operation

The multi-mode cavity could in principle be used as the source for storage of several longitudinal modes within the inhomogeneous absorption line of a Pr^{3+} QM, to implement frequency multiplexing.

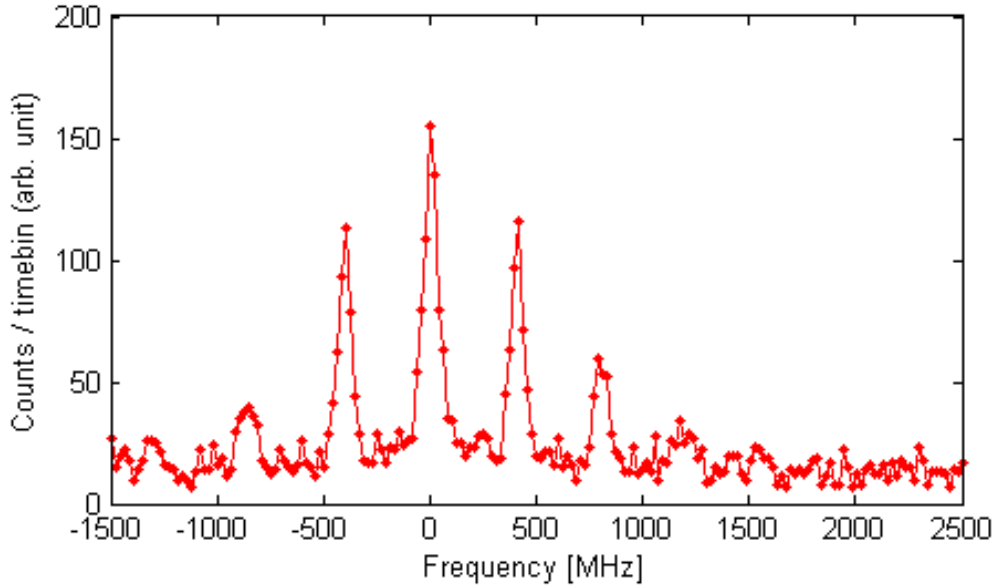

Figure 3.18: Spectral measurement of central cluster taken with scanning Fabry-Perot cavity.

Nevertheless, in absence of a frequency multi-mode QM, it is important to show that our source can also operate in the single-mode regime. To achieve this, we inserted a filter cavity (FC) in the 606 nm arm, designed to suppress all modes around the fundamental one. The FSR was chosen such that the transmission peaks do not coincide with the neighboring clusters ($\Delta\nu = 80\,\mathrm{MHz}$, $FSR = 16.8\,\mathrm{GHz}$). The FC transmission for long term measurements was 11 %, including a peak transmission of 22 % (fiber-to-fiber) and a further drop of 50 % due to frequency drifts of the only passively stabilized FC. For this measurement, a single-mode fiber was inserted in the 606 nm arm (with reduced fiber coupling compared to the unfiltered cavity experiments ($\eta_C = 0.5$ and 0.8, respectively)).

The measured $G^{(2)}_{s,i}(\tau)$ function of the signal transmitted by the FC and the unfiltered idler is plotted in Fig. 3.19. We obtain a raw $g^{(2)}_{s,i}(0)$ of 9. Note that a significant part of accidental coincidences are due to the fact that only the signal photon is filtered. The number

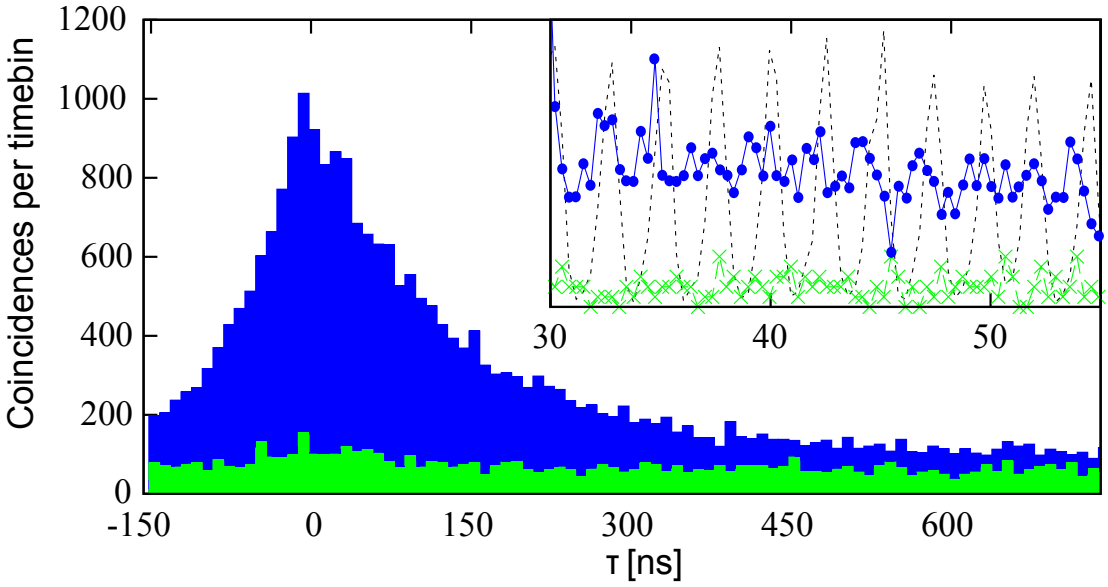

Figure 3.19: Measured correlation function of the cavity output when the signal was spectrally filtered. $G^{(2)}_{s,i}(\tau)$ function (1.7 mW pump power, $\eta_{\mathrm{det},1436} = 20\,\%$, 60 min integration time, 10 ns timebin size). The noise level (light green) was measured with FC off-resonant with the signal. The inset is a zoom to the $30 - 55$ ns region evaluated with 325 ps timebin size. The dashed line corresponds to the unfiltered case for comparison.

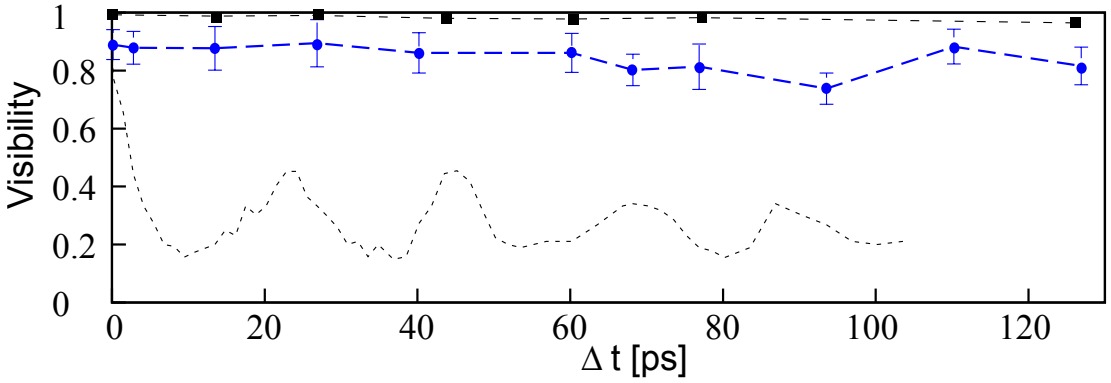

Figure 3.20: $|g^{(1)}_s(\Delta t)|$ function measured with 606 nm down-converted photons after dark count subtraction (circles). As reference, the visibility for classical light (squares), and for the unfiltered cavity (dotted line) are plotted.

of coincidences (500 ns window) with the background level subtracted is 2.9 Hz/mW. Comparing with the unfiltered cavity – correcting for the different experimental conditions – we find a reduction of 4.6 for the coincidence rate which is consistent with the number of modes estimated from the unfiltered experiment.

The suppression of the oscillations at 2.4 ns for the filtered signal (inset of Fig. 3.19) confirms the suppression of neighboring spectral modes within the same cluster. The suppression of modes in the neighboring clusters was also tested by measuring the $|g_s^{(1)}(\Delta t)|$ for the filtered signal, see Fig. 3.20. The visibility is above 80 % over the 120 ps range (average $\sim 88 \pm 5\,\%$) and there is no sign of decay over this range. This leads to the conclusion that the neighboring clusters were also suppressed efficiently. The combination of $G_{s,i}^{(2)}(\tau)$ and $|g_s^{(1)}(\Delta t)|$ measurements is a strong evidence of the presence of a single spectral mode in the signal. Note that only a single filtering stage is needed to reach the single-mode regime.

The spectral brightness corresponding to the probability of finding a pair in single-mode fibers (i.e. correcting only for detection efficiencies) for the filtered source is 11 pairs/ (s·mW·MHz). Correcting for all known losses after the creation of the photon pair we find $8 \cdot 10^3$ pairs/ (s · mW · MHz), which shows that passive loss is a major issue to be improved. Compared with the single-pass case, where we measure a coincidence rate of 3000 Hz/mW (for $\eta_{\mathrm{det},1436} = 0.1$), the cavity enhances the spectral brightness by B = 1250 [45] (correcting for filter transmission, cavity escape efficiencies and chopper duty-cycle).

To compare the achieved enhancement with the theoretical enhancement factor the finesse without crystal was measured $F_0 = 416$. According to Eq. 2.19, the theoretical enhancement factor at the cavity output is 2300 (corrected for escape efficiencies).

3.3 Conclusions

In conclusion, we designed, built and characterized a quantum light source which is suitable to connect solid state Pr^{3+} QMs to fiber optics networks. This is an important step towards long distance quantum repeaters using solid state QMs. Beyond this application, our source is also a proof-of- principle that cavity-enhanced down-conversion can be used as a versatile source of narrow-band photon pairs at widely separated wavelengths, which is relevant in the context of connecting light-matter quantum interfaces of different kinds. In the following chapter experiments show the storage of quantum light in a solid state Pr^{3+} QM.

3. CREATION OF ULTRA NARROW BAND PHOTON PAIRS COMPATIBLE WITH SOLID-SATE QUANTUM MEMORIES

4

Quantum storage of a heralded single photon in a Pr doped crystal.

In this chapter we use the source presented in chapter 3 for experiments with a Pr^{3+}:Y_2SiO_5 crystal as storage device. The goal is to store one photon of the pair (signal), whose presence is heralded by the other photon (idler), as a collective optical atomic excitation. For that purpose, we use the atomic frequency comb (AFC) protocol [95]. The storage experiments show non-classical correlation between the two photons for storage times up to 4.5 μs. That is more than 20 times longer than what was observed with non-classical light in previous solid state experiments [32, 33]. The content of this chapter was published in Physical Review Letters [73]. That work is the results from the connection of the photon pair source with the storage device and includes several different setups like coherent light preparation and stabilization, preparation of the memory and preparation and stabilization of the photon pairs. The memory and coherent beam was built up and investigated by Mustafa Gündogan in collaboration with Patrick Ledingham and Margaritha Mazzera and prepared by Kutlu Kutluer. The publication was mainly written by M. Mazzera and H. de Riedmatten. This chapter contains a text from that publication, which is marked as quotation (indented). My main contributions were the preparation and stabilization of the source, the connection of the two setups and the data taking.

The AFC scheme [30] relies on the creation of a series of narrow absorption peaks with periodicity Δ in a transparency window created within the inhomo-

geneous absorption profile of the crystal (see Fig. 4.2). The single photon is then mapped onto the absorption profile, leading, in the ideal case, to a single collective optical excitation [32, 33]. This is a superposition of one exited rare earth ion (further describes as atom) and many ions in the ground state which can be described as:

$$\sum_{j=1}^{N_A} e^{-i\vec{k_p}\cdot\vec{x_j}} e^{-i\delta_j t} |g_1 \cdots e_j \cdots g_{N_A}\rangle \tag{4.1}$$

, where N_A is the number of atoms, $|g\rangle$ and $|e\rangle$ are the ground and excited state, respectively, $\vec{k_p}$ is the single photon wave vector, and $\vec{x_j}$ (δ_j) is the position (detuning) of atom j. In that sense a single photon interacts with a group of spatially delocalized atoms at several separated frequencies in a range covered by the bandwidth of the photon. Initially the collective excitation undergoes an inhomogeneous dephasing. Since the ions are at several equidistant frequency positions, due to the comb shown in Fig. 4.2, they will rephase after a time $\tau = 1/\Delta$ inverse to spacing of the peaks inside the comp giving rise to a re-emission of the photon in the forward direction, the so called AFC echo [31]. Hence the photons are stored in the excited state of the atoms with a predetermined storage time, which can be controlled by the preparation of the comb.

4.1 Setup

4.1.1 preparation beam

Figure 4.1 represents the experimental setup. The coherent light at 606 nm is obtained using a periodically poled $KTiOPO_4$ (PPKTP) waveguide (AdVR, Inc.) by means of sum frequency generation (SFG) of 1570 nm and 987 nm light. The sources for these are amplified diode lasers (Toptica, DL 100 pro and TA PRO, respectively) [96]. The frequency of the 606 nm light is locked with the Pound-Drever-Hall technique to a temperature stabilized cavity assembled in a home-made vacuum chamber (2×10^{-7} mbar). The cavity has a finesse $\mathcal{F} \approx 787$ and a free spectral range (FSR) of 1 GHz, leading to a bandwidth

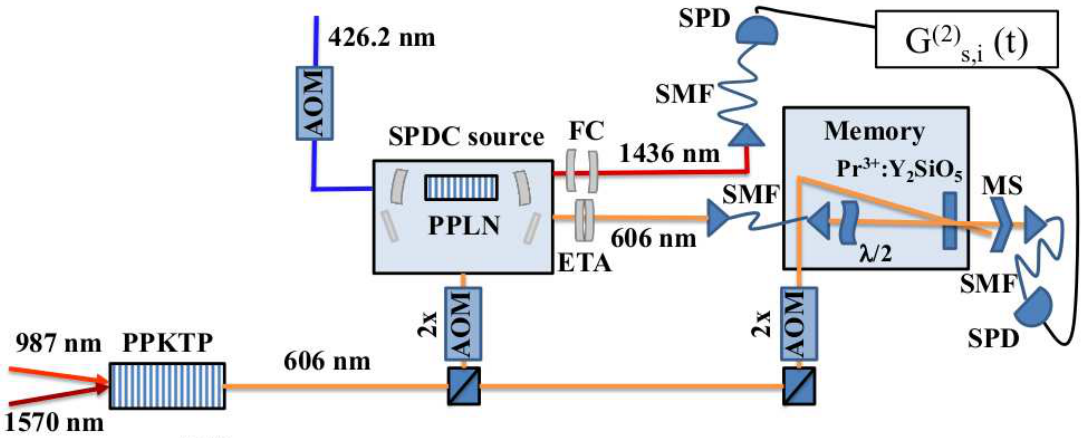

Figure 4.1: Simplified scheme of experimental setup. AOM, acousto-optic modulator (2x when double pass); FC, filter cavity; ETA, etalon; SMF, single-mode fiber; MS, mechanical shutter; SPD, single photon detector; $\lambda/2$, half-wave plate.

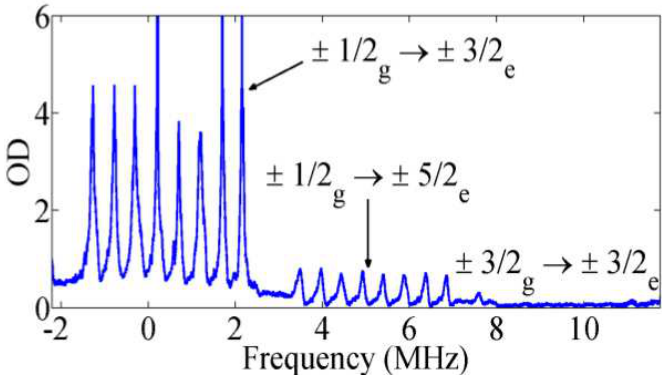

Figure 4.2: Example of AFC with $\Delta = 500\,\text{kHz}$.

of 1.27 MHz. Two beams are spatially separated, the first being used as a frequency reference for the photon-pair source [58] and the second for the memory preparation [96]. Their frequency and amplitude are varied by double-pass acousto-optic modulators (AOMs) driven by an arbitrary waveform generator (Signadyne). After the AOMs, the beams are coupled into polarization maintaining single-mode fibers (SMFs) and out-coupled in two separated optical benches hosting the source and the cryostat (closed cycle cryogenic cooler, Oxford V14), which is exploited to cool the Pr^{3+}:Y_2SiO_5 crystal down to 2.8 K.

4.1.2 Photon pair source

The heralded single photons are obtained from the photon-pair source, whose detailed description is given in the previous sections. A CW pump beam at 426.2 nm (Toptica, TA SHG), modulated by an AOM, produces photons at 606 nm (signal) and 1436 nm (idler) by SPDC in a temperature-stabilized PP lithium niobate (LN) crystal. A bow-tie cavity surrounding the crystal enhances the SPDC process for the resonant frequencies. The cavity is stabilized with the reference beam at 606 nm, to ensure the signal resonance with the Pr^{3+}:Y_2SiO_5 crystal. At the same time, to maintain the cavity resonant with the idler, the pump frequency is locked using light at the idler frequency created by difference frequency generation of the pump and the 606 nm reference beam. The double resonance allows a very efficient suppression of the redundant spectral modes due to the so called clustering effect [58]. The photon-pairs' spectrum is composed of a main- and two secondary-clusters separated by 44.5 GHz, each containing four longitudinal modes [58]. In order to operate in the single-mode regime, the heralding telecom photons are filtered by a home-made filter cavity (FC, linewidth 80 MHz and FSR 16.8 GHz, mirrors from Layertec GmbH). An etalon (Finesse $\approx$ 10 and FSR 60 GHz, LightMachinery) is placed in the signal arm as well, resulting in the mere suppression of the secondary-clusters. Further suppression of the unwanted spectral modes within the main-cluster is provided in the 606 nm arm by the inhomogeneously broadened absorption profile of Pr^{3+}. The correlation time of the photon-pair is measured from the signal-idler cross-correlation function $G^{(2)}_{s,i}(t)$ to be $\tau_c = 108$ ns, corresponding to a photon bandwidth of $\delta\nu = 2.3$ MHz (1.84 MHz) for the signal (idler) photons [58]. In order to protect the single photon detectors (SPDs) from the reference beams and to avoid excess noise, the lock and the measurement times are alternated (with 45 % duty cycle) by mechanical choppers. The telecom photons are detected immediately after the FC by a InGaAs SPD (IdQuantique id220, de-

tection efficiency $\eta_{d,i} = 10\,\%$ and 400 Hz dark count rate) and are used to herald the creation of the 606 nm photons, which are sent to the memory via a SMF. The optical transmission of the signal (idler) photon from the output of the bow-tie cavity to the cryostat (SPD) is $\eta_s = 0.18$ ($\eta_i = 0.18$). To optimize the detection of the stored and retrieved photons, we switch off the pump beam using the AOM after the detection of an idler photon (500 ns before signal photon is re-emitted by the crystal), thus interrupting the creation of new photon-pairs.

4.1.3 Quantum storage

Our storage device is a 3 mm thick Y_2SiO_5 sample doped with a Pr^{3+} concentration of 0.05 %. The relevant optical transition is at 605.977 nm with a measured absorption coefficient of $\alpha = 23\,\mathrm{cm}^{-1}$ and an inhomogeneous linewidth of 5 GHz [96]. A half-wave plate ($\lambda/2$) ensures the polarization of the photons to be aligned close to the optical D_2 axis of the crystal, in order to maximize the absorption [97]. To prevent noise from the strong preparation beam polluting the single photon mode, we use two different optical paths with an angle of 2.5 degrees. The maximum power in the preparation mode before the cryostat window is 6 mW and the beam diameter at the crystal is 150 μm. The beam diameter for the input mode is 50 μm. The single photon mode is directed to a Si-SPD (Excelitas Technologies, efficiency $\eta_{d,s} = 40\,\%$ and 10 Hz dark counts) via a SMF with 60 % coupling efficiency. A mechanical shutter is employed to protect the SPD during the preparation of the spectral features (300 ms long); the duty cycle is 50 %.

To prepare the memory we follow the procedure thoroughly described in [96, 98]. We prepare a transparency window within the inhomogeneously broadened Pr^{3+} absorption at 606 nm by sweeping the laser frequency by 12 MHz. The comparatively narrow transparency window contributes to select only one mode among the four

remaining in the main-cluster of the source spectrum and are separated by 412 MHz [58]. Afterwards we tailor a single class AFC on the $\pm 1/2_g - \pm 3/2_e$ transition by first burning back atoms with pulses at frequencies differing by Δ and then performing a cleaning sweep in the region of the $\pm 3/2_g - \pm 3/2_e$ transition (see Fig. 1.3). To ensure the efficient absorption of the photons by the periodic structure, the total comb-width is set to 3.5 MHz (see Fig. 4.2 for an example with $\Delta = 500$ kHz). With the present preparation procedure we are able to tailor spectral features as narrow as 60 kHz. The input photon frequency is selected to be resonant with the $\pm 1/2_g - \pm 3/2_e$ transition.

The arrival times of the photons to the detector are recorded with a time-stamping card (Signadyne) and used to reconstruct the second-order cross-correlation function between signal and idler $G^{(2)}_{s,i}(t)$. A figure of merit for the non-classical nature of the photon correlations is the normalized cross-correlation function [12, 32]

$$g^{(2)}_{s,i} = \frac{p_{s,i}}{p_s p_i}, \tag{4.2}$$

where p_s (p_i) is the probability to detect a signal (idler) photon and $p_{s,i}$ the probability to detect a coincidence in a time window $\Delta t_d = 400$ ns centered at zero time delay. All the results presented in this paper are from raw data, without any background or dark count subtraction.

4.2 Characterization - heralded single photons

We first characterize the input heralded single photon by sending it through the memory crystal when only a transparency window is created (see green histogram centered at zero time delay in Fig. 4.3). The values of $g^{(2)}_{s,i}$ as a function of the pump power P_p are plotted in Fig. 4.5 (a). Despite the expected decrease for increased pump powers, the values remain well above the classical limit of 2 (dotted line) for two-mode squeezed states.

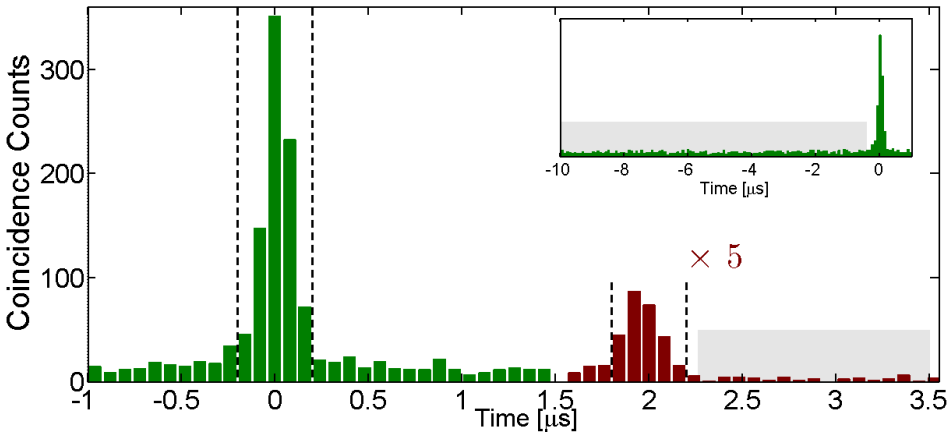

Figure 4.3: $G^{(2)}_{s,i}(t)$ histogram without (green) and with (red) AFC. The preprogrammed storage time is $2\,\mu$s and the power of the 426.2 nm pump is 2 mW. The dashed lines and shaded area define the detection windows for the coincidences ($\Delta t_d = 400$ ns) and noise, respectively, used to compute $g^{(2)}_{s,i}$.

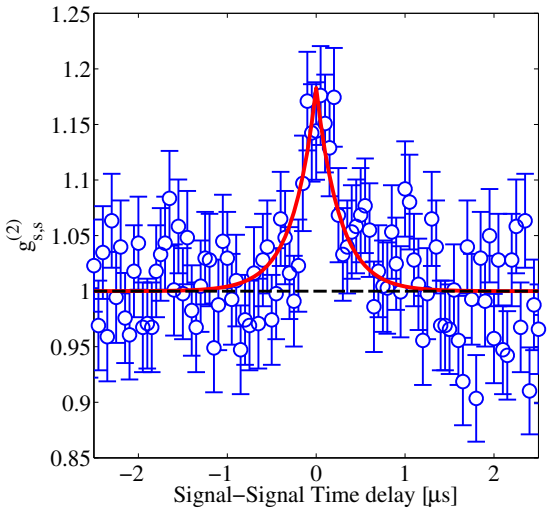

Figure 4.4: Normalized second-order autocorrelation function of the signal photons. The pump power is 5 mW and the integration time is 18 hours. The time-bin size is 50 ns. The error bars are calculated according to Poissonian statistics.

In order to unambiguously confirm the non-classical nature of the correlation, we also measure the marginal auto-correlation function for the signal and idler mode, $g^{(2)}_{s,s}$ (see Fig 4.4) and $g^{(2)}_{i,i}$. We find, at pump power of 5 mW, $g^{(2)}_{s,s} = 1.14 \pm 0.03$ and $g^{(2)}_{i,i} = 1.07 \pm 0.02$, leading to strong violation of the Cauchy-Schwarz inequality in the form $R = (g^{(2)}_{s,i})^2/(g^{(2)}_{i,i} \times g^{(2)}_{s,s}) = 61 \pm 3 \not\leq 1$.

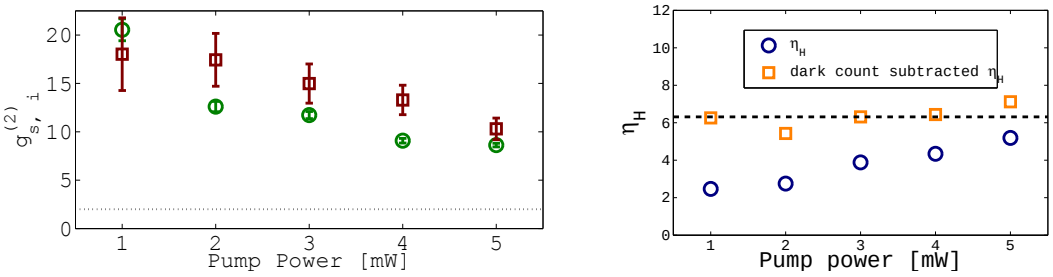

(a) crosscorrelation (b) heralding efficiency

Figure 4.5: The $g^{(2)}_{s,i}$ values as a function of the pump power for the AFC echo (empty squares) are compared to those for the input photons (empty circles). The heralding efficiencies η_H are also reported (filled triangles).The integration times range between 30 and 60 minutes. The error bars are evaluated from the raw number of counts assuming Poissonian statistics. The dotted line corresponds to the classical limit $g^{(2)}_{s,i} = 2$ for two-mode squeezed states.

The detected coincidence rate (within Δt_d) is $C_d = (0.83 \pm 0.14)$ Hz/mW. From this value, we infer the generated coincidence rate C_g at the output of the cavity $C_g = C_d/(\eta_i \cdot \eta_{d,i} \cdot \eta_s \cdot \eta_{loss} \cdot \eta_{d,s}) = 3.4$ kHz/mW, where $\eta_{loss} = 0.225$ is the transmission from the input of the cryostat to the signal SPD, including the duty cycle of the memory. We can also evaluate the heralding efficiency in front of the cryostat, $\eta_H = p_{s,i}/(p_i \times \eta_{d,s} \times, \eta_{loss})$, whose values as a function of P_p are reported in Fig. 4.5(b) (full triangles). η_H is mainly limited by η_s and dark counts in the heralding SPD. Subtracting the contribution of the 1436 nm detector dark counts we find heralding efficiencies almost constant, ${\eta_H}^{DC} \approx 6.3\,\%$, over the whole range of pump powers investigated. Finally, we estimate that more than 95 % of the heralded

signal photons detected after the crystal are resonant with the atoms [57].

4.3 AFC storage experiments

Once the non-classical nature of the input photons propagating through the transparency window is demonstrated, we prepare the AFC and reconstruct the $G^{(2)}_{s,i}(t)$ function for the stored and retrieved photons. Figure 4.3 includes the coincidence histogram when an AFC is producing a collective re-emission at a delay of $\tau = 2\,\mu s$ (orange trace). The values of $g^{(2)}_{s,i}$ for the AFC echo as a function of the P_p are reported in Fig. 4.5(a) (empty squares). The count rate in the region of the AFC echo is $C = (0.043 \pm 0.03)\,\mathrm{Hz/mW}$. We observe that the echoes exhibit $g^{(2)}_{s,i}$ values higher than the input photons. We attribute this unexpected effect to the fact that the AFC acts as a temporal filter [99] for non-resonant noise arising from the SPDC source. Since a break of 20 µs for the pump of SPDC process after the detection of an idler photon is introduced, the AFC delays the signal to a region free of broadband noise, thus increasing the $g^{(2)}_{s,i}$. When the pump power decreases, the detection of the echo is limited by the detector dark counts. This gives rise to a saturation of the echo $g^{(2)}_{s,i}$ values which hides the filtering effect of the storage.

In view of applications in temporally multi-mode quantum memories with on-demand read-out, the pre-programmed delay τ must be tunable to allow the application of control pulses transferring the excitation to the spin states [96]. Thus, we changed the spectral periodicity Δ of the AFC to obtain increased delays. Figure 4.6 shows the coincidence histograms in the region of the AFC echo occuring at different predetermined storage times. The AFC storage efficiency, η_{AFC}, is estimated by comparing the number of counts of the input propagating through the transparency window and the echo; it decreases for longer delays, as shown in Fig. 4.7, denoting a reduction of the comb finesse [31]. We note that the AFC efficiency with single

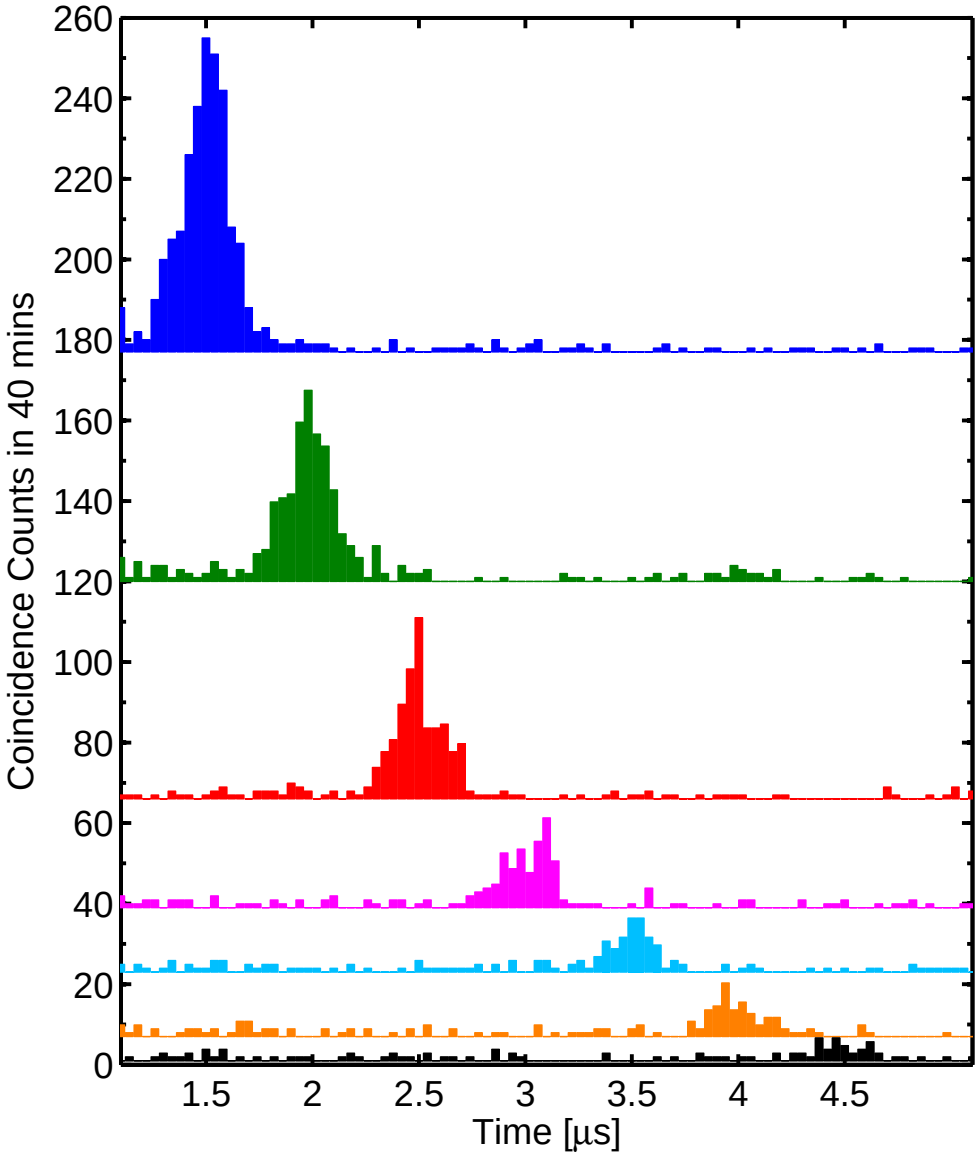

Figure 4.6: AFC echoes at different predetermined storage times observed in coincidence histograms measured at 2 mW pump power (integration time is 40 minutes and the time-bin size is 5 ns). The curves are vertically shifted for clarity.

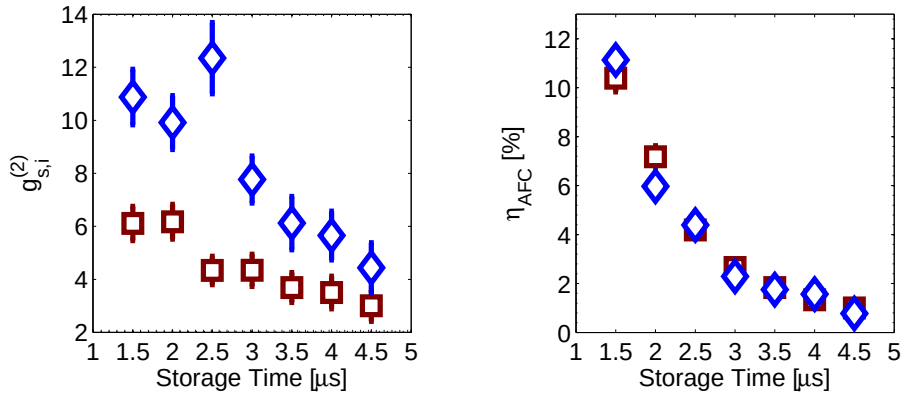

Figure 4.7: AFC efficiency and $g^{(2)}_{s,i}$ (calculated in a 400 ns window) of the AFC echo as a function of the storage time. Diamonds: filter cavity in the heralding photon path; squares: filter cavity removed from the heralding photon path. The error bars are evaluated from the raw counts assuming Poissonian statistics. The dotted line corresponds to the classical limit $g^{(2)}_{s,i} = 2$ for two-mode squeezed states.

photons does not decrease with respect to the storage of bright pulses or weak coherent states at the single photon level. This confirms that there is no significant frequency jitter for the single photons. Compared to previous experiments of single photon storage in solid state devices based on other materials [32, 33], we could reach AFC storage times more than 20 times longer, while preserving non-classical correlations (see Fig. 4.7). As we stop the production of pairs after the detection of a telecom photon, the region where the echo lies should not be affected by unconditional noise coming from the source due to the mentioned break of the pump beam after a heralding click. Thus, despite the reduction in the AFC efficiency, the echo should exhibit constant values of $g^{(2)}_{s,i}$ for increasing storage times. As a matter of fact, the decrease in the $g^{(2)}_{s,i}$ values while increasing the storage time is less pronounced than the drop of the AFC efficiency (see Fig. 4.7) and we attribute the reduction to the limitation given by the detector dark counts.

We also report the values of η_{AFC} and $g^{(2)}_{s,i}$ measured without the

FC in the idler arm. The efficiencies in the two cases agree within the experimental error. On the contrary, despite the factor 2 gain in the raw number of counts thanks to the reduced passive losses, the $g^{(2)}_{s,i}$ without FC decreases due to the frequency multimodality of the source [58]. In fact, among the four modes coexisting in the main-cluster, only one is resonant with the AFC. The non-resonant modes in the idler arm join the start signals for the coincidence histogram without corresponding stops (the Pr^{3+} absorption acts as a filter for the non-resonant mode in the 606 nm arm), thus decreasing the heralding efficiency and contributing to the noise increase. Note that frequency multiplexed quantum light storage could be obtained by creating several AFCs at different frequencies separated by the SPDC cavity FSR [24].

4.4 Conclusion

In conclusion, we have demonstrated the reversible mapping of heralded single photons to collective optical atomic excitations in a praseodymium doped crystal. We observed an increase of non-classical correlations between signal and idler photons during the storage, thanks to a temporal filtering effect due to the AFC. Storage times up to 4.5 μs while preserving quantum correlations were observed, more than 20 times longer than previous solid state experimental realizations. Furthermore, the transition used would readily allow the transfer of the excitation to the ground state to obtain long-lived spin-wave storage of quantum state of light, provided that the noise induced by the control beams can be sufficiently reduced. At time of the publication that was the longest storage reported for a heralded single photon in a solid state device.

Since the work has been published the memory characteristics has been improved. A new PhD student, Alessandro Seri, applied changes to increase the efficiency of the memory and the available storage time. The Pr^{3+}:Y_2SiO_5 crystal has been replaced by a longer one (5 mm) in order to increase the OD. In addition different methods of optical pumping were tested to increase the quality of the AFC and thus the efficiency. With this improved memory, an efficiency of

17 % has been reached for a storage time of 5 µs in the excited state. In Figure 4.8 a comparison of the improvement with the here presented data is shown.

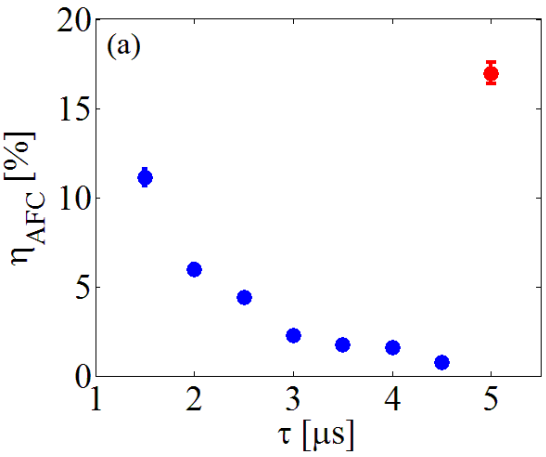

Figure 4.8: Improved efficiency in red compared with data from two years earlier.

4. QUANTUM STORAGE OF A HERALDED SINGLE PHOTON IN A PR DOPED CRYSTAL.

5

Second generation source for spin state storage

5.1 Introduction

The characterization of the source presented so far was obtained before we stored the heralded signal photons in the excited state of the praseodymium ions. Here a narrow line width was important. For storage experiments in the long lived spin state another crucial requirement is to achieve a high heralding efficiency. The heralding efficiency is the probability of finding a heralded signal photon at a certain position, e.g. in front of the detector or at the memory input, conditioned on the click of the heralding detector. It can be calculated using a coincidence measurement:

$$\eta_{her_s} = \frac{C}{S_i \cdot \eta_{det_s}} \tag{5.1}$$

with the detected coincidences C, the single rate of the idler photons S_i, corrected for the detection efficiency η_{det_s} of the signal counter and eventually any transmission in between the position and the detector.

Achieving a high heralding efficiency is important in view of reaching high signal-to noise ratio in the storage and retrieval of single photons. For that purpose, it is indeed required that $\eta_{her} \cdot \eta_{QM} \gg p_N$, where η_{QM} is the storage and retrieval efficiency of the quantum memory, and p_N is the noise probability in the photon mode, due to the control pulses required for spin-wave storage. Obtaining

a high value of heralding efficiency from the quantum light source therefore helps relaxing the requirement on noise and efficiency of the memory.

In order to achieve a sufficient high heralding efficiency it is important to minimize the uncorrelated noise in the idler arm, therefore we use the mentioned filter cavity in addition with a bandpass filter[1]. It is also required to maximize the transmission in the signal arm. One factor which has a major effect on the heralding efficiency is the cavity escape efficiency η_{esc}. It is addressed in the next section.

5.2 Modified setup

A sketch of the experimental setup can be found in Fig. 5.1. The setup, including the pump laser[2] at 426 nm and the elaborate locking scheme is already described in chapter 3. Here the cavity length was readjusted to match the cavity geometry with a modified beam waist inside the crystal for better efficiency. The distance d between the curved mirrors became 11.8 cm. That resulted in a FSR of 423 MHz. The pump beam focus inside the crystal was adjusted, by replacing lens L2 (f = 100 mm*insteadof*f=400 mm) to increase the internal conversion efficiency. The new cavity parameters can be found in Tab. 5.1.

L_{cav} [cm]	L_c [cm]	d [cm]	r [mm]	ω_c [µm]
68.7	2	11.75	100	18.5

Table 5.1: Final parameters of bowtie cavity with L_{cav}: total cavity length, L_c: crystal length, d: distance between curved mirrors, r: radius of curved mirrors, ω_c: beam waist in crystals center.

The 606 nm reference beam is now created by a commercial laser system[3], which provides a better stability and a higher output power than the previously used sum frequency generation described in Sec. 4.1.1. In the signal arm a new Etalon (linewidth 4.25 GHz, FSR 100 GHz) is used for better suppression of the side clusters.

[1] Omega optics: 1440BP14/25
[2] Toptica TA-SHG 110
[3] Toptica TA-SHG pro

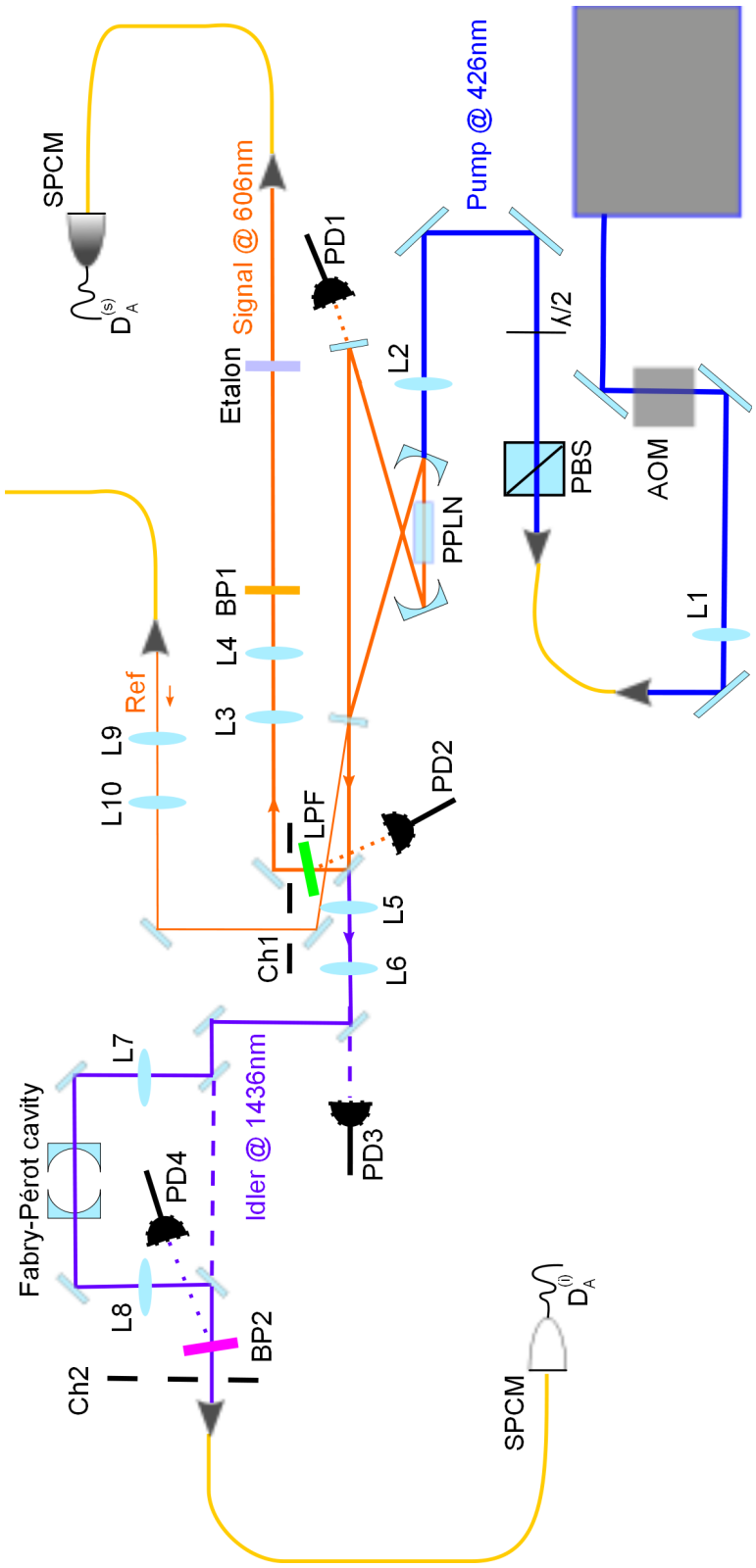

Figure 5.1: Experimental setup of final source with AOM: acusto optic modulator, L1 - L10: lenses, PBS: polarizing beam splitter, $\lambda/2$: half-waveplate, PPLN: Bowtie cavity surrounding PPLN crystal, PD1 - PD4: Photodiodes, LPF: Longpass filter, BP1 - BP2: bandpass filters, Ch1 - Ch2: Choppers, Etalon and Fabry-Perot cavity for spectral filtering, SPCM: single photon counter modules. The lenses have following focal lengths': $f = -75\,\mathrm{mm}$: L10 $f = -50\,\mathrm{mm}$: L1,L3,L5,$f = 75\,\mathrm{mm}$: L4, L6, $f = 100\,\mathrm{mm}$: L2, $f = 200\,\mathrm{mm}$: L7,L8,L9

The filter cavity was placed in the idler arm for all shown measurement in a free space configuration, instead of a previously fiber coupled version, to increase the transmission and the detected count rate. By using flippable mirrors it is still possible to do 'multimode' measurements without filter cavity. In addition a new stabilization-circuit was implemented. A part of the cavity transmission signal is captured with photodiode PD4. It is digitalized with a ADC ant processed with a micro controller. A modified C code generates a correction signal to keep the transmission high and after passing a DAC sent to the piezo behind the rear mirror of the Fabry-Perot cavity.

5.2.1 Increasing the escape efficiency

The cavity escape efficiency describes the probability of an photon to exit the cavity, without getting lost beforehand (by absorption or transmittance trough high reflective mirrors). It can be calculated using the transmission of the out coupling mirror T_{oc} and the internal losses L_{int} [84]:

$$\eta_{esc} = \frac{T_{oc}}{T_{oc} + L_{int}} \tag{5.2}$$

In the impedance-matched case $T_{oc} \approx L_{int}$, the best trade off between cavity finesse and escape efficiency for the highest enhancement, it amounts 50 %. Higher escape efficiencies reduce the spectral brightness at the cavity output and lead to an increased the bandwidth of the photons. The cavity finesse was measured without crystal resulting in $F_0 = 416 \pm 6.3$, and the transmission of the out-coupling mirror was measured to be 1.06(2) % for the signal wavelength. With the inserted crystal a finesse of ($F^{(s)} = 172$) is obtained by the linewidth of the signal photons. From Eq. 2.20, the following relation can be found for reflectivities close to 1 $\sqrt{r_{oc} r_{tr}} \approx 1$:

$$L_{int} = 1 - r_{tr}^2 = 1 - \left[\frac{\left(1 - \frac{\pi}{F}\right)^2}{(1 - T_{oc})} \right]$$

That results in an internal loss of 0.4 % without crystal and 2.6 % with crystal for the signal photons. For the idler wavelength the transmission of the out coupler is supposed to be $T_{oc}^{(i)} = 1.35\,\%$, provided by the data sheet. A finesse of

$F^{(i)} = 257$ is obtained from the photon linewidth. That results in internal losses of 1.1 % for the idler photons including the crystal. The different losses come from absorption in the nonlinear crystal which differ significantly for our signal and idler wavelengths [100].

The calculated finesse, the escape efficiency and the cavity enhancement factor at the output are plotted in Fig. 5.2 as function of the transmission of the out-coupling mirror. We see that with the present mirror escape efficiencies of 30 % for signal and 55 % for idler photons are obtained.

For the best trade off between enhancement and escape efficiency the transmission of the out coupling mirror should be at least as high as the internal loss. Here we are more interested in increasing the escape efficiencies and therewith the heralding efficiency for both photons. That implies to reduce the reflectivity of the output coupler. However, this also increases the cavity linewidth, and therefore the photon bandwidth, which would ultimately lead to a decrease in storage and retrieval efficiency in the quantum memory, due to the limited memory bandwidth. Finally, we chose a reflectivity of 97 %, leading to a calculated escape efficiency of 53 % for the signal and 73 % for the idler photon.

5.2.2 Transmission and pump beam optimization

Beyond increasing the escape efficiency, it is important to obtain a high transmission from the cavity output toward the quantum memory. The transmission in the signal arm could be increased by removing the glass plates and using a reduced reflection signal obtained by a reflection from the LPF[1] for the lock. In addition the bandpass filter BP1[2] and the Etalon[3] were exchanged with higher transmissive ones. In addition with a fiber coupling efficiency of 80 % a total transmission of 70 % could be obtained from the cavity toward the detector. By connecting the source with the solid state memory via two fibers, using an index matching gel[4], a total transmission toward the quantum memory of 50 % could be achieved.

[1] longpass filter with cutoff at 532 nm
[2] Semrock FF01-600/14
[3] SLS Optics Ldt. FSR 100.4 GHz, Finesse 23.5
[4] Thorlabs: Index Matching Gel

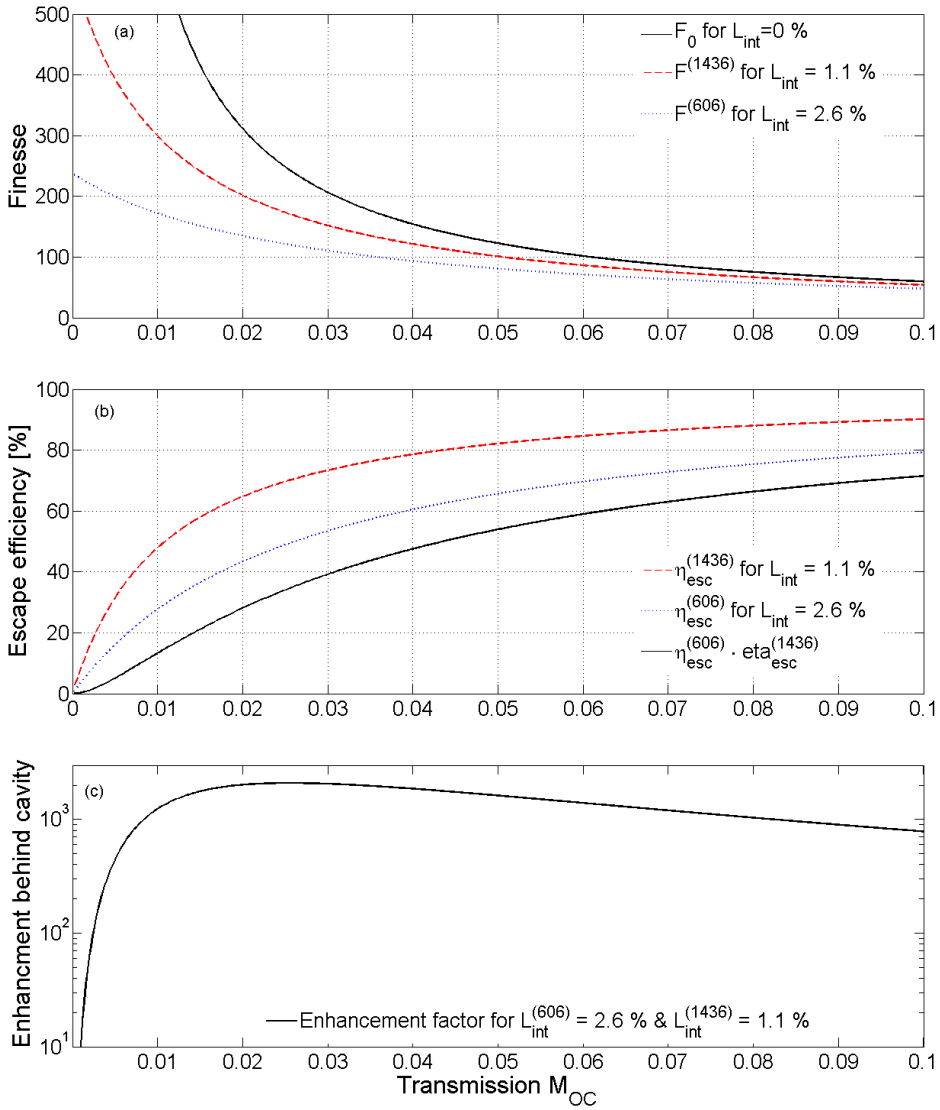

Figure 5.2: (a) Finesse and (b) escape efficiency as function of transmission of out-coupling mirror for a cavity without internal loss (black), a loss of 1.1 % for the idler photons (red) and a loss of 2.6 % for the signal photons. (c) Enhancement factor of the spectral brightness at the cavity output with respect to the single pass case. $B = \eta_{esc}^{(606)} \eta_{esc}^{(1436)} \frac{F^{(606)} F^{(1436)} \sqrt{F^{(606)} F^{(1436)}}}{2F_0}$

In addition the beam waist of the pump beam was recalculated and optimized by replacing the in coupling lens with 400 mm focal length before the cavity with a lens with 100 mm focal length.

5.2.3 New low noise telecom single photon detector

Apart from increasing the escape efficiency and the transmission behind the cavity, clicks at the heralding detector should only occur if a photon is created by the SPDC process and correlated to a signal photon. Hence high dark-count rates and uncorrelated noise should be avoided. To reduce the dark counts the previous detector[1] has been replaced by a low noise telecom single photon detector[2] with only 10 Hz dark count rate at a detection efficiency of 10 %. The counter is also based on an InGaAs avalanched photo diode (APD). It is reverse biased above the breakdown voltage. If a photon pings on the p-n junction a carrier is generated and undergoes an avalanche gain resulting in an increasing voltage. To harness this effect the avalanche must be stopped and the device reset by a quenching circuit. To reduce thermal effects and achieve a low dark count rate the APD is cooled down to a temperature of −90 °C.

5.2.4 Effect of uncorrelated noise

After reducing the dark counts we observed a big contribution of uncorrelated photons shown in Fig. 5.3 (a). To obtain the spectrum plotted in Fig. 5.3 we used a the filter cavity as scanning Fabry-Perot interferometer in the idler arm as we did previously in the signal arm (see. Fig. 3.18). To this end a voltage ramp created by an arbitrary waveform generator[3] and synchronized with the opening time of the chopper wheel (running with 30 Hz), was applied on a piezo behind one mirror of the filter cavity. Fig. 5.3 shows different histograms with the trigger the voltage ramp as start signal and a click on the idler detector as stop signal.

All histograms show a region of low noise, while the signal was blocked by the closed chopper which is placed in front of the fiber leading to the single

[1] IdQuantique: id220
[2] IdQuantique: id230
[3] Tecktronix

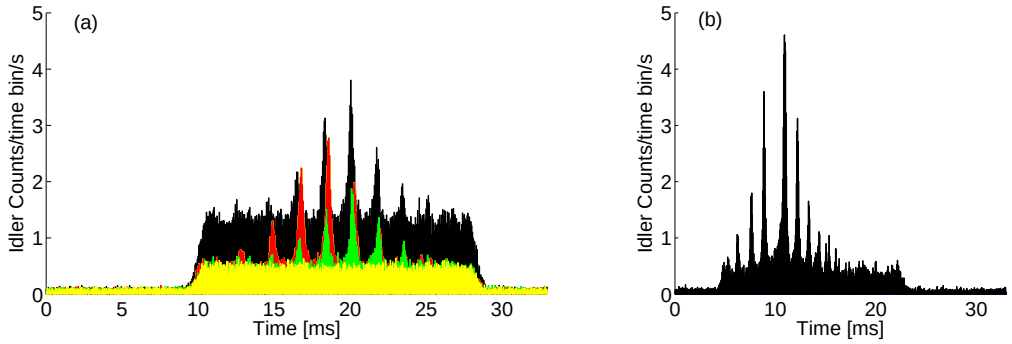

(a) black without filter, color polarization analysis

(b) with bandpass filter

Figure 5.3: Spectra taken with scanning filter cavities, the low noise level is related to dark counts, when the copper is closed, high noise level shows uncorrelated noise. (a) polarization analysis of noise, black spectra is taken without polarizing beam splitter and shows a high noise floor. Red spectra is taken with polarizer set to horizontal polarization. Green spectra is taken with polarizer set to 45°. Yellow spectra is taken with vertical polarization. (b) Bandpass filter decreases noise to a SNR of level to 1/10.

photon counter. There the noise is dominated by detector dark counts. While the chopper is opened for 18 ms, the noise level is increased in all histograms. The noise has to be broadband, since it is transmitted by the filter cavity and reduced by the bandpass filter[1] (center wavelength: 1440 nm, bandwidth: 14 nm). This broad band noise may be due to fluorescence created by the pump beam in the PPLN crystal or in other optical elements. On top of the noise the main cluster with the cavity modes separated by 423 MHz is visible.

In Fig. 5.3(a) a histogram without spectral filter is shown in black. We see a strong background covering 1/3 of the signal. For the colored histograms a half-waveplate in combination with a polarizing beamsplitter was in front of the fiber input. Each color corresponds to a different waveplate setting showing that the signal is well polarized and the noise is unpolarized. For maximal transmission of the signal the noise level is 1/6 of the signal. In Fig. 5.3(b) a bandpass filter[2] (center wavelength: 1440 nm FWHM: 14 nm) is used resulting in a good

[1] Omega optics: 1440BP14/25
[2] Omega optics: 1440BP14/25

background suppression resulting in a signal-to-noise ratio of 10.

5.3 Improved results

5.3.1 New histograms

The applied changes led to major improvements for the outcome of the photon pair source. In Fig. 5.4 typical histograms of start- (click on the idler detector) stop- (click on the signal detector) measurements of the new source are shown. The detection events of each single photon counter are recorded with a time stamp card[1]. A self-written Matlab code is used to plot the histograms and to calculate parameters shown in the inset. Fig. (a) shows a measurement using the filter cavity selecting a single mode in the idler arm and an Etalon filtering side clusters in the signal arm. Fig. (b) shows a measurement just with the Etalon in the signal arm, bypassing the single mode filter in the idler arm. Thus all modes of one prominent cluster are detected.

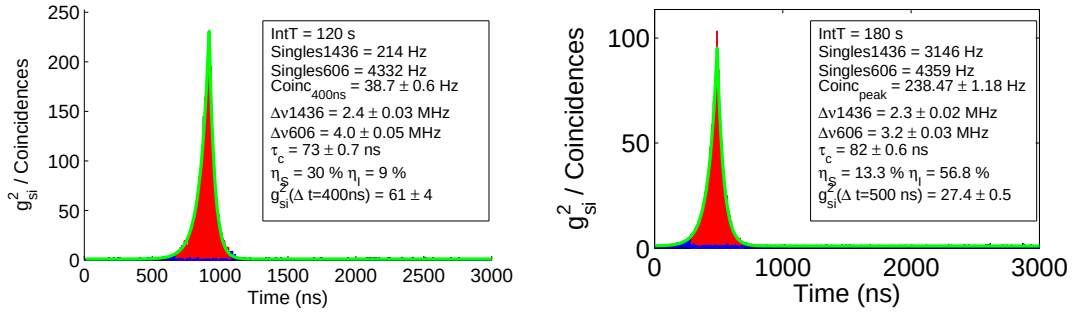

(a) single mode (b) multi mode

Figure 5.4: Histograms of a single mode measurement and a multi mode measurement with corresponding data in inset: detected single rates, coincidences in red window, photon linewidth archived by exponential fit (in green), correlation time of FWHM, heralding efficiencies for signal and idler photons and $g^{(2)}_{si}$-value obtained by the ratio in between the coincidence area and a noise area normalized to the same width.

[1] Signadyne

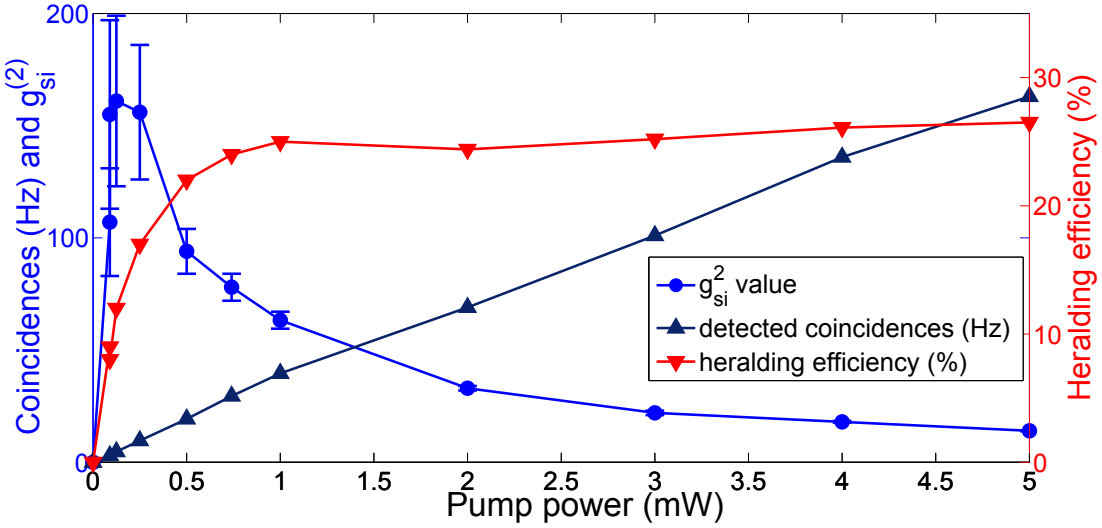

Figure 5.5: detected coincidences, $g_{si}^{(2)}(\Delta t = 400\,\mathrm{ns})$ and heralding efficiency as function of the pump power.

With these changes we reach in the filtered case heralding efficiencies up to 30 % at the signal photon detector, which leads to heralding efficiency of 22 % in front of the memory crystal, which is more than 3 times higher than in previous experiments [73]. Coincidence rates are improved by one order of magnitude for a single mode with respect to [58], which is necessary to obtain reasonable integration times for the storage experiments. The non-classical $g_{si}^{(2)}$-value is increased by more than one order of magnitude due to better suppression of non-correlated noise. Thus the pump power could be increased up to the maximal available pump power of up to 5 mW, keeping a good non-classical value, while increasing the count rate. In Fig. 5.5 (a) the coincidences and heralding efficiency as function of the pump power are plotted. We achieve a detected coincidence rate of $34\,\mathrm{Hz\,mW^{-1}}$. The heralding efficiency at powers below 1 mW is limited by dark counts of the telecom detector. The slope for the coincidences rates results in a detected brightness of $34\,\mathrm{Hz\,mW^{-1}}$. If we correct for detection efficiencies (10 % for telecom photon and 62 % for signal photon) and transmission losses, we achieve a spectral brightness of 820 coinc/mW/MHz/s at the output of the cavity. Taking also the chopper and the escape efficiencies into account and comparing that value with the obtained single pass rate in chapter 3 an enhancement factor

of 1400 is obtained.

The heralding efficiency is constant at 28 %, for value of pump power $P_p > 1\,\mathrm{mW}$. For $P_p < 1\,\mathrm{mW}$, it is limited by the detector dark-counts.

5.3.2 Size of integration window

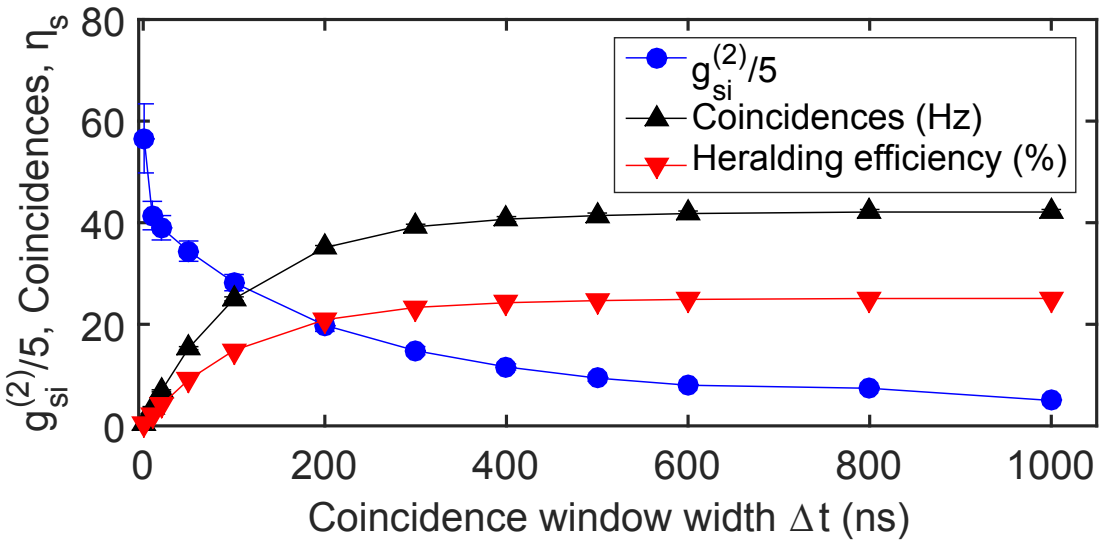

Figure 5.6: $g^{(2)}_{si}$ value, coincidences and heralding efficiency for different width of the coincidence window.

The size of the integration window in which the coincidences are counted is selected to cover most of the coincidence peak.In Fig. 5.6 the obtained values for $g^{(2)}_{si}$, coincidences and heralding efficiency are plotted for different sizes of the evaluation window. For narrow windows the obtained $g^{(2)}_{si}$ values are higher but less counts are included in the integration area, leading to a underestimation of the coincidence rate.

For the values reported in the following sections and publications we agreed on a size for the coincidence window of 400 ns, for broader windows the coincidence rate saturates and would reveal lower $g^{(2)}_{si}$ values. Note that in most broadband sources the temporal shape cannot be resolved with given detector resolutions. For those sources or for the single pass case the coincidence window is given by the detector temporal resolution.

5.4 Temporal and spectral characterization

As a result of changing the output coupling, the finesse of the resonator was reduced to 184 for idler and 114 for signal, and the bandwidth of the photons became slightly larger than in [58]. To investigate the new bandwidth of the photons we use the second order cross-correlation function $G^{(2)}_{s,i}$. Its temporal shape is a result of the cross-correlation of the temporal shapes of both photons. The spectrum of each photon should resemble the Lorentzian shape of the cavity mode spectrum corresponding to an exponential time structure. Hence we see in Fig. 5.4 the rising exponential of the idler and the falling exponential of the signal wave packet. We fit the histogram with the following function:

$$\begin{aligned} G \propto & \exp\left[-2\pi \cdot \Delta\nu_s \cdot t\right] \cdot \Theta\left(t\right) \\ & + \exp\left[2\pi \cdot \Delta\nu_i \cdot t\right] \cdot \Theta\left(-t\right) + c_0 \end{aligned} \tag{5.3}$$

which directly results in the cavity bandwidth for signal and idler wavelength $\Delta\nu_{s,i}$, which is typically 3.7 MHz and 2.3 MHz. We use the heaviside function $\Theta\left(t - t_0\right)$ to distinguish between the idler ($t < t_0$) and signal ($t > t_0$). The smaller value for the idler photons can be explained by a higher cavity finesse due to slightly lower intra-cavity losses. We define the correlation time τ_c of the photon pair as the width (FWHM) of the measured $G^{(2)}_{s,i}$-function ($\tau_c = 78$ ns). The biphoton bandwidth is then $\Delta\nu = \frac{\ln 2}{\pi\tau_c} = 2.8\,\mathrm{MHz}$.

5.5 Heralded narrow-band single-photon source

For the following correlation measurements additional single photon counters were required. A simplifed sketch of the setup is shown in Fig. 5.7.

We next check the single photon character of the generated light. This is done by measuring the autocorrelation conditioned on the detection of a heralding photon. We use a gate window of 400 ns around the detection time of the idler photons (analog to previous measurements) to herald the signal photons. We then use a method introduced by Fasel et al. [101] to generate histograms as shown in Fig. 5.8. The histogram illustrates the triple coincidences sorted by the number of heralding events between succeeding detections at different signal

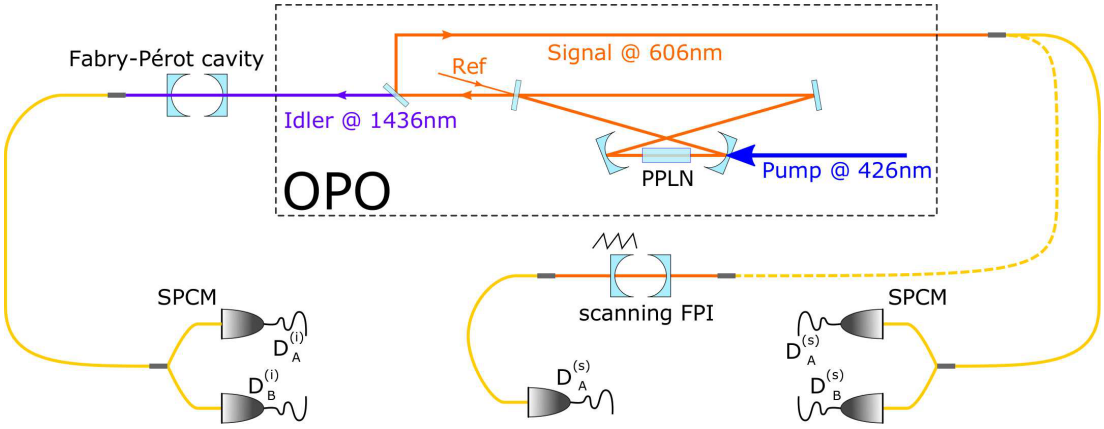

Figure 5.7: Schematic of the experimental setup. Additional photon counters were used for correlation measurements. A replica of the filter cavity was used in the signal arm for spectral measurement of the signal modes. The fiber connections and beam splitters can be changed according to the current experiment.

detectors. The ratio of events in the central bin (bin 0, coincidence of the signal detectors in the same heralding window) divided by the mean value of the outer bins corresponds to the conditioned autocorrelation $g^{(2)}_{i:s,s} = 0.035(2)$. This value is considerably below the classical threshold $g^{(2)}_{i:s,s} \geq 1$.

We performed such measurements of the conditioned autocorrelation for various pump powers. The results are shown in Fig. 5.9. For all accessible pump powers the $g^{(2)}_{i:s,s}$-value is well below the classical threshold, with a minimum of 0.010(4). Our source is therefore well suited to generate narrowband heralded single photons with high fidelity. The solid line in Fig. 5.9 is a fit to the data according to the model in [94] and describes our experimental data well. The approximately linear dependence of the $g^{(2)}_{i:s,s}$-values on pump power was also observed earlier [101]. The inflection of the curve and decrease at very low pump powers has the same origin as for the cross correlation. For low pump powers the rate of detected photons becomes comparable to the dark count rate. The single photon correlation is then superimposed by noise coincidences.

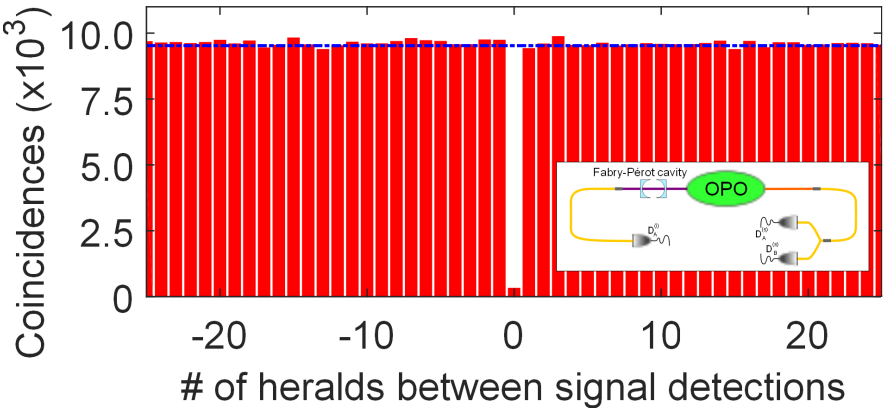

Figure 5.8: Heralded signal autocorrelation histogram for a pump power of 1 mW. The dashed line illustrates the average height of the outer bins, corresponding to $g^{(2)}_{i:s,s} = 1$. For the bin at 0, where triple coincidences are recorded, the height corresponds to $g^{(2)}_{i:s,s} = 0.035$.

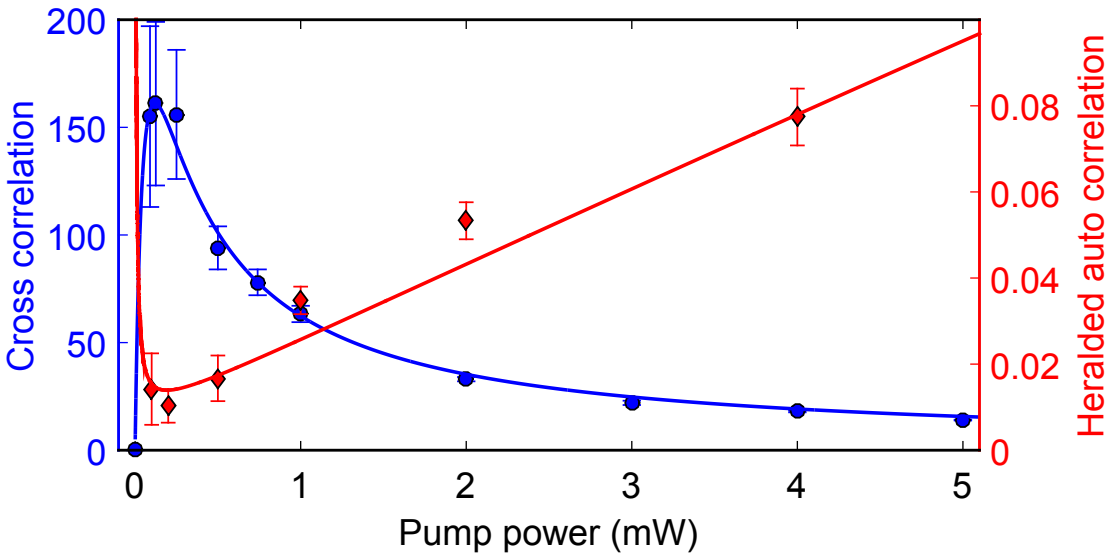

Figure 5.9: Blue circles with error bars show the $g^{(2)}_{si}$ value, the solid line represents fit to theoretical model. Red diamonds show conditioned autocorrelation values of the signal photons. Solid lines represent fits according to a theoretical model.

5.6 Measurements of unconditional auto-correlation

The signal-idler second-order cross correlation is a quantity easy to measure, but it does not prove the quantumness of the generated light without further assumptions. Hence we performed additional measurements to unambiguously show the quantum character of the correlations. First we measured the unconditional second order autocorrelation functions for signal ($g^{(2)}_{s,s}$) and idler ($g^{(2)}_{i,i}$), shown in Fig. 5.10. To this end we split the particular photons in a 50/50 fiber beam splitter followed by single photon detectors at both outputs. Again we correlate the detection events in the post processing of the time tags, using the data from both the signal detectors only. For an ideal two-mode squeezed state we expect values of $g^{(2)}_{x,x}(0) = 2$, which is not the case for our results. For comparison with other measurements we further define the $g^{(2)}_{x,x}$-values via integration over a 400 ns interval, analog to the cross correlation value. This eventually results in $g^{(2)}_{s,s}(\Delta\tau = 400\text{ns}) = 1.10(1)$ and $g^{(2)}_{i,i}(\Delta\tau = 400\text{ns}) = 1.33(4)$. Due to the use of a low dark count detector this is the first time we observe a bunching peak for the idler photon autocorrelation (see [73] for a comparison). From the fits to the histograms we determine the width of the peaks as 138 ns and 182 ns (FWHM; signal and idler, respectively), which is twice the time constant as for the cross correlation, as expected. From the height of the peaks we deduce values of $g^{(2)}_{s,s}(0) = 1.18(4)$ for the signal and $g^{(2)}_{i,i}(0) = 1.5(1)$ for the idler photons. Two reasons can explain the decrease of the measured correlation values: A superposition of modes and noise in the detection process. It has been shown [81, 102] that a superposition of modes results in a reduced value following $g^{(2)}_{x,x}(0) = 1 + \frac{1}{N}$, where N is the number of contributing modes. In the signal branch there is no narrowband filtering installed, which results in the contribution of all modes of the central cluster By determining the total intensity as the sum of detected counts in all modes and comparing it to the detections in the central mode, we infer a number of $N = 3.9$ effective modes (assuming all modes have the same intensity). This corresponds to $\tilde{g}^{(2)}_{s,s}(0) = 1.26$, close to the measured value.

The autocorrelation measurements, especially for idler, are also affected by detector noise, described in chapter 2 in Eq. 2.15, reducing the resulting value compared to the ideal case. We measured dark count rates of $B^{(s)}_A = 30$ Hz

and $B_B^{(s)} = 50$ Hz for the signal measurement as well as $B_A^{(i)} = 37$ Hz and $B_B^{(i)} = 384$ Hz for the idler measurements. Taking only these detector dark counts into account we find upper limits of $g_{s,s}^{(2)}(0) \leq 1.91$ and $g_{i,i}^{(2)}(0) \leq 1.26$. Combining the assumptions of many modes and dark counts for the signal photons we obtain a theoretical value of 1.20, which is in good agreement with our measurement.

With this data we can also give an estimation for the conditioned autocorrelation. We expect the relation $g_{i:s,s}^{(2)} = \frac{g_{s,s}^{(2)} \cdot g_{i,i}^{(2)}}{g_{s,i}^{(2)}}$ [82]. Since we condition the detection of the signal photons to the idler however, we project the signal photons to a single mode, too. Thus we assume for the autocorrelation value of the signal photons the theoretical value for a single-mode, corrected for dark counts, and retrieve a prediction of $g_{i:s,s}^{(2)} = \frac{1.91 \cdot 1.33}{69.5} = 0.037$. This fits well the measured value. However, the $g_{i,i}^{(2)}$-value here was measured with a low and a high dark count detector, while for the conditioned autocorrelation only the low dark count detector was used for heralding. Hence this value is underestimation the quality of the photons.

We can further use the measured data to prove the quantum character of the correlations. The Cauchy-Schwarz inequality $R = \frac{\left(g_{s,i}^{(2)}\right)^2}{g_{s,s}^{(2)} \cdot g_{i,i}^{(2)}} \leq 1$ is bound for classical correlations. When we insert the results for cross-correlation ($g_{s,i}^{(2)} = 70(1)$) and auto-correlation measurements we find $R = 2711 \pm 247$. Hence we violate the classical boundary by more than 10 error margins which is a proof of non-classical correlations.

We summarize the different correlation results, and values derived by different methods in table 5.2 for comparison.

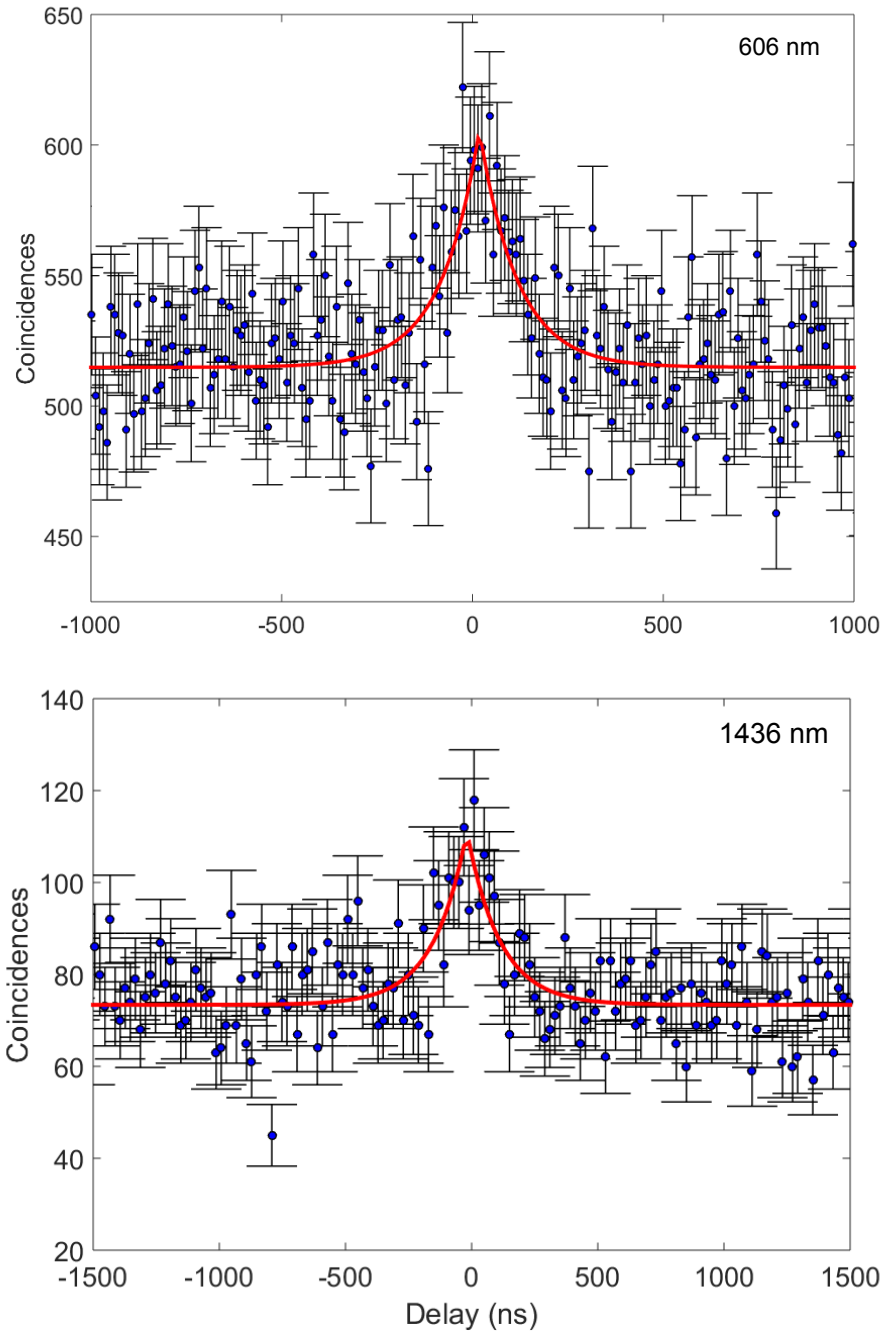

Figure 5.10: Unconditioned autocorrelations functions for signal (top, pump power 1 mW) and idler (bottom, pump power 4.3 mW) photons. The solid lines are fits of symmetric exponential functions used to calculate the peak value for zero delay.

	$\Delta\tau = 0$	$\Delta\tau = 400$	theoretical prediction	classical threshold
$g^{(2)}_{i,s}$	335(8)	70(1)		$\leq \sqrt{g^{(2)}_{ss} g^{(2)}_{ii}}$
$g^{(2)}_{s,s}$	1.18(2)	1.10(1)	≤ 1.2	
$g^{(2)}_{i,i}$	1.5(1)	1.33(4)	≤ 1.26	
R	$63(6) \cdot 10^3$	2700(250)		≤ 1
$g^{(2)}_{i:s,s}$		0.035(2)	≤ 0.037	≥ 1

Table 5.2: Second order cross- and auto-correlation and non-classical values R at zero time delay, for an integration window of 400 ns, the theoretical prediction including assumptions for detector dark counts, and the classical boundaries. The pump power is 1 mW for the measurement of all correlation functions, except for $g^{(2)}_{i,i}$ where it is 4.3 mW.

5.7 Quantum light storage in the spin state

With the improved performance of the source it is promising to store the single photons in the spin state of Pr^{3+}:Y_2SiO_5. Therefore the photons are first stored in the excited state and create a collective single excitation of the Praseodymium ions, as described in chapter 4. Now we use an optical transfer pulse to transfer the excitation into a long lived spin state, offered by the level structure of Praseodymium. Here the rephasing process is frozen. After a time T_s a read pulse transfers the photons back into the excited state and the rephasing continues creating an echo after a time $T_{storage} = \tau + T_s$. This technique allows an extension of the storage time and in addition on demand readout of the quantum memory. This experiment is much more demanding on the source and on the quantum memory. The write and read pulses create noise due to fluorescence, which has to be suppressed strongly. In addition the condition for quantum storage is that $\eta_H > \mu_1$, where μ_1 is the minimum input number of photons to achieve a signal-to-noise ratio of 1 after the memory [104, 105]. In state of the art demonstrations of solid-state spin-wave quantum memories with weak-coherent states, μ_1 ranges between 0.03 and 0.11 [38, 104, 105], albeit with much longer pulses, from a few microseconds to a few hundred ns, respectively. Our source is therefore promising for the spin-wave storage of single photons in solid-state quantum memories.

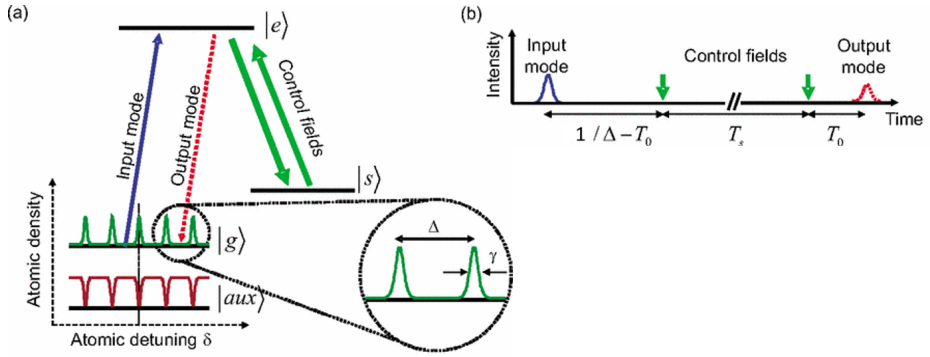

Figure 5.11: Scheme of the AFC protocol [103]. a) An input photon (blue arrow) is absorbed by the comb (green peaks). Two transfer pulses (green arrows) respectively map the collective atomic excitation to the spin state and, after a time T_s, bring it back to the excited state. After a time $\tau + T_s$ (where $\tau = 1/\Delta$ is the predetermined AFC storage time), the atoms decay and the photon is re-emitted (red arrow). b) Timing of the AFC scheme

To show the storage and retrieval of non-classical light the signal-to-noise ratio has to be higher than two $g_{si}^{(2)} > 2$, assuming signal and idler fields have thermal statistics, as described in chapter 2. Thus it is important to keep non-correlated noise low. To transfer the excitation to the spin state we use strong ($P \approx 20\,\mathrm{mW}$) control pulses which create a high noise level. To suppress most of this noise several filtering techniques are used, involving spatial, spectral and temporal filtering. The transfer pulses enter the crystal with an narrow angle ($\approx 2°$) with respect to the single photon mode. A narrowband filter has been developed by Mustafa Gündoğan [104]. He introduced a second Pr^{3+}-crystal and created a narrow transmissive window ($\nu = 4\,\mathrm{MHz}$) inside the inhomogeneous broadening using hole burning techniques. Using this filter the non-resonant noise could be decreased by a factor of 700. This allowed him to show that weak coherent pulses required a photon number higher than $\mu_1 = 0.07$ to reach a signal to noise ratio exceeding one, $SNR > 1$ [104]. The transfer pulses are triggered by a click of the heralding detector. In that case the pump of the source is switched off, such that no additional noise from the source enters the crystal. Further more the storage efficiency has been increased by Alessandro Seri, another PhD student. He exchanged the crystal by a longer one in order to increase the OD. In

addition he studied different methods of optical pumping to improve the quality of AFC leading to an increase in the efficiency, shown in Fig. 4.8. The storage in the excited state was increased to 17 % for a storage time of 5 µs. The storage efficiency in the excited state is now limited by the bandwidth of the photons. Since the photons got slightly broader in frequency their Lorentzian shape with FWHM of 2.8 MHz doesn't overlap completely with the AFC (squared shape of 4 MHz width). However, the photon linewidth could be decreased by extending the cavity length to increase the storage efficiency.

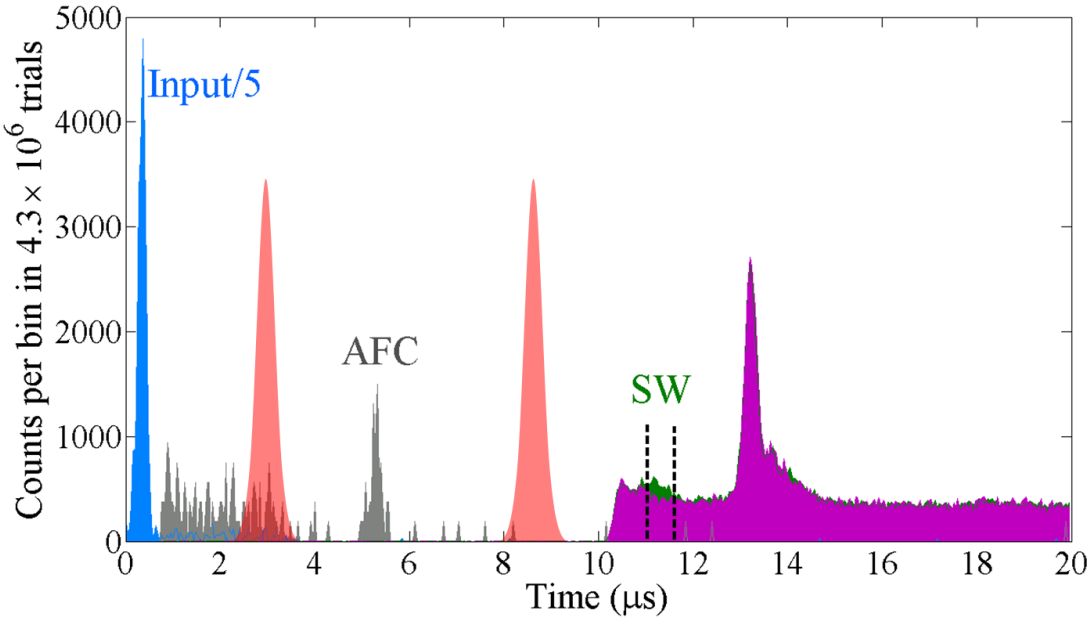

Figure 5.12: Time histogram of spin state storage with heralded single photons. The input photons transmitted through the spectral pit without any AFC are shown in blue. The counts in gray show the result with applied AFC. A photon echo is created after 5 µs. The green counts are obtained, when the transfer pulses, marked in red are applied. In that case the counters are in the gated mode and opened after the transfer pulses happened. In magenta a noise measurement without input photons is shown. The dominant peak at 13.5 µs is created by an echo of the readout pulses. Before at a total storage time of 11 µs we see the retrieved photons in green above the noise level.

With the new characteristics of the source and the memory we were confident to try the spin state storage with heralded single photons created by the described

source. We obtained first preliminary results by connecting the source with the memory. An AFC with a preliminary storage time of 5 µs was created. Write pulses were applied 2 µs after a click on the heralding detector, 6 µs later a read pulse was applied. The total storage time is thus 11 µs. In Fig. 5.12 results of a storage experiment are shown.

A signal to noise ratio of 1.36(2) is obtained in this measurement. Taking into account the autocorrelation values, measured in section 5.6, we could violate already the classical boundary of the Cauchy-Schwarz inequality $g^{(2)}_{si} \leq \sqrt{g^{(2)}_{ss} g^{(2)}_{ii}} = 1.21(4)$ for an integration window of 400 ns. However, the signal spectrum behind the source contains several modes which results in a lower value of $g^{(2)}_{ss}$, while the memory acts as filter for a single mode. On the other hand, the main noise contribution is created by the coherent control pulses. The autocorrelation behind the memory could not be measured because the low count rate would lead to a very long integration time. The obtained storage efficiency is 1.3 %. However, a signal to noise ratio higher than 2 is desirable for a clear evidence of non classical light. Recent results obtained by A. Seri and A. Lenhard after further improvement on the memory (reduction of the noise) led to higher signal to noise values of 5.4(9) at a storage time of 13.25 µs.

5.8 Conclusion

In summary, we developed a source of telecom-heralded single photons with high heralding efficiency and a high creation rate of narrowband photons compatible with a solid-state quantum memory based on Pr^{3+}:Y_2SiO_5. We proved the single photon character of the emission by direct measurement of the heralded autocorrelation function, with antibunching parameters as low as 0.01. In addition, we reported significant improvements in terms of count rate, quality of correlations and heralding efficiency (up to 28 %), compared to the state of the art. This source is well suited for advanced experiments with solid state quantum memories. In particular, it meets the requirements to demonstrate single-photon spin-wave storage in a solid-state quantum memory, which would be an important milestone for the use of solid-state quantum memories in quantum networks and quantum repeaters architectures.

6

Frequency entanglement of narrow band photon pairs

6.1 Introduction

In the previous measurements we showed non-classical light correlations of the created photon pairs and by using one photon as herald, a single photon Fock state could be created. These quantum correlations are sufficient for some repeater architecture [13]. Some other architectures require direct light matter entanglement [106].

Photons can be entangled in different degrees of freedom, including pathway, polarization, time, frequency or momentum. The most common types of entanglement are polarization and time-bin entanglement. I will briefly comment on the challenges of implementing these types in our source. Then I will show the possibility of implementing entanglement based on frequency-bins created naturally by our source. High visibility two photon interference fringes are shown, which are a clear indicator for entanglement. Finally, I will show how a Bell inequality can be violated with our non-maximally high dimensional entangled state, and show first results towards this goal.

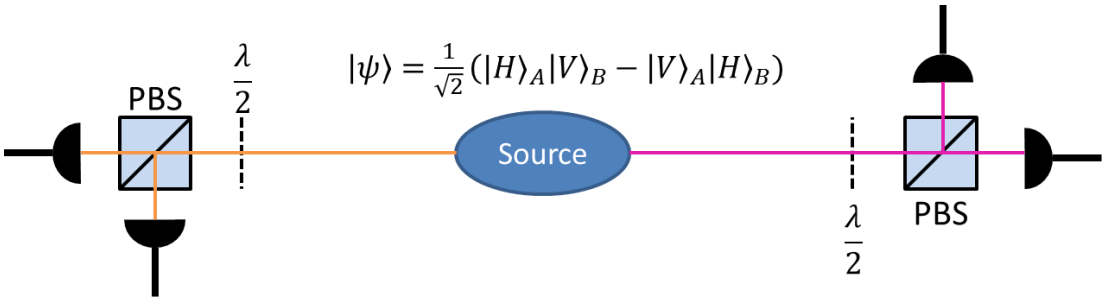

Figure 6.1: Source generates polarization entangled photon pairs, $\frac{\lambda}{2}$-waveplates and polarizing beamsplitters (PBS) can be used to analyze the entangled state.

6.1.1 Polarization entanglement

Polarization entanglement is rather simple to analyze and therefore used in many experiments [107, 108]. The polarization analysis can be done with a half-waveplate and a polarizing beam splitter (PBS) in each output arm of the photon pair source (see Fig. 6.1). By rotating the half-waveplate the measurement bases can be selected. The PBS acts then as analyzer with two possible outcomes.

Methods to generate polarization entangled pairs are:

- using type II parametric down-conversion [60]
- using two orthogonally polarized Type I sources and overlap their output beams[42]
- using a two crystal configuration respectively rotated by 90° [55, 109].

In our setup we implemented a configuration with two Type I crystals inside the cavity respectively rotated by 90°, similar to [55]. Both crystals generated photons pairs at 606 nm and 1436 nm with orthogonal polarizations. Due to dispersion and birefringence inside the crystals photons with each combination of the four possible combinations can obtain different phase. This phase is very sensitive to the temperature of the crystals (in the mK range). To exit the cavity with the same efficiency all the photons require the same phase, that means the cavity has to be resonant to all the four created modes. In principle a phase compensation inside the cavity can be obtained with additional birefringent materials as in [109] and if the two crystals had identical properties the phase

should be compensated by their birefringence themselves. In practice it resulted that the crystals have slightly different phase matching temperatures and that the phase sensitivity of the temperature is hardly covered by the stability of the temperature controllers ($\Delta T \approx 8\,\mathrm{mK}$). Nevertheless, I achieved to keep three modes resonant by inserting a birefringent wave-plate for phase compensation, but one degree of freedom was missing to keep all four modes resonant.

6.1.2 Energy-time entanglement

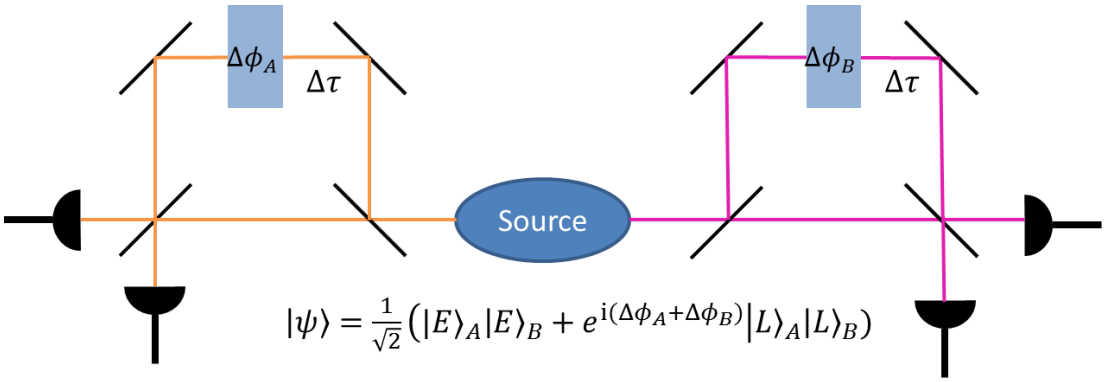

Figure 6.2: Source generates early and late time bins. An interferometer in each arm is used to analyze the entanglement, unitary transformations can be performed by changing the phase setting $\Delta\phi$ in the interferometer arms.

Energy time entanglement is achieved naturally in the SPDC process, as soon as the coherence time of the pump is much longer than the coherence time of the photons. Contrary to polarization entanglement it doesn't require special crystal configurations or phase compensations and is easier to obtain. Energy-time entanglement, or its discrete version time-bin entanglement, is convenient to use in experiments with long fiber length, like in [110], since the stability of polarization in fibers relies on stable outer conditions of the fiber like temperature changes or mechanical stress, which is harder to avoid over long distances. For the energy-time and time-bin entanglement analysis, Franson-type interferometers [111] can be used. These interferometers consist of a short arm and a long arm in which the phase difference between the arms can be tuned. In addition the arm-length difference of the interferometers has to be longer than the coherence length of the

photons and shorter than the coherence length of the laser $\tau_p > \frac{l_{int}}{c} > \tau_{ph}$. That leads to a constraint for very narrowband photons which would require interferometers with a long arm length difference and elaborate stabilization techniques. Possible interferometers are developed in our group, but a more elegant and convenient way for our source could be the manipulation in the frequency domain. Polarization entanglement is limited to two dimensions, since polarizing beam splitters have just two outputs. The time and frequency domain, offers the possibility of higher dimensional entanglement, because the state can be analyzed with more than two outputs. An example for an interferometer with three arm is given in [112].

6.1.3 Frequency-bin entanglement

Instead of using the time domain for the entanglement analysis, we can manipulate and measure it also in the frequency domain, since photons crerated by SPDC are intrinsically time-energy entangled. In our case, the source creates several narrowband frequency modes, which can be assumed as discrete frequency-bins, leading to frequency-bin entanglement.

By replacing the interferometers or polarizing beamsplitters with spectral filters and phase shifters or waveplates with optical devices which can perform an unitary transformation in the frequency domain, one can analyze the frequency entangled state in different bases. For narrowband photon pair sources as obtained by cavity enhanced SPDC this could be more convenient than the analysis of time-bin entanglement, because of the long coherence length of the photons. In addition it is practical for existing quantum communication structures and can be combined with frequency multiplexing [24]. So far, few experiments showed frequency-bin entanglement, mostly with broadband sources [74, 113]. To our knowledge there is no frequency bin entanglement shown with narrowband sources based on cavity enhanced SPDC. This kind of source intrinsically creates narrowband frequency-bins, since the cavity emits few modes which are well separated and can be distinguished by frequency filters. In that case each created mode represents a dimension of our entangled state, thus we have intrinsically a higher dimensional entangled state.

In the following sections I will describe the spectral properties of our source and the implementations which are used to analyze the two photon state. A theoretical model adapted to our spectrum is presented. High visibility two-photon interference fringes are shown, and an experimental investigation towards the violation of a Bell inequality with our non-maximally entangled high dimensional state is presented.

6.2 State created by cavity enhanced photon pair source

As already presented in chapter 5, the spectrum of our source is composed of clusters containing several frequency modes with different height. These modes naturally define our frequency bins and are sketched in Fig. 6.3. The source is pumped with a narrow-band pump laser in continuous wave and energy has to be conserved:

$$h\nu_p = h\nu_s + h\nu_i \tag{6.1}$$

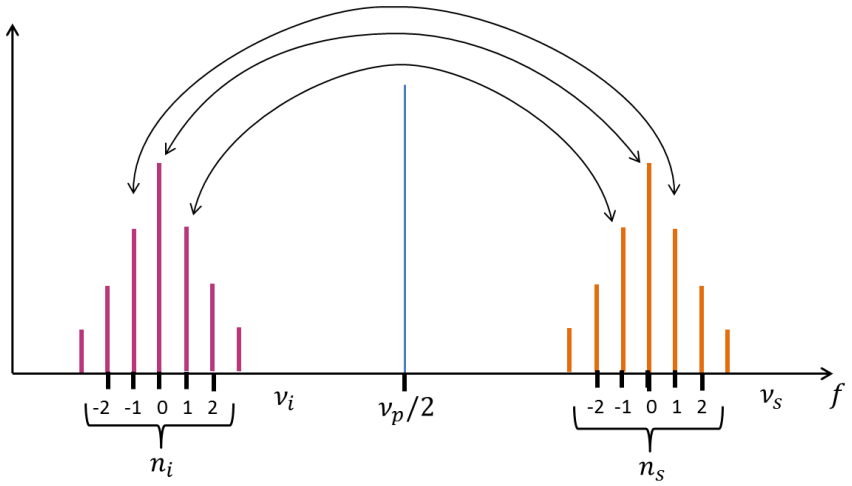

Figure 6.3: Sketch of correlated signal and idler modes generated by the photon pair source. Since the pump laser has a narrow line width and energy has to be conserved, each idler mode has a correlated signal mode. By filtering a frequency-bin of one photon, we can determine the frequency of it's partner.

As a result each spectral mode of the signal photon is correlated with a certain mode of the idler photon. The frequency correlations lead naturally to the creation of a frequency entangled state:

$$|\psi\rangle = \sum_n g_n |n\rangle |-n\rangle \tag{6.2}$$

Where $|n\rangle$ describes frequency bin n, with the central frequency bin denoted to $n = 0$, and g_n describes the different intensity of each bin. In our case, since the various frequency bins have different intensities, we create a non maximally entangled state.

Fabry-perot cavities used as frequency filters (FCs) before the single photon detectors allow us to select a given bin to be measured.

6.2.1 State analysis

To be able to manipulate the central bin, we use a method introduced by Olislager et al. [74]. Electro Optical Modulators (EOM) are used in each arm and create a superposition between a central mode and its neighboring modes. The principle of EOMs can be described as follows:

EOMs use a non-linear crystal on which an oscillating electrical field is applied with a radio frequency Ω of amplitude c and phase δ. That leads to a fast change of the refractive index and thus creates sidebands (see Fig. 6.4) in the frequency domain. This action can be described by the unitary transformation on the monochromatic frequency state $|n\rangle$:

$$\mathsf{U}(c,\delta)\,|n\rangle = \sum_m U_m(c,\delta)\,|n + m\Omega\rangle\,, \tag{6.3}$$

where $U_m(c,\delta) = J_m(c)e^{im(\delta-\frac{\pi}{2})}$. And $J_m(c)$ are the Bessel functions.

The oscillation frequency Ω of the electrical field is set such, that the created sidebands overlap with the frequency modes emitted by the cavity ($\Omega = FSR$). In the following we use the modulation indices $a = \pi c_A/V_\pi$ with the voltage amplitude c_A and the phase setting α for Alice's (idler) EOM and $b = \pi c_B/V_\pi$ with the voltage amplitude c_B and the phase setting β for Bob's (signal) EOM.

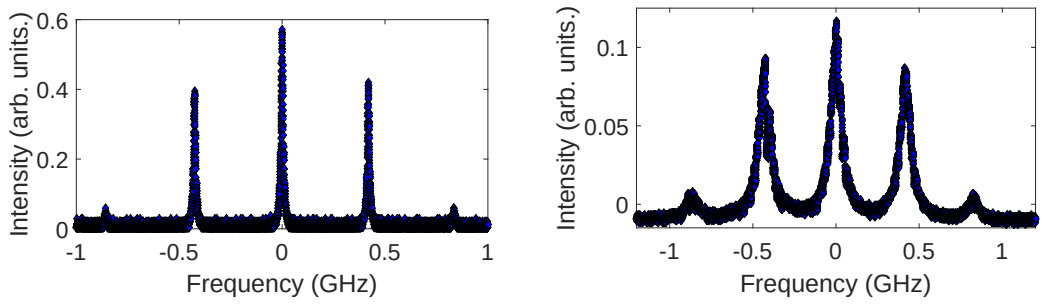

(a) signal sidebands

(b) idler sidebands

Figure 6.4: Recorded sidebands generated by the EOMs using classical reference beams at signal- and idler-wavelength passing through the EOMs and through the scanning filter cavities before being detected with fast photodiodes. From the ratio of the peak height we infer a modulation index $a = 1.30$ for signal and $b = 1.36$ for idler. The different peak width results from different finesse of the filter cavities.

When the electrical field is applied to the EOMs all modes are superposed with their individual neighbors, i.e. the unitary operator has to be applied to all modes $|n\rangle$. As both photons of the pair are transmitted through different modulators the unitary has further to be applied to signal and idler modes individually. This results in the following pair state:

$$\left|\tilde{\Psi}\right\rangle = \hat{U}_A \otimes \hat{U}_B \left|\Psi\right\rangle = \sum_n \sum_k \sum_m U_k\left(a,\alpha\right) U_m\left(b,\beta\right) g_n \left|n+k\right\rangle \left|-n+m\right\rangle \quad (6.4)$$

$$U_k\left(a,\alpha\right) U_m\left(b,\beta\right) = J_k\left(a\right) J_k\left(b\right) \exp\left[i\left(k\alpha + m\beta - \pi/2\left(k+m\right)\right)\right] \quad (6.5)$$

This is similar to the model shown in Olislager et al [74], but it has been adapted by A. Lenhard to take into account the fact that we have a finite spectrum with varying amplitude for each mode.

A simulation together with a spectral measurement of the idler modes is shown in Fig. 6.5. By changing the phases α or β of the electrical field (RF-signal) which drives the EOM, a transformation on the two photon state can be applied, leading to constructive or destructive interferences in the coincidence measurements.

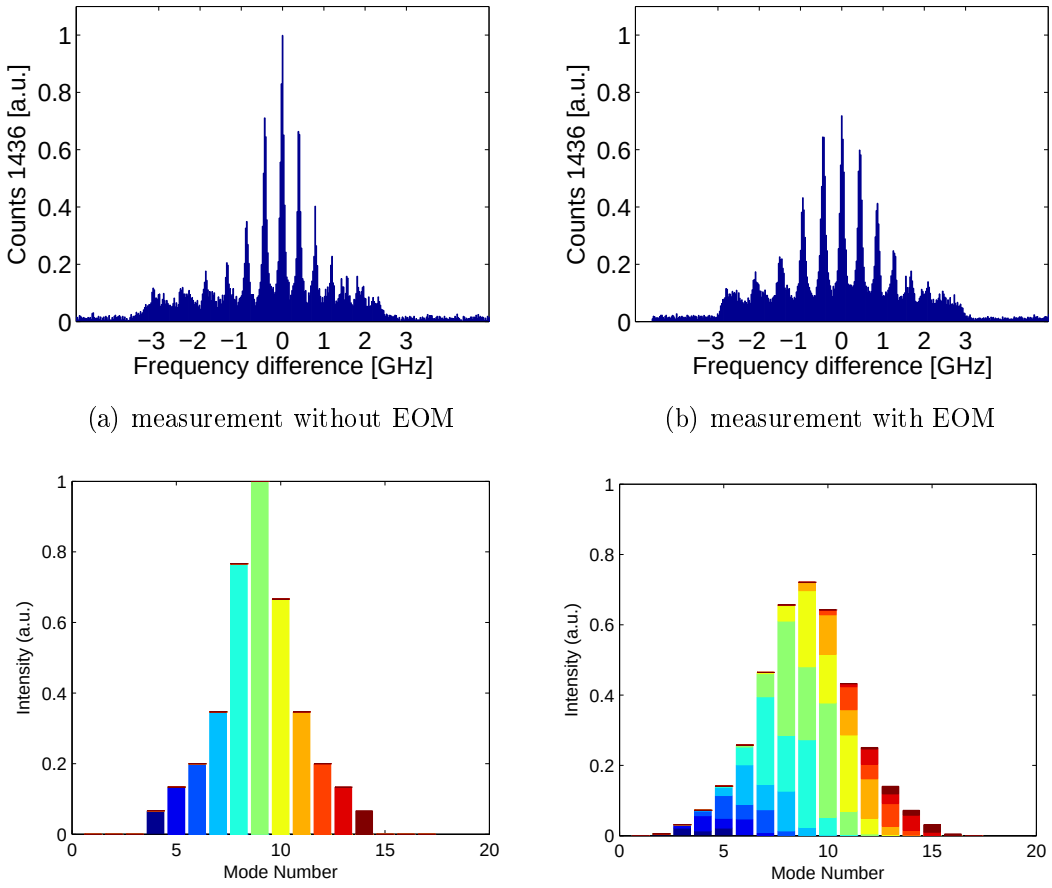

(a) measurement without EOM

(b) measurement with EOM

(c) simulation without EOM

(d) simulation with EOM

Figure 6.5: (a) Spectral measurement of frequency bins using a method explained in 3.2.5 (at idler frequency), generated by the source without action of the EOM. (c) Simulation of frequency bins, each bin is encoded in a different color and intensities g_n are obtained from measured spectrum in (a). (d) Action of EOM with modulation index of 1.6 is simulated to the frequency bins. Sidebands are created and overlap with neighboring modes. Colors denotes the origin of the bins. Phase difference lead to interference effects. (b) Measurement of the spectrum when sidebands are created by the EOM with a modulation index of $b = 1.6$, the intensities of the modes agree with the simulation.

6.2.2 Detection probability

In the experiment we then measure the coincidence rate of the photon pairs. between detecting a signal and an idler photon. Here the idler photon is filtered to a single mode (frequency) after passing the modulator and we assume this mode has the number l. The probability to find its partner photon in mode $l+d$ is then the following:

$$\begin{aligned} P_d\left(a,\alpha,b,\beta;l\right) &= \left|\langle l|\left\langle -l+d\right|\tilde{\Psi}\right\rangle\right|^2 \quad \text{with} && (6.6)\\ \langle l|\left\langle -l+d\right|\tilde{\Psi}\right\rangle &= \sum_n\sum_k\sum_m U_k\left(a,\alpha\right)U_m\left(b,\beta\right)g_n\left\langle l\left|n+k\right\rangle\right\langle -l+d\left|-n+m\right\rangle \end{aligned}$$

The modes are orthogonal and normalized which results in some simplifications:

$$\begin{aligned} \left\langle l\left|n+k\right\rangle\right. &= \delta_{l,n+k} && (6.7)\\ \left\langle -l+d\left|-n+m\right\rangle\right. &= 1 \quad \text{for} \quad -l+d=-n+m && (6.8)\\ &\Rightarrow\ P_d\left(a,\alpha,b,\beta;l\right)\neq 0 \quad \text{only for} \quad d=m+k && (6.9) \end{aligned}$$

$$\begin{aligned} \langle l|\left\langle -l+d\right|\tilde{\Psi}\right\rangle &= \sum_n\sum_k J_k\left(a\right)J_{d-k}\left(b\right)\exp\left[i\left(k\alpha+\beta\left(d-k\right)-\pi/2d\right)\right]\\ &\cdot\ g_n\left\langle l\left|n+k\right\rangle\right\langle -l+d\left|-n-k+d\right\rangle && (6.10) \end{aligned}$$

The last expression contains only two sums over n,k.

6.3 Experimental demonstration of two photon interference fringes

6.3.1 Experimental setup

We generate photon pairs with the same source presented in Chapter 5 based on spontaneous parametric down conversion (SPDC) in an optical parametric oscillator (OPO). We use a narrowband pump laser at 426 nm to generate idler photons at 1436 nm (telecommunications E-band) and signal photons at 606 nm. The spectrum of the photons consists of several peaks, formed by longitudinal modes of the OPO cavity, obeying the double resonance condition. These modes

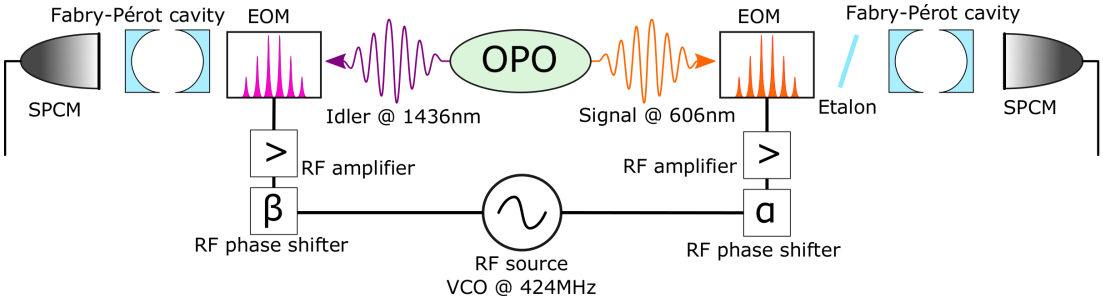

Figure 6.6: Sketch of components used for our entanglement analysis of the frequency-bin entanglement.

are separated by the cavity free spectral range. The Fourier transformation of a multi modal time correlation between signal and idler photons tells us $FSR = 423.7(1)\,\mathrm{MHz}$. The bandwidth of each mode is around 3 MHz.

To analyze the frequency-bin entanglement we include electro-optic modulators (EOM) in our setup as illustrated in Fig. 6.6. Each EOM is placed behind the source, before any spectral filter. We use a voltage controlled oscillator (VCO), tuned to 424 MHz as master oscillator. We split its radio frequency (RF) signal in two parts and feed it to the following components which are identical for the signal and idler branch. Each path for the RF contains a phase shifter, a variable attenuator and a high power amplifier to drive the EOM. Hence we can set the phase and power for each EOM individually. The effect of the EOM on the optical spectrum is the creation of sidebands, which overlap with the photon modes created by the OPO.

Our source setup further contains tunable Fabry-Pérot cavities which we use to select a single mode of the spectrum and that can be stabilized to a reference laser. Due to this preconditions our source is well suited to demonstrate frequency-bin entanglement.

6.3.2 Modulated spectra

As the RF is matched to the cavity FSR, the side bands of one mode will overlap with its neighboring modes. This creates the superposition of frequency bins necessary to show entanglement. The resulting spectra of the single photons with the EOMs turned on are shown in Fig. 6.7. The width of the peaks in that

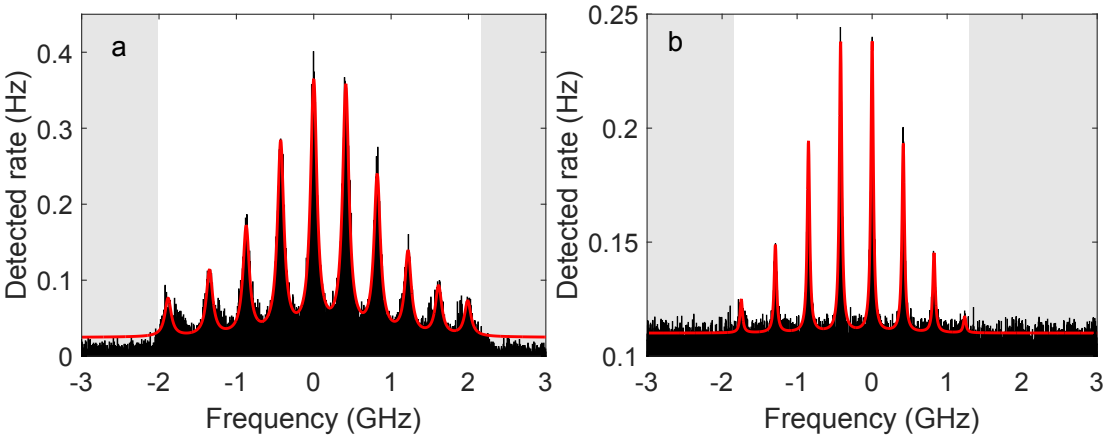

Figure 6.7: Spectra with active EOM for idler (a) and signal (b). We fitted sums of Lorentzians to the experimental data, shown as red solid lines. The gray shaded areas indicate the phase where the detectors are blocked and the source is locked to the reference laser.

figure is limited by the resolution of the Fabry-Pérot cavities, which is different for signal and idler wavelengths. In the insets of Fig. 6.7 the sidebands created by the EOMs are shown. From the ratio of the peak height we infer a modulation index $b = 1.36$ for idler and $a = 1.30$ for signal. We keep these values constant during all the measurements. The modulation index can be adjusted by the RF power sent to the EOMs. We monitor of the RF amplitude at each data point with an oscilloscope and adjust slight deviations due to different setting on the phase shifters.

6.3.3 Measurement of two-photon interference fringes

In a first step we measure the coincidences between single modes for different phases. The fringes as function of the phase difference are described by Bessel functions and depend on the modulation indices. In particular we decided to use equal depths for a and b in the range of 1.3 as we expect to achieve a rather high contrast for the coincidence rate with these settings. The result is shown in Fig. 6.8. We first set the phase of idler EOM to $\beta = 0°$ and varied the signal EOM phase only (green curve in Fig. 6.8). Next we set the idler EOM phase to $\beta = 51°$ and repeated the measurement (blue curve in Fig. 6.8). In both cases the filter

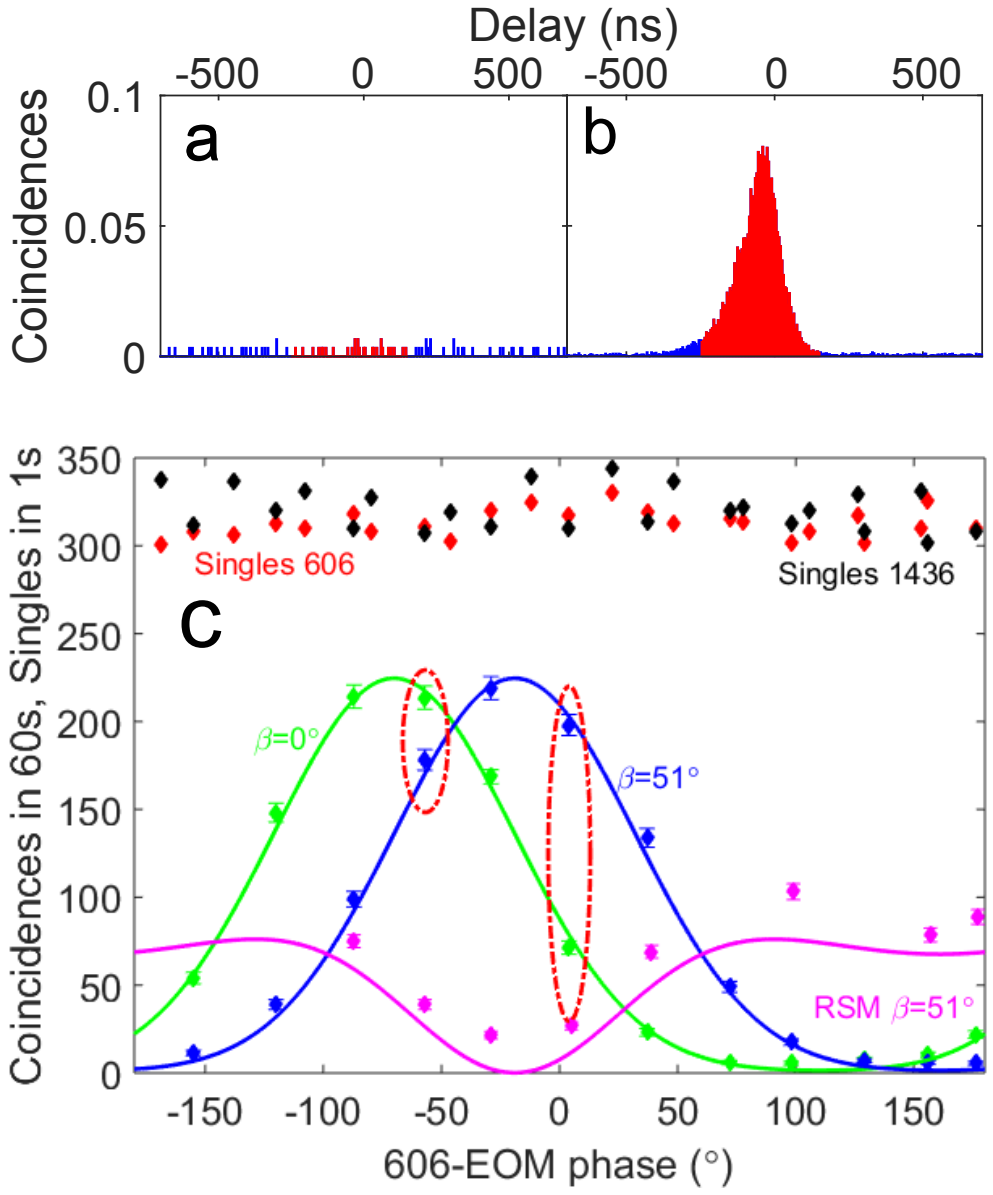

Figure 6.8: Results of the correlation measurements. (a) Shows the correlation histograms for minimum ($\beta = 178°$,$\beta = 51°$, left) and (b) maximum ($\beta = -29°$,$\beta = 51°$, right). To determine the coincidence rate we integrate over a 400 ns interval, indicated by the red shaded region. (c) The red and black points show the measured single rates for signal and idler, respectively. The green points show the coincidence rate for idler phase set to $\beta = 0°$ while for the blue points $\beta = 51°$. Both signal and idler filter cavities were set to mode $|0\rangle$. The magenta points show coincidences with $\beta = 51°$ and the idler filter selecting mode $|+1\rangle$. The solid lines show fits to the data according to a model from [113]. The measured points surrounded by the red ovals are used for further calculations with a Bell inequality.

cavities were actively stabilized to the central mode (mode $|0\rangle$) of the spectra, corresponding to the central frequency bins of each spectrum. For comparison, the magenta data points in the figure show the results when the idler cavity is set to a mode next to the central mode (mode $|+1\rangle$) while the signal filter is still centered.

The variation of the coincidence rate induced by the change of the RF phase is a signature of a two-photon interference effect, which is a proof of coherent superposition between frequency terms. From the raw data, shown in Fig. 6.8, we find an interference visibility of $V = 95(4)\,\%$. Which is a strong indicator for entanglement since we measured the same visibility for two different non-orthogonal settings of Bob's analyzer (blue and green fringe).

The solid lines shown in the figure are to guide the eye. They are obtained from Bessel-functions based on the model presented in [113]. These model can not be applied directly to our data, since our spectrum contains modes of different heights, leading to an increased value for the magenta points. The evaluation with a modified model which includes different intensities for each mode is given in section 6.5.2. First we were interested in the violation of a Bell inequality. The points surrounded by the red oval are at the optimized settings (according to the model of Olislager [113]) for the violation of the Bell inequality.

6.4 Bell inequalities for frequency entangled states

A device independent proof for entanglement, independent from the number of dimensions, could be the violation of Bell inequalities. In the next section a Bell inequality is presented, which has been derived in collaboration with theorists[1] from ICFO, which matches with our system.

6.4.1 Derivation of Bell inequality

We can use a Clauser-Horne inequality [114] which we adapted to our system:

[1] Osvaldo Jimenez, Daniel Cavalcanti, Alejandro Máttar and Antonio Acín

$$P(00|A_1B_1) + P(00|A_1B_2) + P(00|A_2B_1) - P(00|A_2B_2) \\ -P(0|A_1) - P(0|B_1) \leq 0. \tag{6.11}$$

Here $P(00|A_xB_x)$ describes the probability of measuring a coincidence with the filters set to the central mode and with a setting A_x of the EOM in the signal arm and a setting B_x of the EOM in the idler arm. $P(0|x)$ describe the marginal probabilities to find a single photon in each arm. As it can be deduced from the constant single rates in Fig. 6.8, the marginals are independent from the phase setting of the EOMs.

In an experiment with photons, the probability outcomes correspond to photon counts $C(xy|ab)$ normalized by the total number of events $\sum_{ab} C(xy|ab)$ (sum over all the possible outputs), that is

$$P(ab|xy) = \frac{C(ab|xy)}{\sum_{ab} C(ab|xy)} \tag{6.12}$$

6.4.2 Additional measurements for normalization and marginals

In practice we can not measure each outcome one by one. The total number of events $\sum_{ab} C(ab|xy)$ has to be measured in a different way. In order to do so, we bypass the Fabry-Pérot cavities to detect all the possible outcome modes at once and then we correct by a transmission coefficient. That is, our measure probabilities must be written as

$$P(ab|xy) = \frac{C(ab|xy)}{N(xy)}, \tag{6.13}$$

where $N(xy) = \eta_{tot} \sum_{ab} C(ab|xy)$ with $\eta_{tot}^T = \eta_s^T \eta_i^T$ the total transmission, which is the product of the transmission on the signal (idler) mode $\eta_s(i)$ passing the filter cavities.

$\sum_{ab} C(ab|xy) \equiv C^{MM}$ can be obtained by a coincidence measurement of all spectral modes bypassing both filter cavities. The transmission coefficients η_i^T and η_s^T can be obtained by

$$\eta_{i,s}^T = \frac{C_{i,s}^{FC}}{C^{MM} \cdot \xi} \tag{6.14}$$

with ξ the intensity ratio between the central mode and the sum of the modes derived from the measured spectrum in Fig. 6.7. Additional coincidence measurements C_s^{FC} (C_i^{FC}) are required with a filter cavity in the signal (idler) arm while there is no filter cavity in the other arm. In contrast to measurements with single photon rates, these measurements of coincidences are independent from uncorrelated noise.

The marginal probabilities $P(0|x)$ are given by the normalized amount of correlated photons in each arm. The amount of correlated photons in each arm $C(0|x) = \sum_b C(0b|xy) = \sum_a C(a0|xy)$ can be obtained from the same measurements, bypassing one filter cavity $\sum_b C(0b|xy) = \eta_i C_i^{FC}$ and $\sum_a C(a0|xy) = \eta_s C_s^{FC}$. After that, we normalize by $N(x(y)) = \eta_{tot} \sum_{ab} C(ab|xy) = \eta_s \eta_i C^{MM}$.

6.4.3 Bell-inequalities obtained from coincidences

In order to measure the Bell correlations, we have taken the coincidence rates C_{ij} for two different settings of A and B, obtained from the fringes in Fig. 6.8. In addition we had to take measurements with the spectral filters in just one arm on each side obtaining the results C_i^{FC} with the filter cavity in the idler arm and C_s^{FC} with the filter cavity in the signal arm. In addition a measurement without any filter cavity was taken, to get the coincidence rate C^{MM}. The Bell inequality can then be written as:

$$\frac{C_{00} + C_{01} + C_{10} - C_{11}}{C^{MM} \cdot \eta_i^T \cdot \eta_s^T} - \frac{C_i^{FC}}{\eta_i^T \cdot C^{MM}} - \frac{C_s^{FC}}{\eta_s^T \cdot C^{MM}} \leq 0 \tag{6.15}$$

replacing the transmissions $\eta_{i,s}^T$ by coincidence measurements given in Eq. 6.14 we rewrite 6.15 to:

$$(C_{00} + C_{01} + C_{10} - C_{11}) \cdot \frac{C^{MM} \cdot \xi}{C_i^{FC} \cdot C_s^{FC}} \leq 2. \tag{6.16}$$

6.4.4 Experimental investigation of Bell inequality violation

To test our measurement against the new Bell inequality we use the data points at phases $\alpha = -57°$ and $\alpha = 4°$. Our simulation predicted the highest Bell

value for these four points in our set of measurements. By-passing just the idler filter cavity gave a coincidence rate of 5.4(1) Hz (4.8(1) Hz if accidental floor is subtracted). By-passing the signal filter cavity results in a coincidence rate of 25.4(3) Hz (24.7(3) Hz). Both cavities bypassed we measured a coincidence rate of 114.7(6) Hz (105.1(6) Hz), with all modes contributing. From the signal spectrum shown in Fig. 6.7 we got $\xi = 0.255$. With Eq. 6.14 that results in a transmission efficiency of $\eta_{i,s}^T = 86.2\,\%$ for the idler cavity and $\eta_s^T = 18.4\,\%$ for the signal cavity.

Including these values in Eq. 6.16 we get following result for a first measurement we did, without the subtraction of accidental background:

$$(3.56 + 2.97 + 3.3 - 1.19) - 2 \cdot \frac{114.7 \cdot 0.255}{5.44 \cdot 25.37} = 1.83 \pm 0.19 \tag{6.17}$$

and 1.95 ± 0.21 if we subtract accidental background. Since these values are below 2, we don't violate the derived Bell inequality, with the phase settings we used, although they were optimized for our modulation indices. This is at first sight surprising, since our two-photon interference visibility is very high 95 %. In the next section, we investigate this issue with a deeper analysis of our data, additional measurements and the simulation presented in section 6.2.2.

6.5 Interpretation with simulated state

6.5.1 Additional measurement of spectral components

To get an idea about outcomes we could not measure one by one, we took additional measurements of the spectrum shown in Fig. 6.9.

We scanned the filter cavity in the signal arm, while the cavity in the idler arm was stabilized to a central mode. The EOMs had the same modulation index as in the previous measurement. The phase of the EOMs where set once to the maximum (Fig. 6.9 (a)) of the interference fringe and the other time to the minimum (Fig. 6.9 (b)). In blue the single rates as dependence of filter cavity length (resulting in the spectral position) are shown. In green just the single photons conditioned on a click at the heralding detector are shown. At the minimum (in Fig. 6.9 (b)) we see that the counts spread over six outputs,

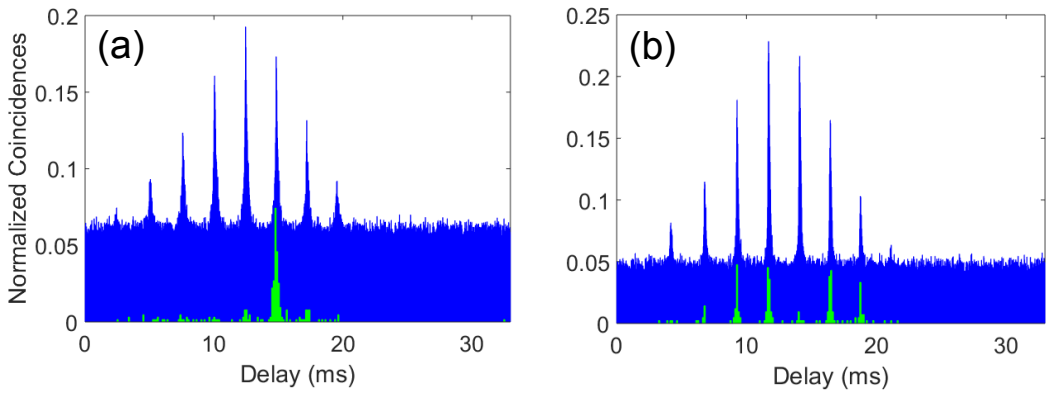

Figure 6.9: Spectrum of uncorrelated signal photons in blue and conditioned on idler photons in the central frequency bin in green. (a) phases were set to the maximum interference fringe (b) at minimum of interference fringe.

with no counts in the central mode.At the maximum (Fig. 6.9 (a)) of the fringe we find 87 % of the photons in the central peak and the residual photos equally distributed in the neighboring modes. This is due to the fact that our state is non-maximally entangled, resulting in a not complete destructive interference for the side modes. This fact has direct consequences on the normalization factor for the Bell inequality. Since we have to normalize with all the events the probability to find a photon at the maximum is 87 % below 1.

6.5.2 Simulation of measured state

To further investigate this issue, we can use the model presented in section 6.2.1. With this model, we can simulate the coincidence rate for all the modes from the state given in Eq. 6.5, which includes the unitary transformation performed by the EOMs on the non-maximal entangled state expressed in Eq. 6.2. The solid lines in Fig. 6.10 are simulated coincidence rates, we get from 6.10 for the phase setting applied to the measurement. We can take the sum of all modes as maximum of the achievable counts in the central bin (see Fig. 6.10). The dashed line represents the sum of all modes as reference of the achievable coincidences from the different possible outcomes. We see that even at the maximum of the fringe, the counts are lower than the reference. This means that with our created

non-maximally entangled state, it is not possible to find phase settings where all the coincidence go in the central bin, if we use the same modulation indices. This prevents the violation of the Bell inequality with these settings. Thus the normalization constant stays well above the maximum of our interference fringes. With the simulation we get an Bell parameter of $S = 2.03 \pm 0.06$, which agrees inside the error bars with our measurements.

Since our measured data match quite well with the simulated lines, we conclude that our model indeed describes our experiment. As the initial state our model is based on, is an entangled state we here claim that our photons are frequency-bin entangled.

6.6 Towards storage of frequency entanglement in the quantum memory

We demonstrated earlier, that we can store heralded single photons created by this source in a solid state quantum memory [73]. In the future we plan to combine the effect of frequency-bin entanglement with quantum storage. As a preparatory step we now include our quantum memory setup into the experiment. As illustrated in Fig. 6.11 we replace the filtering cavity in the signal arm by the doped crystal.

We use a Praseodymium doped Y_2SiO_5 crystal. The inhomogeneous broadening of the transition at 606 nm results in total absorption of all signal modes created by our OPO. However, we can create a transmission window via spectral hole burning, i.e. with the help of a narrow band tunable laser we pump a certain species of ions to another ground state. With this technique we tailor a window of 8 MHz featuring high transmission for the mode $|0\rangle$ only. We measure coincidences between the single mode signal photons filtered in that way and the idler photons filtered to a single mode with the help of the cavity, as explained before. The coincidence rate is reduced due to increased losses in the signal arm and an additional duty cycle, necessary to periodically refresh the spectral hole filter. As shown in Fig. 6.11 we still observe interference fringes with high visibility.

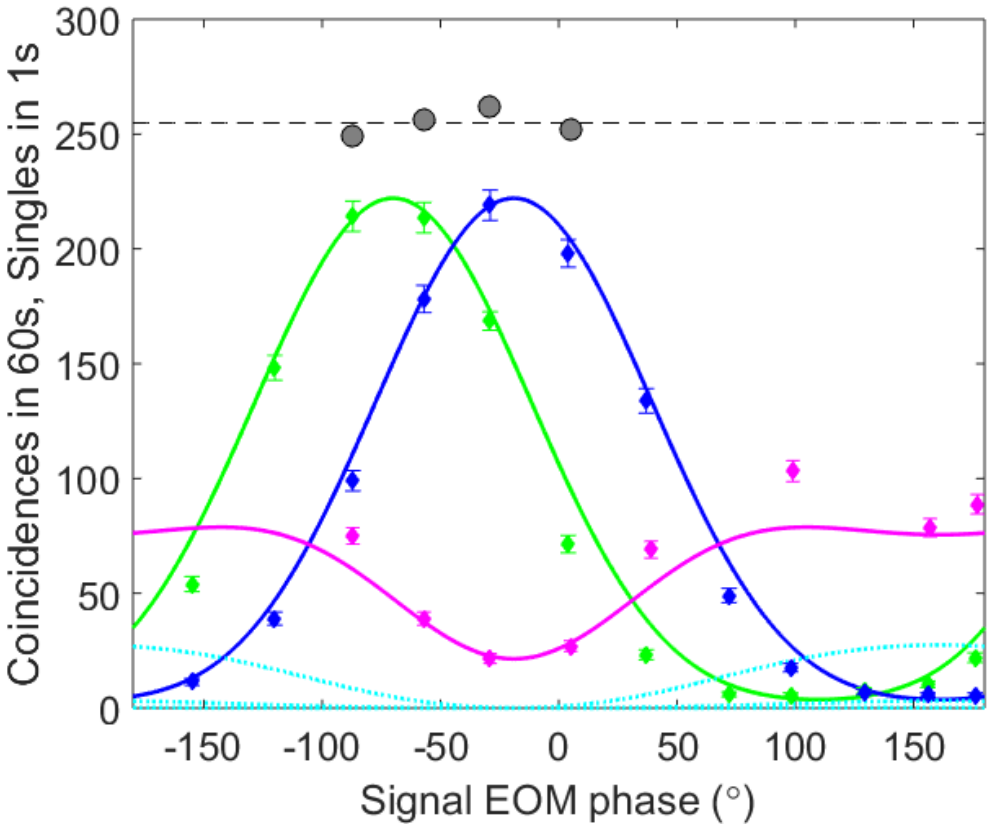

Figure 6.10: Data taken at coincidence measurement together with simulations of output rates. The green and blue line represent the simulated outcome for the central frequency bins. The solid magenta line represent the coincidence rate, between a central mode and the neighboring modes, the cyan lines represent the coincidence rates with further neighbors. A sum of all the possible combinations is given by the dashed gray line, which serves as reference rate. The gray circles display the sum of blue data points and two times the magenta data points (for left and right neighboring modes).

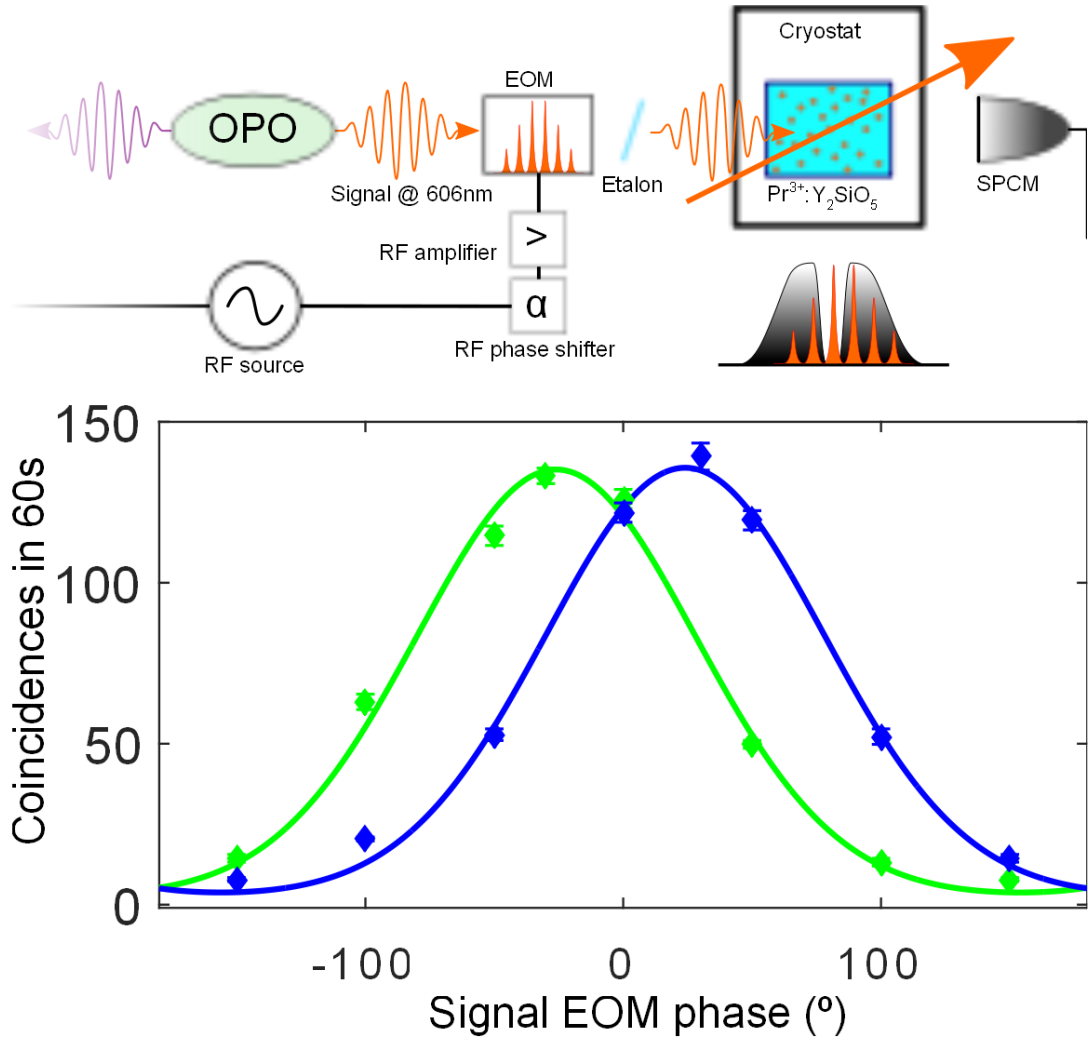

Figure 6.11: Modification of the experimental setup (top): The filter cavity at the idler branch was replaced by our memory setup. We create a spectral filter by spectral hole burning techniques. The resulting coincidence measurement (bottom) shows interference fringes.

We repeated this measurements for different pump powers of our source. Increasing the pump power will increase the probability to create multiple pairs in the SPDC process. This reduces the fidelity of the heralded single photon. This effect can be observed in a decrease of the signal-idler cross correlation value $g^{(2)}_{s,i}$. The result is summarized in Fig. 6.12. For all available pump powers we operate in a high visibility regime.

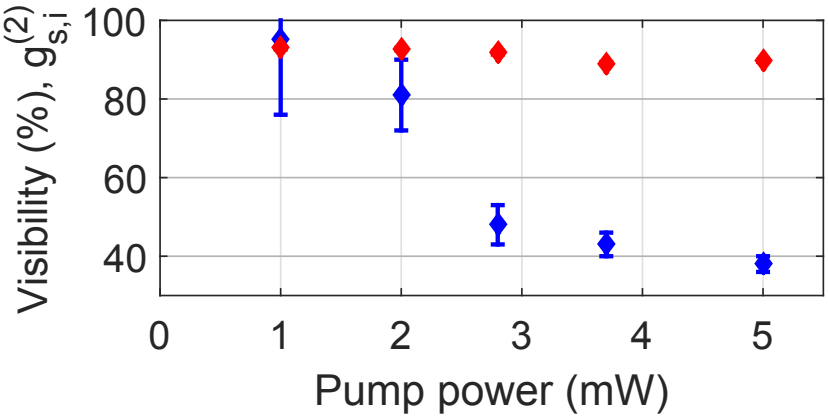

Figure 6.12: Measured interference raw visibility (red) and cross correlation value $g^{(2)}_{s,i}$ (blue) for different pump powers.

We observe a small decrease of visibility with pump power. However, the lowest visibility for all accessible pump powers was still quite high with $V \geq 89.2 \pm 3\%$.

To finally store a frequency-bin entangled qudit a few changes in our memory setup are necessary. We use the atomic frequency comb (AFC) technique for storage. This involves creating a periodic absorption feature within the spectral hole we used for filtering. We already demonstrated this for a single frequency mode [73], but to store a frequency-bin qudit several AFCs, one for each mode is necessary. This would allow us to store the photon in a superposition of frequency bins which is essential to preserve the qudit state. The EOM for analysis of the entanglement has then to be placed behind the memory. The creation of multiple AFCs has been demonstrated [24, 69] elsewhere, in a Tm doped crystal.

6.7 Conclusion

We demonstrated frequency bin entanglement with a source creating frequency bins intrinsically. That opens the way to use this type of entanglement with narrowband sources compatible with quantum memories which allow frequency multiplexing. The high visibility of the two photon interference fringes shows a coherent superposition, which is a good indicator of entanglement. The agreement between our data and a model inferred from the measured photon spectrum also suggests that our state is close the ideal entangled state. To show a clear violation of Bell inequalities the modulation indices on the EOMs have to be adjusted. The simulation predicts a better violation with lower sidebands. On the other hand the visibility of the interference fringes could decrease with too low sidebands. Thus a careful adjustment of the setting related to the present spectra will be required, to be able to violate the presented Bell inequality.

7

Conclusions

Quantum repeaters could enable the transfer of a quantum state over distances larger than few hundreds of kilometers. A crucial requirement for a quantum repeater is the distribution of entanglement between remote quantum memories. Photon pair sources which create photons at telecom wavelength entangled with photons stored in a quantum memory are a promising solution towards that goal. During my PhD project we developed such a source of entangled photon pairs, of which one is connected with a solid state quantum memory and it's partner photon is at telecom wavelength. This source was then used for experiments with a Pr^{3+}-doped solid state quantum memory. Finally, entanglement between the frequency modes of the created photons has been investigated.

7.1 Achievements

First the source was built and characterized as shown in chapter 3. The spectral requirements for storing heralded single photons in a Pr^{3+}-doped crystal were achieved by demonstrating a photon bandwidth of 2 MHz, the narrowest photon pairs produced by SPDC so far, which can be filtered to a single spectral mode. In addition the ultra wide non-degeneracy allowed us to have a heralding photon at telecom wavelength and to investigate the clustering effect for widely non-degenerate double resonant cavity enhanced SPDC.

After fully characterizing the source we performed experiments by connecting it to our solid state quantum memory, based on a Praseodymium doped crystal.

Using the AFC storage protocol, we could store the heralded single photons for up to 4.5 µs, twenty times longer than in previous experiments using solid state QMs. This storage time would be long enough to distribute entanglement over 1 km.

To enlarge the possible distance longer storage times are required. A possibility to extend the storage time is to transfer the single excitation into a long lived spin state, which is present in the level structure of the praseodymium ions. That also allows an on demand readout of the quantum memory. To be able to apply the source for that storage, its performance had to be improved with respect to the previous storage experiments. An important parameter for that experiment was the heralding efficiency of the photons in front of the memory. A heralding efficiency of 28 % was demonstrated. Further more the detected coincidence rate for a single frequency bin has been improved by an order of magnitude and a significant improvement of the cross-correlation function $g^{(2)}_{s,i}$, was reported. Details are described in chapter 5. The photon pair source runs stable with a good performance and no further improvement on this source is planed so far. The active stabilization holds for up to 18 hours, such that experiments can be performed over night. Further improvements on the source, like a narrower line width or a higher heralding efficiency, will require a modified design.

With improved performance we connected the source to the quantum memory again and achieved improved results for the AFC storage as well as a first storage in the spin state violating the classical condition $g^{(2)}_{si} > \sqrt{g^{(2)}_{ss} \cdot g^{(2)}_{ii}}$ and a total storage time of 11 µs. Preliminary results are shown in the thesis and the ongoing work of my successors shows major improvements on the results.

A further goal of the thesis was to show entanglement between the photons of the pairs. A first approach to implement polarization entanglement was not successful. Instead we took advantage of the fact that our spectrum contains several longitudinal modes and showed entanglement of the frequency bins of the pairs using a technique introduced by Olislager et al. [74]. High visibility ($\approx$ 95 %) two photon interference fringes have been demonstrated, showing coherent superposition of the frequency modes. A Bell inequality has been derived. The results have been explained with a simulation of the multidimensional state, which showed entanglement.

7.2 Discussion

In contrast to many experiments with quantum memories using weak coherent states, in this thesis heralded single photons were generated and stored in a quantum memory. We did first measurements on a system consisting of correlated photon pairs linked with a solid state quantum memory offering the possibility of an on demand readout.

The fact that one photon of the pair is at telecom wavelength while the other one can be stored in a quantum memory, offers the possibility to entangle two distant quantum memories with each other by copying the setup and perform swapping operations on the two telecom arms. That could be a first building block of a quantum repeater. The current storage time of the quantum memory would be enough to distribute the entanglement over few kilometers while the quantum state is stored in the quantum memories. The efficiency of the joint system would lead to count rates in the sub Hz regime, still too low for applications. However, we showed very fast progress in the performance of source and solid state quantum memory. The fast and continuous improvement of source and quantum memory is promising for the future.

The cavity enhanced approach avoids the use of narrow spectral filtering components and brings an enhancement of the spectral brightness. Here we demonstrated not only one of the spectrally narrowest photon pair source, but also the one with the lowest signal photon wavelength and the widest separation of signal and idler photons. This is based on a strong suppression of redundant modes due to the clustering effect for double resonance. Many photon pair sources exist of this type, but only a few are demonstrated to be resonant with an atomic quantum memory. Connecting the source to our quantum memory not only showed the resonance with an atomic system, but also the storage and retrieval of non-classical light.

Our approach towards frequency entanglement between the two photons is ideally suited for such a type of narrowband sources, since they inherently create narrowband frequency bins. The high visibility competes with other types of entanglement and the multi-modality might bring an advantage on the robustness of quantum key distribution and allows an implementation of frequency

multiplexing.

7.3 Outlook

We demonstrated a first example of quantum light source compatible with Pr doped solid state quantum memories. However, several improvements could be made. A new source is already in development, it will provide a narrower linewidth due to a longer cavity length. This could increase the storage efficiency in the quantum memory, since the actual linewidth of the photons doesn't completely match the spectral shape of the AFC.

Furthermore it is planed to store multiple frequency bins which leads to two advantages. One is to show the possibility of frequency multiplexing for the quantum memory and the second is to show the storage of frequency bin entangled photons. In addition the source offers a multi dimensional type of entanglement which allows further investigation on qudit states.

When the second source is finished it can be connected with a second Pr^{3+}-doped solid state quantum memory, present in one of our labs. That would enable the possibility to entangle two quantum memories with a swapping operation on the telecom photons.

Further improvement on the memory could enable longer the storage times. A long storage time in the second regime, with high storage efficiencies is crucial for long distance quantum communication.

Another interesting direction would be to explore the possibility to make quantum memory compatible sources with whispering gallery mode resonators [53]. This would have the advantage of increased stability. However, it is likely that PPLN would not be a suitable material for this task, because of the losses at 606 nm and 426 nm, preventing the realization of high-Q cavities.

Finally, our source could be adapted to achieve light-matter interaction with other matter systems such as NV centers ($\lambda = 637$ nm), or Europium doped solids (580 nm), which possess extremely long coherence times. Especially for the NV center the requirements on wavelength and linewidth are very similar to what we have demonstrated. Furthermore, a storage time in the second range has been demonstrated recently [115] as a first step to diamond based quantum repeaters.

Secure communication using quantum key distribution would be just one example of a possible application. Phase modulated light as used in our frequency-bin entanglement experiments can be used for this purpose [116].Another long term possibility would be to connect optical clocks with each other and create a more accurate time synchronization, than it is possible with classical light, that could also improve the sensitivity of GPS-systems [117]. Another work [118] suggests to use quantum repeaters for a higher resolution of stellar observations with remote telescopes connected by a quantum channel. Probably much more quantum applications will appear with time.

References

[1] W. K. Wootters and W. H. Zurek. A single quantum cannot be cloned. *Nature*, 299(5886):802–803, 1982. ISSN 0028-0836. doi: 10.1038/299802a0. URL http://www.nature.com/nature/journal/v299/n5886/abs/299802a0.html. 2, 3

[2] D. Bouwmeester, J.-W. Pan, K. Mattle, M. Eibl, H. Weinfurter, and A. Zeilinger. Experimental quantum teleportation. *Nature*, 390 (6660):575–579, 1997. ISSN 0028-0836. doi: 10.1038/37539. URL http://www.nature.com/nature/journal/v390/n6660/abs/390575a0.html. 3

[3] M. Halder, A. Beveratos, N. Gisin, V. Scarani, C. Simon, and H. Zbinden. Entangling independent photons by time measurement. *Nature Physics*, 3(10):692–695, 2007. ISSN 1745-2473. doi: 10.1038/nphys700. URL http://dx.doi.org/10.1038/nphys700. 3

[4] A. Ekert and R. Jozsa. Quantum computation and shor's factoring algorithm. *Rev. of Mod. Phys.*, 68(3):733–753, 1996. ISSN 00346861. doi: 10.1103/RevModPhys.68.733. URL http://journals.aps.org/rmp/abstract/10.1103/RevModPhys.68.733. 3

[5] L. M. Vandersypen, M. Steffen, G. Breyta, C. S. Yannoni, M. H. Sherwood, and I. L. Chuang. Experimental realization of Shor's quantum factoring algorithm using nuclear magnetic resonance. *Nature*, 414(6866):883–7, 2001. ISSN 0028-0836. doi: 10.1038/414883a. URL

http://www.nature.com/nature/journal/v414/n6866/abs/414883a.html. 3

[6] E. Lucero, R. Barends, Y. Chen, J. Kelly, M. Mariantoni, A. Megrant, P. Malley, D. Sank, A. Vainsencher, J. Wenner, T. White, Y. Yin, A. N. Cleland, and J. M. Martinis. Computing prime factors with a Josephson phase qubit quantum processor. *Nat. Phys.*, 8(10): 719–723, 2012. ISSN 1745-2473. doi: 10.1038/nphys2385. URL http://www.nature.com/nphys/journal/v8/n10/full/nphys2385.html. 3

[7] C. H. Bennett and G. Brassard. Quantum cryptography: Public key distribution and coin tossing. *IEEE International Conference on Computers, Systems and Signal Processing*, 175:8–12, 1984. 3

[8] N. Gisin and R. Thew. Quantum communication. *Nat Photon*, 1(3):165–171, Mar 2007. ISSN 1749-4885. doi: 10.1038/nphoton.2007.22. URL http://dx.doi.org/10.1038/nphoton.2007.22. 3

[9] B. Korzh, C. C. W. Lim, R. Houlmann, N. Gisin, M. J. Li, D. Nolan, B. Sanguinetti, R. Thew, and H. Zbinden. Provably secure and practical quantum key distribution over 307 km of optical fibre. *Nature Photonics*, 9, feb 2015. ISSN 1749-4893. doi: 10.1038/nphoton.2014.327. URL http://dx.doi.org/10.1038/nphoton.2014.327. 4

[10] H.-J. Briegel, W. Dür, J. I. Cirac, and P. Zoller. Quantum repeaters: The role of imperfect local operations in quantum communication. *Phys. Rev. Lett.*, 81:5932–5935, Dec 1998. doi: 10.1103/PhysRevLett.81.5932. URL http://link.aps.org/doi/10.1103/PhysRevLett.81.5932. 4

[11] L.-M. Duan, M. D. Lukin, J. I. Cirac, and P. Zoller. Long-distance quantum communication with atomic ensembles and linear optics. *Nature*, 414 (6862):413–418, Nov 2001. ISSN 0028-0836. doi: 10.1038/35106500. URL http://dx.doi.org/10.1038/35106500.

[12] N. Sangouard, C. Simon, H. De Riedmatten, and N. Gisin. Quantum repeaters based on atomic ensembles and linear optics. *Rev. Mod. Phys.*, 83(1):33–80, 2011. ISSN 00346861. doi: 10.1103/RevModPhys.83.33. URL http://journals.aps.org/rmp/abstract/10.1103/RevModPhys.83.33. 4, 6, 9, 10, 62

[13] C. Simon, H. de Riedmatten, M. Afzelius, N. Sangouard, H. Zbinden, and N. Gisin. Quantum repeaters with photon pair sources and multimode memories. *Phys. Rev. Lett.*, 98: 190503, May 2007. doi: 10.1103/PhysRevLett.98.190503. URL http://link.aps.org/doi/10.1103/PhysRevLett.98.190503. 6, 8, 9, 11, 15, 93

[14] O. A. Collins, S. D. Jenkins, A. Kuzmich, and T. A. B. Kennedy. Multiplexed memory-insensitive quantum repeaters. *Phys. Rev. Lett.*, 98:060502, Feb 2007. doi: 10.1103/PhysRevLett.98.060502. URL http://link.aps.org/doi/10.1103/PhysRevLett.98.060502. 6

[15] J.-W. Pan, C. Simon, C. Brukner, and A. Zeilinger. Entanglement purification for quantum communication. *Nature*, 410(6832):1067–1070, Apr 2001. ISSN 0028-0836. doi: 10.1038/35074041. URL http://dx.doi.org/10.1038/35074041. 6

[16] W. J. Munro, A. M. Stephens, S. J. Devitt, K. A. Harrison, and K. Nemoto. Quantum communication without the necessity of quantum memories. *Nat Photon*, 6(11):777–781, Nov 2012. ISSN 1749-4885. doi: 10.1038/nphoton.2012.243. URL http://dx.doi.org/10.1038/nphoton.2012.243. 6

[17] N. Sangouard. Quantum networks: A future without long memories? *Nat Photon*, 6(11):722–724, Nov 2012. ISSN 1749-4885. doi: 10.1038/nphoton.2012.268. URL http://dx.doi.org/10.1038/nphoton.2012.268.

[18] K. Azuma, K. Tamaki, and H.-K. Lo. All-photonic quantum repeaters. *Nat Commun*, 6, Apr 2015. URL http://dx.doi.org/10.1038/ncomms7787. Article. 6

[19] R. H. Hadfield. Single-photon detectors for optical quantum information applications. *Nat. Photon.*, 3(12):696–705, 2009. ISSN 1749-4885. doi: 10.1038/nphoton.2009.230. URL http://www.nature.com/nphoton/journal/v3/n12/full/nphoton.2009.230.html. 9

[20] A. E. Lita, A. J. Miller, and S. W. Nam. Counting near-infrared single-photons with 95% efficiency. *Opt. Express*, 16 (5):3032–3040, Mar 2008. doi: 10.1364/OE.16.003032. URL http://www.opticsexpress.org/abstract.cfm?URI=oe-16-5-3032. 9

[21] I. Usmani, M. Afzelius, H. de Riedmatten, and N. Gisin. Mapping multiple photonic qubits into and out of one solid-state atomic ensemble. *Nat Commun*, 1:12, Apr 2010. doi: 10.1038/ncomms1010. URL http://dx.doi.org/10.1038/ncomms1010. 11

[22] M. Bonarota, J.-L. Le Gouët, and T. Chaneliáre. Highly multimode storage in a crystal. *New Journal of Physics*, 13(1):013013, 2011. URL http://stacks.iop.org/1367-2630/13/i=1/a=013013.

[23] C. Laplane, P. Jobez, J. Etesse, N. Timoney, N. Gisin, and M. Afzelius. Multiplexed on-demand storage of polarization qubits in a crystal. *New Journal of Physics*, 18(1):013006, 2016. URL http://stacks.iop.org/1367-2630/18/i=1/a=013006. 11

[24] N. Sinclair, E. Saglamyurek, H. Mallahzadeh, J. A. Slater, M. George, R. Ricken, M. P. Hedges, D. Oblak, C. Simon, W. Sohler, and W. Tittel. Spectral multiplexing for scalable quantum photonics using an atomic frequency comb quantum memory and feed-forward control. *Phys. Rev. Lett.*, 113:053603, Jul 2014. doi: 10.1103/PhysRevLett.113.053603. URL http://link.aps.org/doi/10.1103/PhysRevLett.113.053603. 11, 68, 96, 113

[25] Z.-Q. Zhou, Y.-L. Hua, X. Liu, G. Chen, J.-S. Xu, Y.-J. Han, C.-F. Li, and G.-C. Guo. Quantum storage of three-dimensional orbital-angular-momentum entanglement in a crystal. *Phys. Rev. Lett.*, 115:

070502, Aug 2015. doi: 10.1103/PhysRevLett.115.070502. URL http://link.aps.org/doi/10.1103/PhysRevLett.115.070502. 11

[26] R. Lauro, T. Chanelière, and J. L. Le Gouët. Slow light using spectral hole burning in a tm^{3+}-doped yttrium-aluminum-garnet crystal. *Phys. Rev. A*, 79:063844, Jun 2009. doi: 10.1103/PhysRevA.79.063844. URL http://link.aps.org/doi/10.1103/PhysRevA.79.063844. 11

[27] R. Lauro, T. Chanelière, and J.-L. Le Gouët. Spectral hole burning for stopping light. *Phys. Rev. A*, 79: 053801, May 2009. doi: 10.1103/PhysRevA.79.053801. URL http://link.aps.org/doi/10.1103/PhysRevA.79.053801.

[28] A. Walther, A. Amari, S. Kröll, and A. Kalachev. Experimental superradiance and slow-light effects for quantum memories. *Phys. Rev. A*, 80:012317, Jul 2009. doi: 10.1103/PhysRevA.80.012317. URL http://link.aps.org/doi/10.1103/PhysRevA.80.012317. 11

[29] A. I. Lvovsky, B. C. Sanders, and W. Tittel. Optical quantum memory. *Nat. Phot.*, 3(12):706–714, 2009. ISSN 1749-4885. doi: 10.1038/nphoton.2009.231. URL http://www.nature.com/nphoton/journal/v3/n12/full/nphoton.2009.231.html. 11

[30] M. Afzelius, C. Simon, H. de Riedmatten, and N. Gisin. Multimode quantum memory based on atomic frequency combs. *Phys. Rev. A*, 79:052329, May 2009. doi: 10.1103/PhysRevA.79.052329. URL http://link.aps.org/doi/10.1103/PhysRevA.79.052329. 11, 57

[31] H. de Riedmatten, M. Afzelius, M. U. Staudt, C. Simon, and N. Gisin. A solid-state light-matter interface at the single-photon level. *Nature*, 456(7223):773–777, 2008. ISSN 0028-0836. doi: 10.1038/nature07607. URL http://www.nature.com/nature/journal/v456/n7223/abs/nature07607.html. 11, 58, 65

[32] C. Clausen, I. Usmani, F. Bussières, N. Sangouard, M. Afzelius, H. de Riedmatten, and N. Gisin. Quantum storage of photonic entanglement in a crystal. *Nature*, 469(7331):508–11, 2011. ISSN 1476-4687. doi: 10.1038/nature09662. URL http://www.ncbi.nlm.nih.gov/pubmed/21228774. 11, 13, 14, 15, 57, 58, 62, 67

[33] E. Saglamyurek, N. Sinclair, J. Jin, J. A. Slater, D. Oblak, W. Tittel, F. Bussières, M. George, R. Ricken, and W. Sohler. Broadband waveguide quantum memory for entangled photons (Invited Paper). In *2011 IEEE Photonics Society Summer Topical Meeting Series*, pages 4–5, 2011. ISBN 9781424457304. doi: 10.1109/PHOSST.2011.5999934. 11, 57, 58, 67

[34] I. Usmani, C. Clausen, F. Bussieres, N. Sangouard, M. Afzelius, and N. Gisin. Heralded quantum entanglement between two crystals. 6 (4):234–237. ISSN 1749-4885. doi: 10.1038/nphoton.2012.34. URL http://dx.doi.org/10.1038/nphoton.2012.34. 11, 13

[35] D. Schraft, M. Hain, N. Lorenz, and T. Halfmann. Stopped light at high storage efficiency in a pr^{3+} : y_2sio_5 crystal. *Phys. Rev. Lett.*, 116:073602, Feb 2016. doi: 10.1103/PhysRevLett.116.073602. URL http://link.aps.org/doi/10.1103/PhysRevLett.116.073602. 12

[36] G. Heinze, C. Hubrich, and T. Halfmann. Stopped light and image storage by electromagnetically induced transparency up to the regime of one minute. *Phys. Rev. Lett.*, 111: 033601, Jul 2013. doi: 10.1103/PhysRevLett.111.033601. URL http://link.aps.org/doi/10.1103/PhysRevLett.111.033601. 12

[37] M. P. Hedges, J. J. Longdell, Y. Li, and M. J. Sellars. Efficient quantum memory for light. *Nature*, 465(7301):1052–6, 2010. ISSN 1476-4687. doi: 10.1038/nature09081. URL http://www.ncbi.nlm.nih.gov/pubmed/20577210. 12

[38] K. Kutluer, M. F. Pascual-Winter, J. Dajczgewand, P. M. Ledingham, M. Mazzera, T. Chanelière, and H. de Riedmatten. Spectral-hole memory for light at the single-photon level. *Phys. Rev. A*,

93:040302, Apr 2016. doi: 10.1103/PhysRevA.93.040302. URL http://link.aps.org/doi/10.1103/PhysRevA.93.040302. 12, 88

[39] K. Akiba, K. Kashiwagi, M. Arikawa, and M. Kozuma. Storage and retrieval of nonclassical photon pairs and conditional single photons generated by the parametric down-conversion process. *New Journal of Physics*, 11(1):013049, 2009. URL http://stacks.iop.org/1367-2630/11/i=1/a=013049. 13, 14

[40] A. Haase, N. Piro, J. Eschner, and M. W. Mitchell. Tunable narrowband entangled photon pair source for resonant single-photon single-atom interaction. *Opt. Lett.*, 34(1):55–57, Jan 2009. doi: 10.1364/OL.34.000055. URL http://ol.osa.org/abstract.cfm?URI=ol-34-1-55.

[41] N. Piro, F. Rohde, C. Schuck, M. Almendros, J. Huwer, J. Ghosh, A. Haase, M. Hennrich, F. Dubin, and J. Eschner. Heralded single-photon absorption by a single atom. *Nat Phys*, 7(1):17–20, Jan 2011. ISSN 1745-2473. doi: 10.1038/nphys1805. URL http://dx.doi.org/10.1038/nphys1805.

[42] C. Clausen, F. BussiÃ¨res, A. Tiranov, H. Herrmann, C. Silberhorn, W. Sohler, M. Afzelius, and N. Gisin. A source of polarization-entangled photon pairs interfacing quantum memories with telecom photons. *New Journal of Physics*, 16(9):093058, 2014. URL http://stacks.iop.org/1367-2630/16/i=9/a=093058. 13, 14, 15, 94

[43] J. Jin, M. Grimau Puigibert, L. Giner, J. A. Slater, M. R. E. Lamont, V. B. Verma, M. D. Shaw, F. Marsili, S. W. Nam, D. Oblak, and W. Tittel. Entanglement swapping with quantum-memory-compatible photons. *Phys. Rev. A*, 92:012329, Jul 2015. doi: 10.1103/PhysRevA.92.012329. URL http://link.aps.org/doi/10.1103/PhysRevA.92.012329. 13, 14

[44] E. Saglamyurek, J. Jin, V. B. Verma, M. D. Shaw, F. Marsili, S. W. Nam, D. Oblak, and W. Tittel. Quantum storage of entangled telecom-wavelength photons in an erbium-doped optical fibre. *Nat Photon*, 9(2):83–87, Feb 2015. ISSN 1749-4885. URL http://dx.doi.org/10.1038/nphoton.2014.311. Letter. 13, 14, 15

[45] Z. Y. Ou and Y. J. Lu. Cavity enhanced spontaneous parametric down-conversion for the prolongation of correlation time between conjugate photons. *Phys. Rev. Lett.*, 83:2556–2559, Sep 1999. doi: 10.1103/PhysRevLett.83.2556. URL http://link.aps.org/doi/10.1103/PhysRevLett.83.2556. 13, 23, 54

[46] Y. Jeronimo-Moreno, S. Rodriguez-Benavides, and A. B. U'Ren. Theory of cavity-enhanced spontaneous parametric downconversion. *Laser Physics*, 20(5):1221–1233, 2010. ISSN 1555-6611. doi: 10.1134/S1054660X10090409. URL http://dx.doi.org/10.1134/S1054660X10090409. 13, 27, 29

[47] C.-S. Chuu and S. E. Harris. Ultrabright backward-wave biphoton source. *Phys. Rev. A*, 83:061803, Jun 2011. doi: 10.1103/PhysRevA.83.061803. URL http://link.aps.org/doi/10.1103/PhysRevA.83.061803. 13, 20

[48] E. Pomarico, B. Sanguinetti, N. Gisin, R. Thew, H. Zbinden, G. Schreiber, A. Thomas, and W. Sohler. Waveguide-based opo source of entangled photon pairs. *New Journal of Physics*, 11(11):113042, 2009. URL http://stacks.iop.org/1367-2630/11/i=11/a=113042. 13

[49] S. Krapick, H. Herrmann, V. Quiring, B. Brecht, H. Suche, and C. Silberhorn. An efficient integrated two-color source for heralded single photons. *New Journal of Physics*, 15(3):033010, 2013. URL http://stacks.iop.org/1367-2630/15/i=3/a=033010.

[50] K.-H. Luo, H. Herrmann, S. Krapick, B. Brecht, R. Ricken, V. Quiring, H. Suche, W. Sohler, and C. Silberhorn. Direct generation of genuine single-longitudinal-mode narrowband photon pairs. *New Journal of Physics*, 17(7):073039, 2015. URL http://stacks.iop.org/1367-2630/17/i=7/a=073039. 13, 14, 15, 27, 29

[51] B. Brecht, K.-H. Luo, H. Herrmann, and C. Silberhorn. A versatile design for resonant guided-wave parametric down-conversion sources for quantum repeaters. *Applied Physics B*, 122(5):1–11,

2016. ISSN 1432-0649. doi: 10.1007/s00340-016-6381-4. URL http://dx.doi.org/10.1007/s00340-016-6381-4. 13

[52] M. Förtsch, J. Fürst, C. Wittmann, D. Strekalov, A. Aiello, M. V. Chekhova, C. Silberhorn, G. Leuchs, and C. Marquardt. A versatile source of single photons for quantum information processing. *Nat. Comms.*, (2):1–8, 2013. ISSN 2041-1723. doi: 10.1038/ncomms2838. URL http://www.nature.com/ncomms/journal/v4/n5/abs/ncomms2838.html. 13, 46

[53] M. Förtsch, G. Schunk, J. U. Fürst, D. Strekalov, T. Gerrits, M. J. Stevens, F. Sedlmeir, H. G. L. Schwefel, S. W. Nam, G. Leuchs, and C. Marquardt. Highly efficient generation of single-mode photon pairs from a crystalline whispering-gallery-mode resonator source. *Phys. Rev. A*, 91:023812, Feb 2015. doi: 10.1103/PhysRevA.91.023812. URL http://link.aps.org/doi/10.1103/PhysRevA.91.023812. 13, 14, 118

[54] C. Reimer, L. Caspani, M. Clerici, M. Ferrera, M. Kues, M. Peccianti, A. Pasquazi, L. Razzari, B. E. Little, S. T. Chu, D. J. Moss, and R. Morandotti. Integrated frequency comb source of heralded single photons. *Opt. Express*, 22(6):6535–6546, Mar 2014. doi: 10.1364/OE.22.006535. URL http://www.opticsexpress.org/abstract.cfm?URI=oe-22-6-6535. 13

[55] H. Wang, T. Horikiri, and T. Kobayashi. Polarization-entangled mode-locked photons from cavity-enhanced spontaneous parametric down-conversion. *Phys. Rev. A*, 70:043804, Oct 2004. doi: 10.1103/PhysRevA.70.043804. URL http://link.aps.org/doi/10.1103/PhysRevA.70.043804. 13, 14, 15, 47, 94

[56] J. S. Neergaard-Nielsen, B. M. Nielsen, H. Takahashi, A. I. Vistnes, and E. S. Polzik. High purity bright single photon source. *Optics Express*, 15 (13):7940–7949, 2007. ISSN 1094-4087. doi: 10.1364/OE.15.007940. URL http://www.opticsinfobase.org/abstract.cfm?id=138385.

[57] F. Wolfgramm, Y. A. De Icaza Astiz, F. A. Beduini, A. Cerè, and M. W. Mitchell. Atom-resonant heralded single photons by

interaction-free measurement. *Physical Review Letters*, 106(5), 2011. ISSN 00319007. doi: 10.1103/PhysRevLett.106.053602. URL http://journals.aps.org/prl/abstract/10.1103/PhysRevLett.106.053602. 13, 14, 44, 65

[58] J. Fekete, D. Rieländer, M. Cristiani, and H. de Riedmatten. Ultranarrow-band photon-pair source compatible with solid state quantum memories and telecommunication networks. *Phys. Rev. Lett.*, 110:220502, May 2013. doi: 10.1103/PhysRevLett.110.220502. URL http://link.aps.org/doi/10.1103/PhysRevLett.110.220502. 13, 14, 15, 27, 31, 49, 59, 60, 62, 68, 80, 82

[59] C.-S. Chuu, G. Y. Yin, and S. E. Harris. A miniature ultrabright source of temporally long, narrowband biphotons. *Applied Physics Letters*, 101(5):051108, 2012. doi: http://dx.doi.org/10.1063/1.4740270. URL http://scitation.aip.org/content/aip/journal/apl/101/5/10.1063/1.4740270. 13, 20

[60] X.-H. Bao, Y. Qian, J. Yang, H. Zhang, Z.-B. Chen, T. Yang, and J.-W. Pan. Generation of narrow-band polarization-entangled photon pairs for atomic quantum memories. *Phys. Rev. Lett.*, 101: 190501, Nov 2008. doi: 10.1103/PhysRevLett.101.190501. URL http://link.aps.org/doi/10.1103/PhysRevLett.101.190501. 13, 14, 94

[61] C. E. Kuklewicz, F. N. C. Wong, and J. H. Shapiro. Time-bin-modulated biphotons from cavity-enhanced down-conversion. *Phys. Rev. Lett.*, 97:223601, Nov 2006. doi: 10.1103/PhysRevLett.97.223601. URL http://link.aps.org/doi/10.1103/PhysRevLett.97.223601. 13

[62] M. Scholz, L. Koch, and O. Benson. Statistics of narrow-band single photons for quantum memories generated by ultrabright cavity-enhanced parametric down-conversion. *Phys. Rev. Lett.*, 102(6), 2009. ISSN 00319007. doi: 10.1103/PhysRevLett.102.063603. URL

http://journals.aps.org/prl/abstract/10.1103/PhysRevLett.102.063603.

[63] M. Scholz, L. Koch, R. Ullmann, and O. Benson. Single-mode operation of a high-brightness narrow-band single-photon source. *Applied Physics Letters*, 94(20):201105, 2009. doi: http://dx.doi.org/10.1063/1.3139768. URL http://scitation.aip.org/content/aip/journal/apl/94/20/10.1063/1.3139768. 13, 14

[64] D. Höckel, L. Koch, and O. Benson. Direct measurement of heralded single-photon statistics from a parametric down-conversion source. *Phys. Rev. A*, 83:013802, Jan 2011. doi: 10.1103/PhysRevA.83.013802. URL http://link.aps.org/doi/10.1103/PhysRevA.83.013802. 13

[65] H. Zhang, X.-M. Jin, J. Yang, H.-N. Dai, S.-J. Yang, T.-M. Zhao, J. Rui, Y. He, X. Jiang, F. Yang, G.-S. Pan, Z.-S. Yuan, Y. Deng, Z.-B. Chen, X.-H. Bao, S. Chen, B. Zhao, and J.-W. Pan. Preparation and storage of frequency-uncorrelated entangled photons from cavity-enhanced spontaneous parametric downconversion. 5(10):628–632. ISSN 1749-4885. doi: 10.1038/nphoton.2011.213. URL http://dx.doi.org/10.1038/nphoton.2011.213. 13, 14

[66] F. Monteiro, A. Martin, B. Sanguinetti, H. Zbinden, and R. T. Thew. Narrowband photon pair source for quantum networks. *Opt. Express*, 22(4):4371–4378, Feb 2014. doi: 10.1364/OE.22.004371. URL http://www.opticsexpress.org/abstract.cfm?URI=oe-22-4-4371.

[67] A. Ahlrichs and O. Benson. Bright source of indistinguishable photons based on cavity-enhanced parametric down-conversion utilizing the cluster effect. *Appl. Phys. Lett.*, 108(2): 021111, 2016. doi: http://dx.doi.org/10.1063/1.4939925. URL http://scitation.aip.org/content/aip/journal/apl/108/2/10.1063/1.4939925. 13

[68] Z. Zhou, D. Ding, Y. Li, F. Wang, B. Shi, and G. Guo. Cavity-enhanced narrow bandwidth photon pairs at telecom wavelength generation with a

triple resonances configuration. *Journal of the Optical Society of America B*, 31(1):128–134, 2014. ISSN 21622701. 14

[69] E. Saglamyurek, M. Grimau Puigibert, Q. Zhou, L. Giner, F. Marsili, V. B. Verma, S. Woo Nam, L. Oesterling, D. Nippa, D. Oblak, and W. Tittel. A multiplexed light-matter interface for fibre-based quantum networks. *Nat. Comms.*, 7, Apr 2016. URL http://dx.doi.org/10.1038/ncomms11202. 13, 113

[70] G. Schunk, U. Vogl, D. V. Strekalov, M. Förtsch, F. Sedlmeir, H. G. L. Schwefel, M. Göbelt, S. Christiansen, G. Leuchs, and C. Marquardt. Interfacing transitions of different alkali atoms and telecom bands using one narrowband photon pair source. *Optica*, 2(9):773–778, Sep 2015. doi: 10.1364/OPTICA.2.000773. URL http://www.osapublishing.org/optica/abstract.cfm?URI=optica-2-9-773.

[71] J. Wang, P.-Y. Lv, J.-M. Cui, B.-H. Liu, J.-S. Tang, Y.-F. Huang, C.-F. Li, and G.-C. Guo. Generation of nondegenerate narrow-band photon pairs for a hybrid quantum network. *Phys. Rev. Applied*, 4:064011, Dec 2015. doi: 10.1103/PhysRevApplied.4.064011. URL http://link.aps.org/doi/10.1103/PhysRevApplied.4.064011.

[72] A. Lenhard, M. Bock, C. Becher, S. Kucera, J. Brito, P. Eich, P. Müller, and J. Eschner. Telecom-heralded single-photon absorption by a single atom. *Phys. Rev. A*, 92:063827, Dec 2015. doi: 10.1103/PhysRevA.92.063827. URL http://link.aps.org/doi/10.1103/PhysRevA.92.063827.

[73] D. Rieländer, K. Kutluer, P. M. Ledingham, M. Gündoğan, J. Fekete, M. Mazzera, and H. de Riedmatten. Quantum storage of heralded single photons in a praseodymium-doped crystal. *Phys. Rev. Lett.*, 112:040504, Jan 2014. doi: 10.1103/PhysRevLett.112.040504. URL http://link.aps.org/doi/10.1103/PhysRevLett.112.040504. 13, 15, 22, 57, 80, 85, 110, 113

[74] L. Olislager, J. Cussey, A. T. Nguyen, P. Emplit, S. Massar, J.-M. Merolla, and K. P. Huy. Frequency-bin entangled photons. *Phys. Rev. A*, 82:013804, Jul 2010. doi: 10.1103/PhysRevA.82.013804. URL http://link.aps.org/doi/10.1103/PhysRevA.82.013804. 16, 96, 98, 99, 116

[75] P. Grangier, G. Roger, and A. Aspect. Experimental evidence for a photon anticorrelation effect on a beam splitter: A new light on single-photon interferences. *EPL (Europhysics Letters)*, 1(4):173, 1986. URL http://stacks.iop.org/0295-5075/1/i=4/a=004. 17

[76] Z.-Y. J. Ou. *Multi-Photon Quantum Interference*. Springer Science and Business Media, 2007. ISBN 978-0-387-25532-3. 18

[77] H. Karlsson. *Fabrication of periodically poled crystals from the KTP family and their applications in nonlinear o [Elektronisk resurs]...* Fysiska institutionen, 1999. ISBN 99-3028750-7. URL http://www.diva-portal.org/smash/get/diva2:8587/FULLTEXT01.pdf. 19

[78] D. H. Jundt. Temperature-dependent sellmeier equation for the index of refraction, ne, in congruent lithium niobate. *Opt. Lett.*, 22(20):1553–1555, Oct 1997. doi: 10.1364/OL.22.001553. URL http://ol.osa.org/abstract.cfm?URI=ol-22-20-1553. 20, 38

[79] G. D. Boyd and D. A. Kleinman. Parametric interaction of focused Gaussion light beams. *Journal of Applied Physics*, 39(8): 3597–3639, 1968. ISSN 00218979. doi: 10.1063/1.1656831. URL http://scitation.aip.org/content/aip/journal/jap/39/8/10.1063/1.1656831. 20

[80] A. Predojević and M. W. Mitchell. *Engineering the Atom-Photon Interaction*. Springer Science and Business Media, 2015. ISBN 978-3-319-19231-4. 20

[81] A. Christ, K. Laiho, A. Eckstein, K. N. Cassemiro, and C. Silberhorn. Probing multimode squeezing with correlation functions. *New Journal of Physics*, 13(3):033027, 2011. URL http://stacks.iop.org/1367-2630/13/i=3/a=033027. 22, 85

[82] C. W. Chou, S. V. Polyakov, A. Kuzmich, and H. J. Kimble. Single-photon generation from stored excitation in an atomic ensemble. *Phys. Rev. Lett.*, 92:213601, May 2004. doi: 10.1103/PhysRevLett.92.213601. URL http://link.aps.org/doi/10.1103/PhysRevLett.92.213601. 22, 86

[83] B. E. A. Saleh and M. C. Teich. *Fundamentals of Photonics*. Wiley, 2007. ISBN 987-0-471-35832-9. 24, 26

[84] F. Wolfgramm. *Atomic Quantum Metrology with Narrowband Entangled and Squeezed States of Light*. ICFO - The Institute of Photonic Sciences, 2011. 25, 74

[85] H. Kogelnik and T. Li. Laser beams and resonators. *Appl. Opt.*, 5(10):1550–1567, Oct 1966. doi: 10.1364/AO.5.001550. URL http://ao.osa.org/abstract.cfm?URI=ao-5-10-1550. 26

[86] R. C. Eckardt, C. D. Nabors, W. J. Kozlovsky, and R. L. Byer. Optical parametric oscillator frequency tuning and control. *J. Opt. Soc. Am. B*, 8(3):646–667, Mar 1991. doi: 10.1364/JOSAB.8.000646. URL http://josab.osa.org/abstract.cfm?URI=josab-8-3-646. 27, 29

[87] CASIX. Properties of lithium niobate crystal series, June 2016. URL http://www.fabrinet.co.th/custappl/casix/aa/product/prod_cry_linbo3.html. 38

[88] X. Wu, C. Zhou, W. R. Huang, F. Ahr, and F. X. Kärtner. Temperature dependent refractive index and absorption coefficient of congruent lithium niobate crystals in the terahertz range. *Opt. Express*, 23(23):29729–29737, Nov 2015. doi: 10.1364/OE.23.029729. URL http://www.opticsexpress.org/abstract.cfm?URI=oe-23-23-29729. 38

[89] P. Brand, B. Boulanger, P. Segonds, Y. Petit, C. Félix, B. Ménaert, T. Taira, and H. Ishizuki. Angular quasi-phase-matching experiments and determination of accurate sellmeier equations for 5%mgo:ppln. *Opt. Lett.*, 34(17):2578–2580, Sep 2009. doi: 10.1364/OL.34.002578. URL http://ol.osa.org/abstract.cfm?URI=ol-34-17-2578.

[90] O. Gayer, Z. Sacks, E. Galun, and A. Arie. Temperature and wavelength dependent refractive index equations for mgo-doped congruent and stoichiometric $linbo_3$. *Appl. Phys. B*, 91:343–348, 2008. URL http://link.springer.com/article/10.1007/s00340-008-2998-2.

[91] G. J. Edwards and M. Lawrence. A temperature-dependent dispersion equation for congruently grown lithium niobate. *Optical and Quantum Electronics*, 16:373–375, 1984. URL http://link.springer.com/article/10.1007/BF00620081. 38

[92] M. Gündoğan, P. M. Ledingham, A. Almasi, M. Cristiani, and H. de Riedmatten. Quantum storage of a photonic polarization qubit in a solid. *Phys. Rev. Lett.*, 108:190504, May 2012. doi: 10.1103/PhysRevLett.108.190504. URL http://link.aps.org/doi/10.1103/PhysRevLett.108.190504. 40

[93] M. Rambach, A. Nikolova, T. J. Weinhold, and A. G. White. Sub-megahertz single photon source. *arXiv*, (1601.06173), Jan 2016. doi: arXiv:1601.06173. URL http://arxiv.org/abs/1601.06173. 44

[94] P. Sekatski, N. Sangouard, F. BussiÃ¨res, C. Clausen, N. Gisin, and H. Zbinden. Detector imperfections in photon-pair source characterization. *Journal of Physics B: Atomic, Molecular and Optical Physics*, 45(12):124016, 2012. URL http://stacks.iop.org/0953-4075/45/i=12/a=124016. 46, 83

[95] M. Afzelius, I. Usmani, A. Amari, B. Lauritzen, A. Walther, C. Simon, N. Sangouard, J. c. v. Minář, H. de Riedmatten, N. Gisin, and S. Kröll. Demonstration of atomic frequency comb memory for light with spin-wave storage. *Phys. Rev. Lett.*, 104:

040503, Jan 2010. doi: 10.1103/PhysRevLett.104.040503. URL http://link.aps.org/doi/10.1103/PhysRevLett.104.040503. 57

[96] M. Gündoğan, M. Mazzera, P. M. Ledingham, M. Cristiani, and H. de Riedmatten. Coherent storage of temporally multimode light using a spin-wave atomic frequency comb memory. *New Journal of Physics*, 15(4):045012, 2013. 58, 59, 61, 65

[97] Y. C. Sun. *Rare Earth Materiais in Optical Storage and Data Processing Applications*, volume 83. Springer Science and Business Media, 2005. ISBN 978-3-540-23886-7. doi: 10.1007/3-540-28209-2_7. 61

[98] M. Nilsson, L. Rippe, S. Kröll, R. Klieber, and D. Suter. Hole-burning techniques for isolation and study of individual hyperfine transitions in inhomogeneously broadened solids demonstrated in pr^{3+}: Y_2sio_5. *Phys. Rev. B*, 70:214116, Dec 2004. doi: 10.1103/PhysRevB.70.214116. URL http://link.aps.org/doi/10.1103/PhysRevB.70.214116. 61

[99] D. L. McAuslan, L. R. Taylor, and J. J. Longdell. Using quantum memory techniques for optical detection of ultrasound. *Applied Physics Letters*, 101(19):191112, 2012. doi: http://dx.doi.org/10.1063/1.4766341. URL http://scitation.aip.org/content/aip/journal/apl/101/19/10.1063/1.4766341. 65

[100] J. R. Schwesyg, M. C. C. Kajiyama, M. Falk, D. H. Jundt, K. Buse, and M. M. Fejer. Light absorption in undoped congruent and magnesium-doped lithium niobate crystals in the visible wavelength range. *Appl. Phys. B*, 100(109), May 2010. URL http://link.springer.com/article/10.1007/s00340-010-4063-1. 75

[101] S. Fasel, O. Alibart, S. Tanzilli, P. Baldi, A. Beveratos, N. Gisin, and H. Zbinden. High-quality asynchronous heralded single-photon source at telecom wavelength. *New Journal of Physics*, 6(1):163–, 2004. ISSN 1367-2630. URL http://stacks.iop.org/1367-2630/6/i=1/a=163. 82, 83

[102] K. J. McNeil and C. W. Gardiner. Quantum statistics of parametric oscillation. *Phys. Rev. A*, 28(3):1560–1566, Sept. 1983. URL http://link.aps.org/doi/10.1103/PhysRevA.28.1560. 85

[103] M. Afzelius, C. Simon, H. de Riedmatten, and N. Gisin. Multimode quantum memory based on atomic frequency combs. *Phys. Rev. A*, 79:052329, May 2009. doi: 10.1103/PhysRevA.79.052329. URL http://link.aps.org/doi/10.1103/PhysRevA.79.052329. 89

[104] M. Gündoğan, P. M. Ledingham, K. Kutluer, M. Mazzera, and H. de Riedmatten. Solid state spin-wave quantum memory for time-bin qubits. *Phys. Rev. Lett.*, 114(23):230501–, June 2015. URL http://link.aps.org/doi/10.1103/PhysRevLett.114.230501. 88, 89

[105] P. Jobez, C. Laplane, N. Timoney, N. Gisin, A. Ferrier, P. Goldner, and M. Afzelius. Coherent spin control at the quantum level in an ensemble-based optical memory. *Phys. Rev. Lett.*, 114(23):230502–, June 2015. URL http://link.aps.org/doi/10.1103/PhysRevLett.114.230502. 88

[106] L. Jiang, J. M. Taylor, and M. D. Lukin. Fast and robust approach to long-distance quantum communication with atomic ensembles. *Phys. Rev. A*, 76(1):012301–10, July 2007. URL http://link.aps.org/abstract/PRA/v76/e012301. 93

[107] P. G. Kwiat, K. Mattle, H. Weinfurter, A. Zeilinger, A. V. Sergienko, and Y. Shih. New high-intensity source of polarization-entangled photon pairs. *Phys. Rev. Lett.*, 75:4337–4341, Dec 1995. doi: 10.1103/PhysRevLett.75.4337. URL http://link.aps.org/doi/10.1103/PhysRevLett.75.4337. 94

[108] M. Giustina, M. A. M. Versteegh, S. Wengerowsky, J. Handsteiner, A. Hochrainer, K. Phelan, F. Steinlechner, J. Kofler, J.-A. Larsson, C. Abellán, W. Amaya, V. Pruneri, M. W. Mitchell, J. Beyer, T. Gerrits, A. E. Lita, L. K. Shalm, S. W. Nam, T. Scheidl, R. Ursin, B. Wittmann, and A. Zeilinger. Significant-loophole-free test of bell's theorem with entangled photons. *Phys. Rev. Lett.*,

115:250401, Dec 2015. doi: 10.1103/PhysRevLett.115.250401. URL http://link.aps.org/doi/10.1103/PhysRevLett.115.250401. 94

[109] F. Steinlechner, P. Trojek, M. Jofre, H. Weier, D. Perez, T. Jennewein, R. Ursin, J. Rarity, M. W. Mitchell, J. P. Torres, H. Weinfurter, and V. Pruneri. A high-brightness source of polarization-entangled photons optimized for applications in free space. *Opt. Express*, 20(9):9640–9649, Apr 2012. doi: 10.1364/OE.20.009640. URL http://www.opticsexpress.org/abstract.cfm?URI=oe-20-9-9640. 94

[110] B. Hensen, H. Bernien, A. E. Dréau, A. Reiserer, N. Kalb, M. S. Blok, J. Ruitenberg, R. F. L. Vermeulen, R. N. Schouten, C. Abellán, W. Amaya, V. Pruneri, M. W. Mitchell, M. Markham, D. J. Twitchen, D. Elkouss, S. Wehner, T. H. Taminiau, and R. Hanson. Loophole-free Bell inequality violation using electron spins separated by 1.3 kilometres. *Nature*, 526 (7575):682–686, 2015. ISSN 0028-0836. doi: 10.1038/nature15759. URL http://www.nature.com/doifinder/10.1038/nature15759. 95

[111] J. D. Franson. Bell inequality for position and time. *Phys. Rev. Lett.*, 62:2205–2208, May 1989. doi: 10.1103/PhysRevLett.62.2205. URL http://link.aps.org/doi/10.1103/PhysRevLett.62.2205. 95

[112] R. T. Thew, A. Acín, H. Zbinden, and N. Gisin. Bell-type test of energy-time entangled qutrits. *Phys. Rev. Lett.*, 93: 010503, Jul 2004. doi: 10.1103/PhysRevLett.93.010503. URL http://link.aps.org/doi/10.1103/PhysRevLett.93.010503. 96

[113] L. Olislager, I. Mbodji, E. Woodhead, J. Cussey, L. Furfaro, P. Emplit, S. Massar, K. P. Huy, and J.-M. Merolla. Implementing two-photon interference in the frequency domain with electro-optic phase modulators. *New Journal of Physics*, 14(4):043015, 2012. URL http://stacks.iop.org/1367-2630/14/i=4/a=043015. 96, 104, 105

[114] J. F. Clauser and M. A. Horne. Experimental consequences of objective local theories. *Phys. Rev. D*, 10:526–535, Jul 1974. doi: 10.1103/PhysRevD.10.526. URL http://link.aps.org/doi/10.1103/PhysRevD.10.526. 105

[115] S. Yang, Y. Wang, D. D. Bhaktavatsala Rao, T. Hien Tran, A. S. Momenzadeh, M. Markham, D. J. Twitchen, P. Wang, W. Yang, R. Stöhr, P. Neumann, H. Kosaka, and J. Wrachtrup. High-fidelity transfer and storage of photon states in a single nuclear spin. *Nat Photon*, 10(8):507–511, Aug 2016. ISSN 1749-4885. URL http://dx.doi.org/10.1038/nphoton.2016.103. Letter. 118

[116] J.-M. Mérolla, Y. Mazurenko, J.-P. Goedgebuer, and W. T. Rhodes. Single-photon interference in sidebands of phase-modulated light for quantum cryptography. *Phys. Rev. Lett.*, 82: 1656–1659, Feb 1999. doi: 10.1103/PhysRevLett.82.1656. URL http://link.aps.org/doi/10.1103/PhysRevLett.82.1656. 119

[117] P. Komar, E. M. Kessler, M. Bishof, L. Jiang, A. S. Sorensen, J. Ye, and M. D. Lukin. A quantum network of clocks. *Nat Phys*, 10(8):582–587, Aug 2014. ISSN 1745-2473. URL http://dx.doi.org/10.1038/nphys3000. Article. 119

[118] D. Gottesman, T. Jennewein, and S. Croke. Longer-baseline telescopes using quantum repeaters. *Phys. Rev. Lett.*, 109: 070503, Aug 2012. doi: 10.1103/PhysRevLett.109.070503. URL http://link.aps.org/doi/10.1103/PhysRevLett.109.070503. 119

Acknowledgements

I would like to thank my PhD advisor Hugues de Riedmatten for giving me the opportunity to work on a technically challenging experiment and to give me a deep insight into the topic of quantum communication. Thanks for having the possibility to work in an exclusive and stimulating environment like ICFO with an international and enjoyable team. Thanks for the patience and the support.

I thank Julia Fekete, Mustafa Gündogan, Patrick Ledingham and Matteo Cristiani for a very warm welcoming in the group, the kind introduction into the lab, their advises, help and the good atmosphere.

Thanks to Margherita Mazzera, Kutlu Kutluer and Alessandro Seri for joining the group and helping with the experiments in particular taking over the sophisticated work on the quantum memory.

I thank Andreas Lenhard for his patience and help during the last and hardest phase of my PhD.

Without the electronic and the mechanical workshops at ICFO these experiments would not have been possible, their quick interaction prevented long waiting times.

I thank my family and friends for their emotional support, their visits and their company.